





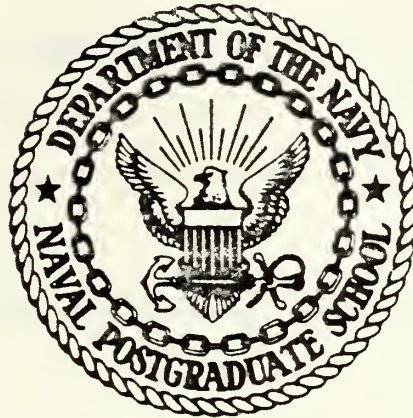






# NAVAL POSTGRADUATE SCHOOL

## Monterey, California



# THESIS

SPATIAL STRUCTURES OF OPTICAL PARAMETERS IN THE  
CALIFORNIA CURRENT AS MEASURED WITH THE  
NIMBUS-7 COASTAL ZONE COLOR SCANNER

by

John T. McMurtrie, Jr.

March 1984

Thesis Advisor:

J. L. Mueller

Approved for public release; distribution unlimited.



## REPORT DOCUMENTATION PAGE

READ INSTRUCTIONS  
BEFORE COMPLETING FORM

1. REPORT NUMBER		2. GOVT ACCESSION NO.	3. RECIPIENT'S CATALOG NUMBER
4. TITLE (and Subtitle) Spatial Structures of Optical Parameters in the California Current, As Measured with the Nimbus-7 Coastal Zone Color Scanner			5. TYPE OF REPORT & PERIOD COVERED Master's Thesis March 1984
7. AUTHOR(s) John T. McMurtrie, Jr.			6. PERFORMING ORG. REPORT NUMBER
9. PERFORMING ORGANIZATION NAME AND ADDRESS Naval Postgraduate School Monterey, California 93943			8. CONTRACT OR GRANT NUMBER(s)
11. CONTROLLING OFFICE NAME AND ADDRESS Naval Postgraduate School Monterey, California 93943			10. PROGRAM ELEMENT, PROJECT, TASK AREA & WORK UNIT NUMBERS N0001484 WR24001
14. MONITORING AGENCY NAME & ADDRESS (if different from Controlling Office)			12. REPORT DATE March 1984
			13. NUMBER OF PAGES 150
			15. SECURITY CLASS. (of this report) Unclassified
			15a. DECLASSIFICATION/ DOWNGRADING SCHEDULE
16. DISTRIBUTION STATEMENT (of this Report)  Approved for public release; distribution unlimited.			
17. DISTRIBUTION STATEMENT (of the abstract entered in Block 20, if different from Report)			
18. SUPPLEMENTARY NOTES  The research reported here was supported by The Office of Naval Research (Code 425 OA) Work request N0001484 WR24001.			
19. KEY WORDS (Continue on reverse side if necessary and identify by block number) Ocean Optical Depth Variability, Remote Sensing, Ocean Color, Coastal Zone Color Scanner(CZCS), California Current System, Empirical Orthogonal Functions.			
20. ABSTRACT (Continue on reverse side if necessary and identify by block number) Optical variability across the continental slope and shelf off Central California was studied using Nimbus-7 Coastal Zone Color Scanner (CZCS) data. CZCS estimates of $k(490)$ , the irradiance attenuation coefficient at 490 nm, were expressed as optical depth $1/k(490)$ . A modified atmospheric correction algorithm was used to account for water radiance at 670 nm. Time sequences of $1/k(490)$ were assembled and partitioned into four zonal transects, at different latitudes, spanning May through November in 1979, 1980 and 1982.			





## #20 - ABSTRACT - (CONTINUED)

Empirical Orthogonal Functions(EOFs) were calculated for each partition. The first EOFs are dominated by scales of order 180 km, with in all cases, a band of low optical depth water in the first 100 km adjacent to the coast. Scales decrease in successive EOFs, to about 40 km in the fifth EOF. The feasibility of joining EOFs from different partitions was demonstrated as a precursor for future applications to piecewise analysis of oceanic satellite data.



Approved for public release; distribution unlimited

Spatial Structures of Optical Parameters in the California  
Current,  
As Measured with the Nimbus-7 Coastal Zone Color Scanner

by

John T. McMurtrie, Jr.  
Lieutenant, United States Navy  
B.S., University of South Carolina, 1977

Submitted in partial fulfillment of the  
requirements for the degree of

MASTER OF SCIENCE IN METEOROLOGY AND OCEANOGRAPHY

from the

NAVAL POSTGRADUATE SCHOOL  
March 1984





## ABSTRACT

Optical variability across the continental slope and shelf off Central California was studied using Nimbus-7 Coastal Zone Color Scanner (CZCS) data. CZCS estimates of  $k(490)$ , the irradiance attenuation coefficient at 490 nm, were expressed as optical depth  $1/k(490)$ . A modified atmospheric correction algorithm was used to account for water radiance at 670 nm. Time sequences of  $1/k(490)$  were assembled and partitioned into four zonal transects, at different latitudes, spanning May through November in 1979, 1980 and 1982. Empirical Orthogonal Functions (EOFs) were calculated for each partition. The first EOFs are dominated by scales of order 180 km, with in all cases, a band of low optical depth water in the first 100 km adjacent to the coast. Scales decrease in successive EOFs, to about 40 km in the fifth EOF. The feasibility of joining EOFs from different partitions was demonstrated as a precursor for future applications to piecewise analysis of oceanic satellite data.



## TABLE OF CONTENTS

I.	INTRODUCTION . . . . .	14
II.	OCEANOGRAPHY OF THE CENTRAL CALIFORNIA COAST . . .	17
A.	THE STUDY DOMAIN . . . . .	17
1.	Coverage . . . . .	17
a.	Area Domain . . . . .	17
b.	Time Domain . . . . .	19
2.	Geometry . . . . .	19
a.	Coastal . . . . .	19
b.	Bathymetry . . . . .	20
3.	Descriptive Oceanography . . . . .	20
a.	Coastal Upwelling . . . . .	20
b.	Currents . . . . .	24
c.	Water Masses . . . . .	30
III.	CZCS OCEAN COLOR IMAGES AND UPPER OCEAN OPTICAL PROPERTIES . . . . .	34
A.	INTRODUCTION . . . . .	34
B.	SYSTEM DESCRIPTION . . . . .	35
1.	The Nimbus-7 Coastal Zone Color Scanner (CZCS) . . . . .	35
2.	Measured Signal . . . . .	37
C.	CZCS GEOPHYSICAL ALGORITHMS . . . . .	38
1.	Atmospheric Corrections . . . . .	38





2.	Clear Water Radiance . . . . .	41
3.	Bio-optic Parameters . . . . .	43
a.	Chlorophyl Concentrations . . . . .	43
b.	Diffuse Attenuation Coefficient . . . . .	45
D.	SIGNAL FACTORS . . . . .	46
IV.	EMPIRICAL ORTHOGONAL FUNCTION ANALYSIS METHODS . .	48
A.	INTRODUCTION . . . . .	48
B.	EOF EQUATIONS . . . . .	52
1.	Raw Data Conversion . . . . .	52
2.	Principal Direction of Scatter . . . . .	53
3.	Principal Component, Eigenvalue and Eigenvector Representaton . . . . .	55
C.	PARTITIONED EOF ANALYSIS . . . . .	57
1.	Purpose . . . . .	57
2.	Rules and Methods . . . . .	58
3.	Equation Development . . . . .	61
D.	INTERPRETATION . . . . .	64
V.	RESULTS . . . . .	65
A.	INTRODUCTION . . . . .	65
B.	CORRECTIONS FOR NON-ZERO $L_w(670)$ IN COASTAL WATERS . . . . .	65
C.	DATA STRUCTURE . . . . .	70
1.	Partition 1 (Zonal Transect at 35 53N) . .	71



2. Partition 2 (Zonal Transect at 35 40N)	. . . 73
3. Partition 3 (Zonal Transect at 35 22N)	. . . 75
4. Partition 4 (Zonal Transect at 35 00N)	. . . 76
D. EOF ANALYSIS . . . . .	79
1. Eigenvalues and Degrees of Freedom . . . . .	79
2. Data Reconstruction Using Eigenvectors and Principal Components . . . . .	81
3. Mean Structure . . . . .	88
4. Structural Content of Eigenvectors and Principal Components . . . . .	90
5. The Joining Of Two Partitions . . . . .	112
VI. DISCUSSION AND CONCLUSIONS . . . . .	116
APPENDIX A. SATELLITE DATA PROCESSING METHODS . . . . .	122
A. INTRODUCTION . . . . .	122
B. LEVEL-I PROCESSING . . . . .	123
C. LEVEL-II PROCESSING . . . . .	128
D. LEVEL-III PROCESSING . . . . .	130
APPENDIX B. DATA CONDITICNING . . . . .	132
APPENDIX C. EOF PROCESSING . . . . .	140
LIST OF REFERENCES . . . . .	144
INITIAL DISTRIBUTION LIST . . . . .	149





# LIST OF FIGURES

Figure 1.	Ocean Bathymetry Off the California Coast . .	18
Figure 2.	Ocean Bathymetry Off the California Coast . .	21
Figure 3.	Graph Showing T-S Curves Defining Subarctic Water . . . . .	33
Figure 4.	Plot Showing the Difference Between Minimization of Distances . . . . .	49
Figure 5.	Trackline plots. . . . .	60
Figure 6.	Comparison Plots For 1/K(490) Between Track 4 and Selected . . . . .	69
Figure 7.	The Optical Depth Parameter, 1/K(490), Across Partition 1 (35 53N) . . . . .	72
Figure 8.	The Optical Depth Parameter, 1/K(490), Across Partition 2 (35 40N) . . . . .	74
Figure 9.	The Optical Depth Parameter, 1/K(490), Across Partition 3 (35 22N) . . . . .	77
Figure 10.	The Optical Depth Parameter, 1/K(490), Across Partition 4 (35 00N) . . . . .	80
Figure 11.	Eigenvalues for Partition One . . . . .	83
Figure 12.	Eigenvalues for Partition Two . . . . .	84
Figure 13.	Eigenvalues for Partition Three . . . . .	85
Figure 14.	Eigenvalues for Partition Four . . . . .	86
Figure 15.	Reconstruction of Optical Depth Transect of 3 June 1980 . . . . .	89
Figure 16.	Mean and Eigenvectors 1 to 5 for Partition One. . . . .	93
Figure 17.	Mean and Eigenvectors 1 to 5 for Partition Two. . . . .	94
Figure 18.	Mean and Eigenvectors 1 to 5 for Partition Three. . . . .	95



Figure 19.	Mean and Eigenvectors 1 to 5 for Partition Four. . . . .	96
Figure 20.	Principal Components 1 to 5 for Partition One. . . . .	97
Figure 21.	Principal Components 1 to 5 for Partition Two. . . . .	98
Figure 22.	Principal Components 1 to 5 for Partition Three. . . . .	99
Figure 23.	Principal Components 1 to 5 for Partition Four. . . . .	100
Figure 24.	Mean and Eigenvectors 6 to 10 for Partition One. . . . .	104
Figure 25.	Mean and Eigenvectors 6 to 10 for Partition Two. . . . .	105
Figure 26.	Mean and Eigenvectors 6 to 10 for Partition Three. . . . .	106
Figure 27.	Mean and Eigenvectors 6 to 10 for Partition Four. . . . .	107
Figure 28.	Principal Components 6 to 10 for Partition One. . . . .	108
Figure 29.	Principal Components 6 to 10 for Partition Two. . . . .	109
Figure 30.	Principal Components 6 to 10 for Partition Three. . . . .	110
Figure 31.	Principal Components 6 to 10 for Partition Four. . . . .	111
Figure 32.	Level-I Processing Schematic Diagram . . .	124
Figure 33.	Level-II Processing Schematic Diagram . . .	129
Figure 34.	Level-III Processing Schematic Diagram . .	131
Figure 35.	Data Conditioning Schematic Diagram . . . .	133
Figure 36.	Partitioning Scheme for Track One (35 53 N) . . . . .	136



Figure 37.	Partitioning Scheme for Track Two (35 40 N) . . . . .	137
Figure 38.	Partitioning Scheme for Track Three (35 22 N) . . . . .	138
Figure 39.	Partitioning Scheme for Track Four (35 53 N) . . . . .	139





# LIST OF TABLES

TABLE I.	Characteristics of the CZCS . . . . .	36
TABLE II.	Eigenvalue Data for Partitions 1 through 4 . . . . .	82
TABLE III.	Eigenvalue Data for Joining Process . . .	115
TABLE IV.	Satellite Data Tapes . . . . .	125
TABLE V.	Partition dimensions . . . . .	134



## ACKNOWLEDGEMENT

The tremendous effort of Ms. Melissa Ciandro, EDM Services Company, in processing the unending chain of program changes and updates deserves special recognition. Also, her presence served as an organizational factor to keep me on track for the completion of this thesis.

This thesis presented many problems that were resolved by the expertise of the thesis advisor, Dr. James Mueller, Adjunct Professor of Oceanography. These problems have left me with a keen awareness of the scope and breadth involved in the processing of satellite data. Support in the mathematical development came from my second reader, Dr. A. J. Willmott. Finally, a special thanks to my wife who accepted my long hours away from home with no complaints.



## I. INTRODUCTION

Satellite remote sensing systems offer fast, economical means of determining the horizontal structure of the oceans on a global basis. The objective of this thesis is to contribute to the development of empirical methods for using satellite images of optical parameters and sea surface temperature (SST) to infer the upper ocean's vertical structure, through interpolation and extrapolation of relatively limited in situ data.

The objective is being approached through regional case studies of correlations between optical parameters and physical water mass properties in the upper ocean in different regions of the world. More specifically, this thesis is a preliminary case study of the California Current region. The ultimate goal is to relate statistically the horizontal structure of optical properties observed with the Coastal Zone Color Scanner (CZCS) to the underlying vertical structures of temperature and salinity, as well as bio-optical parameters, for a given region and season.

The study domain encompasses the continental slope and shelf off the coast of California between Point Sur and Point Arguello. This area was selected to investigate an



ocean upwelling front which is known to persist throughout the upwelling season (Traganza, et al., 1979). The northern and southern portions of the study domain are typified by complex eddy structure associated with irregular features in the bathymetry, such as off Point Sur. Between Point Sur and Point Arguello, on the other hand, isolines of SST and optical parameters tend to be aligned roughly parallel to the underlying isobaths.

An ensemble of data acquired with the Nimbus 7 CZCS during the summer and fall seasons of 1979, 1980 and 1982 is analyzed in this study. The horizontal structure in bio-optical parameters determined from cloud-free portions of CZCS imagery are investigated using a Partitioned Empirical Orthogonal Function (PEOF) decomposition. The spatial partitions examined here consist of four zonal transects crossing the shelf/slope region at different latitudes. The specific goals of this analysis are:

1. To characterize the meridional and zonal spatial correlation structures of ocean color parameters (specifically optical depth  $1/K(490)$  in meters).
2. To compare the spatial scales and structures of optical variability highlighted by the PEOF





decompositions, and to relate these to the historical descriptive oceanography of the study region, and

3. To develop preliminary statistics related to the feasibility of joining data from different spatial partitions on the basis of partial subsamples, and to thus provide an optimal interpolation of satellite image data into cloud covered areas.



## II. OCEANOGRAPHY OF THE CENTRAL CALIFORNIA COAST

### A. THE STUDY DOMAIN

#### 1. Coverage

##### a. Area Domain

The region investigated in this project is located between 32 and 40N, and from the coast of California offshore to approximately 126W, Fig. 1. This area was selected because it contains water mass structures, including fronts, which strongly influence phytoplankton concentrations, and therefore the optical properties of the ocean water. Furthermore, an adequate sample of data was available for this area.

A subarea of this region is labelled Insert A in Figure 1 and presented in greater detail in Figure 2. Insert A is bounded by 34 to 38N, and by 126 to 120W. It is the primary study domain of this thesis. The background hydrography and dynamics of this region are described in subsections 2, 3, and 4 of this chapter.



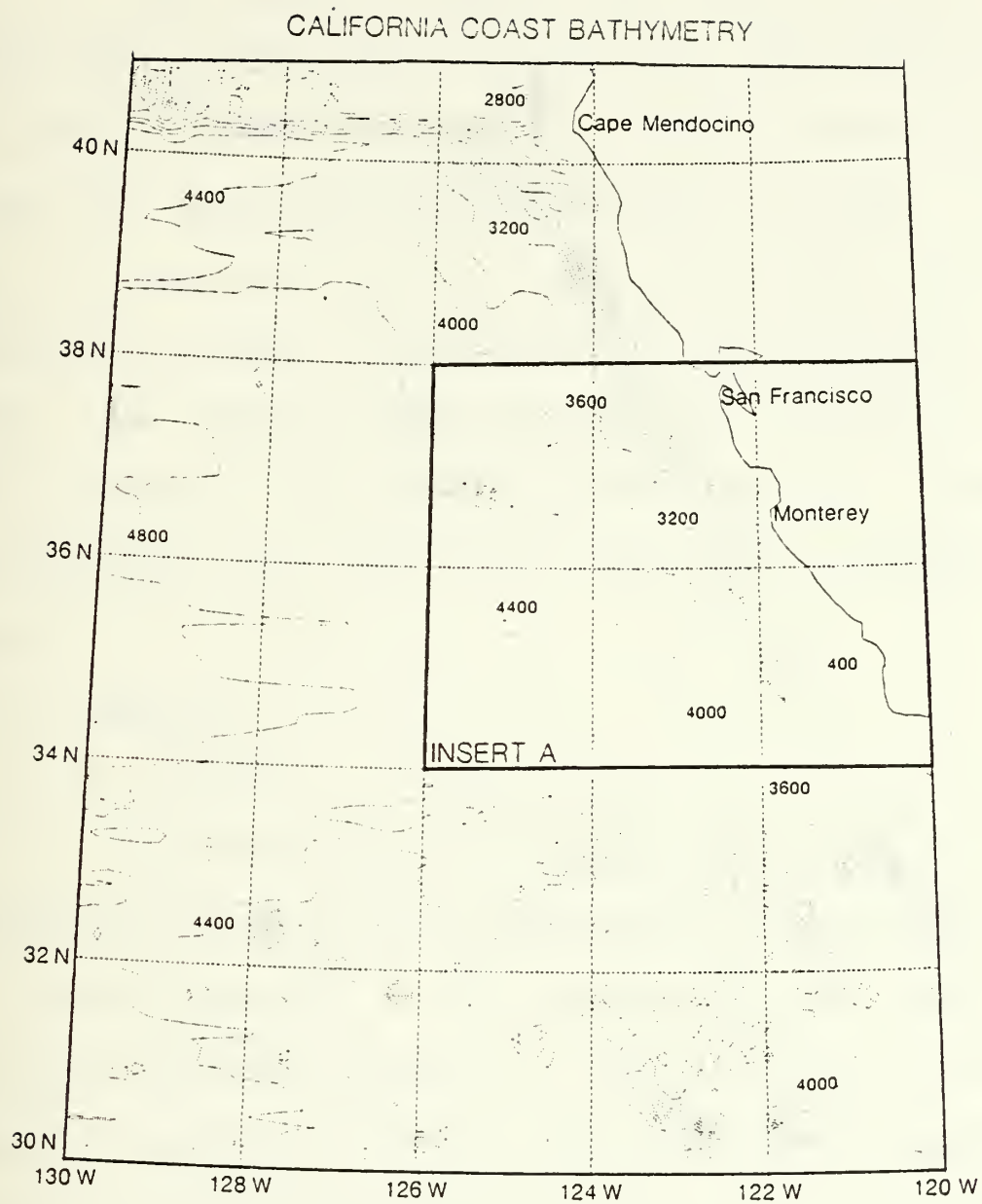


Figure 1. Ocean Bathymetry Off the California Coast (Synthetic Bathymetric Profiling System (SYNBAPS) Data Contoured at 400 m Intervals).



## b. Time Domain

In the time domain, the available CZCS data include scenes from summer through early fall seasons in 1979, 1980 and 1982. Originally, a single season ensemble of CZCS data (May through September 1980) was sought. However, the time span had to be expanded to three years to assemble a reasonably large sample size of cloud-free sub-scenes. The sample analyzed contains three scenes in 1979, eleven scenes in 1980 and eight scenes in 1982. Detailed characteristics of these CZCS images are presented in Appendix B.

## 2. Geometry

### a. Coastal

The California coast bounding the area of study is characterized by a steep, mountainous coastal range running roughly parallel to the coastline. The coastline stretching from San Francisco to Point Arguello is oriented roughly northwest to southeast, but is interrupted by Monterey Bay at 36 45'N and by smaller bays in the vicinity of Morro Bay at 35 20'N. No major rivers drain into this coastline, although many local rain-generated drainage creeks empty here.





## b. Bathymetry

The predominant orientation of the bathymetry is roughly northwest to southeast (parallel to the coast), Fig. 2. Interruptions of this orientation are evident in the vicinity of the Monterey Canyon, Point Sur and the Sur Canyon, the Davidson Seamount, the Taney Seamount and the Santa Lucia Banks and Escarpment off Point Arguello. A very abrupt shelf break is evident all along this section of the California coast. Isobaths tend to diverge south of Monterey, due to a broadening of the continental shelf and slope with distance south of Monterey.

## 3. Descriptive Oceanography

### a. Coastal Upwelling

Coastal upwelling is an oceanic phenomenon which has a pronounced impact upon many physical and biological processes. Predominantly southward winds during spring and summer off the central California coast, yield offshore surface Ekman transports, which forces compensation water to rise from depths of the order of 200 to 300 m (Smith, 1968).

The upwelling season off the coast of California is generally confined to the late spring through early fall. The onset of the seasonal upwelling commences in more



INSERT A

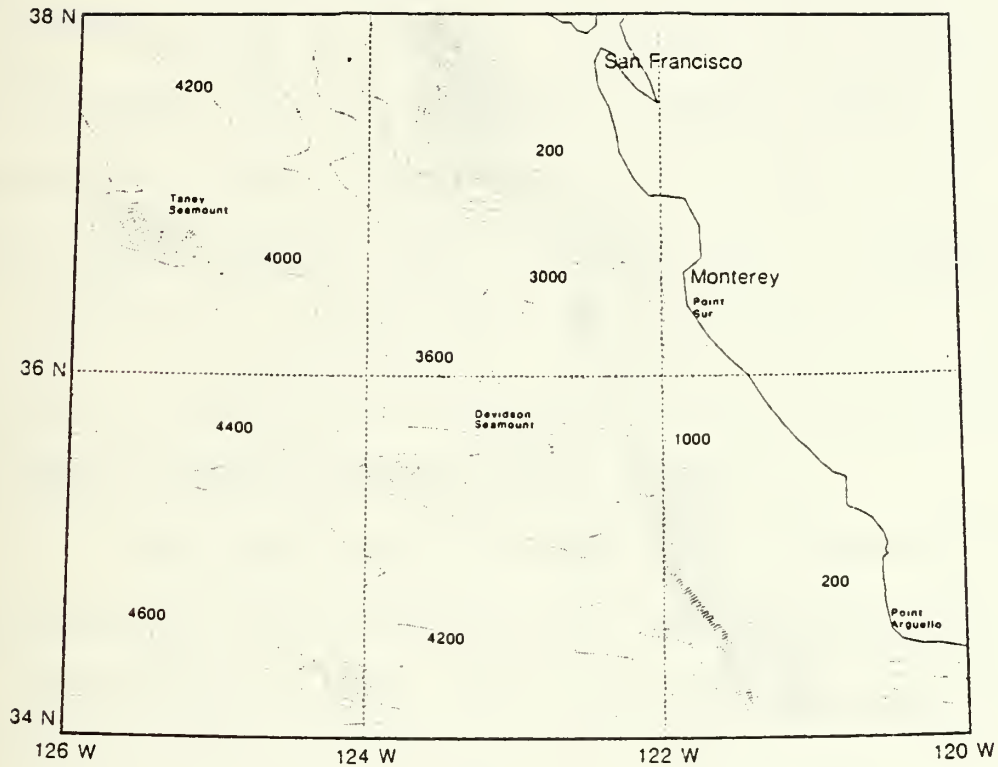


Figure 2. Ocean Bathymetry Off the California Coast  
(SYNBAPS Data, Contoured at 200 m Intervals).



southern waters off the California coast and progresses northward as the season unfolds (Yoshida and Mao, 1957; Wooster and Reid, 1963; Pavlova, 1966; Hickey, 1979). The CZCS data set spans the upwelling season and includes images from beyond this season into early winter.

Upwelling has a marked effect on the sea surface temperature, causing it to be much lower than would otherwise be normal for the latitude and season (Smith, 1968). The relatively lower temperatures are evident in IR images of the region (Johnson, 1980; Nestor, 1979). Accompanying this decrease in temperature is an increase in surface salinity, an upwelling property unique to the regime off the west coast of North America (Smith, 1968).

The oceanographic properties of upwelling have been documented in many areas of the world, but nowhere with the thoroughness of the work off California and Oregon. Ship and satellite observations have allowed us to identify seasons, centers, and the extent of the upwelling event along the west coast of North America. Traganza, et al. (1979) used combined satellite and shipboard observations to infer nutrient upwelling distributions off the coast of California. Frontal structures and mesoscale eddies that can



result from the upwelling phenomenon have been examined with relevance to Anti-Submarine Warfare (ASW) by Traganza (1979). The use of infrared (IR) imagery in the detection and description of upwelling was examined by both Johnson (1980) and Nestor (1979).

The introduction of nutrient rich waters to the nearshore euphotic zone greatly enhances the development of the in situ phytoplankton population. This enhancement in turn causes the upwelled water mass moving offshore to have distinctly different optical properties than adjoining offshore waters. The boundary (frontal region) between the upwelled water mass and the normal surface water mass is thus readily detectable and of great interest.

Nutrient enrichment off the California coastal zone is observed in the regions of upwelling events. These nutrients, which are classified as "biochemically new" on the basis of nitrate-to-phosphate ratios which approach 15:1, are brought to the surface from depths up to 300 m. By way of contrast, nutrients also present in the open ocean surface water approach 5:1 (Nestor, 1979). The added nitrates are a primary factor in the increase in phytoplankton concentrations during the upwelling season. Coastal





waters, on the whole, are fifty times more productive than open ocean waters and this difference can be increased during periods of upwelling (Sverdrup, et al., 1942). The phytoplankton concentrations, with their associated chlorophyll-like pigments, have a profound effect on the upwelled radiances measured by the CZCS, as discussed in Chapter III.

Another aspect of upwelling, and its relation to satellite data, is its effect on regional climate. The relatively cold sea surface temperature in upwelling zones cools the air above and thus increases its relative humidity. As a result, low stratus and fog commonly occur here in a shallow (marine) layer with warm air aloft. The frequent occurrence of low stratus and fog, seriously limits infrared and visible satellite coverage during the upwelling season. The cool sea water also contributes to a diurnal sea breeze by increasing the onshore-offshore pressure gradient. Onshore winds bring cool, moist air as far as 50 miles inland (Smith, 1968).

#### b. Currents

The California Current System may be discussed and studied in terms of four large scale currents:



the California Current, the California Undercurrent, the Davidson Inshore Current, and the Southern California Current (Hickey, 1979). The first three of these currents directly influence the study domain. Mesoscale currents associated with seasonal upwelling are also important here.

(1) California Current. The California Current is a broad wind-driven equatorward current which exhibits significant seasonal variations proportional to the changes in the wind field (Brown, 1974). Off Point Conception the mean annual location of the current axis is located 270 km offshore while the shoreward boundary extends to 200 km offshore. The current is of the order 700 km wide and flows south at 10 to 30 cm per second (Hickey, 1979).

The California Current is a continuation of the West Wind Drift in the North Pacific and flows southward along the California coast between 48 and 23N. It turns westward between 20 and 30N where it becomes part of the North Equatorial Current. This flow regime comprises the eastern extent of the anticyclonic NE Pacific Subtropical Gyre, which is centered near the Hawaiian Islands (Sverdrup, et al., 1942; Chelton and Davis, 1982).



(2) California Undercurrent. The California Undercurrent, also, referred to as the California Counter-current, is the poleward subsurface flow over the continental slope. Maximum poleward flow occurs during the summer and fall seasons at depths of 200 to 250 m (Pavlova, 1966 and Hickey, 1979). The flow can be described as a broad current with a central jet. It is this jet structure that is most often measured and referred to when applying specific values to the Undercurrent. The broad poleward flow has a geostrophic component alongshore near the shelf break of approximately 15 cm/sec (Coddington, 1979).

The flow appears to have a jet-like structure, both vertically and horizontally, and to extend to the bottom over the slope. The existence of a high speed jet core of the order of 20 to 70 km in width, was first suggested by Reid (1962, 1963). Subsequent direct measurements of these jets have produced values as high as 40 cm/sec off Northern Baja and values of 16 cm/sec off Washington (Wooster and Jones, 1970). The depth of the high-speed core varies seasonally. It rises from depths of 200 to 300 m to the surface during the late fall and winter north of Point Conception. Here it is referred as the Davidson Inshore



Current by many authors (Hickey, 1979; Pavlova, 1966; Ingraham, 1967). Event-scale fluctuations (of the order of 100 km and 10 days) in the flow appear to be correlated with the alongshore component of wind stress (Nelson, 1977).

The extent and time scale of continuous alongshore flow, and the width of the region of northward flow below 500 m, are important topics yet to be answered about the California Undercurrent (Hickey, 1979).

(3) Davidson Inshore Current. North of Point Conception, the poleward surface flow in the nearshore regions off the West Coast is known as the Davidson Inshore Current. It is associated with winter weather circulation patterns. As the southward winds weaken and tend toward a northwestward flow, the Davidson Inshore Current becomes established (Hickey, 1979). The current flows near the coast, usually within 100 km, well inshore of the California Current and is confined to the continental shelf and slope. Pavlova (1966) reported that north of Point Conception, the Davidson Inshore Current reaches its maximum development at depth (200 to 250 m) in the summer and autumn. In August the Davidson Inshore Current is scarcely noticeable at the surface despite active development at depth. Maximum





surface development is reached from October through April, i.e., late autumn to early spring. In December, the core of maximum velocity emerges at the surface and in the late spring it almost completely disappears (Reid, 1960; Reid, et al., 1958; Pavlova, 1966). Poleward velocities of up to 25 cm/sec were recorded (Reid and Swartzlose, 1962) within 80 km of central California in January.

The Davidson Inshore Current and the California Undercurrent are often discussed as though they were separate currents. Both currents transport Equatorial-type water northward at least as far as Cape Mendicino (Pavlova, 1966). Also, no subsurface maximum has been found in the flow of the Davidson Inshore Current. These characteristics support a view that the Davidson Current is simply the surface expression of the California Undercurrent, rather than a separate current superimposed on it.

(4) Other Currents. The presence of eddies throughout the the California Current System has been documented for many years (Bernstein, et al., 1977). The time scales for these eddies, as well as the processes responsible for their generation and subsequent dissipation, is an area of increasing study.



Between San Francisco and a point about half the distance to Point Conception, there is a permanent counterclockwise eddy that produces northward flow during all months except April (Brown, 1974). A second eddy just north of Point Conception forms during the summer months and makes northward flow continuous from Point Conception to San Francisco (Hickey, 1979). Willmott (1983) has shown that these features may be produced by flow separation of the California current in the vicinity of major coastal capes.

Reid, et al. (1963) made direct measurements of an eddy (90 km in diameter) off the northern coast of Baja California. Hypotheses for eddy formation discussed in their paper are as follows:

(1) The process of upwelling and the offshore movement of the colder, more saline waters might degenerate into eddies. The lateral shear between the upwelling flow away from the coast and the California Current and Undercurrent (barotropic instability) could produce eddy structures. Temperature and salinity differences set up strong baroclinic zones along the upwelling boundaries which could result in eddy formation. (Sverdrup and Fleming, 1941)



(2) The offshore surface flow during upwelling should produce a counter current (Munk, 1950). If there is substantial north-south variation in the intensity of the winds, then separate countercurrents of different strengths might occur along the coast.

(3) A second hypothesis proposed by Reid, et al. (1963), is that the deeper countercurrent may transfer momentum upward to the surface layers, at times when, or in regions where, a surface current does not prevail. This could cause spot intrusions of colder circulating waters that form eddies where neither surface countercurrents nor coastal upwelling produce them.

Additionally, the effects of bottom steering by coastal topography, and the associated trapped motions must be considered when discussing eddy formation. (Hurlburt, 1974; Johnson, 1982; Willmott, 1983)

#### c. Water Masses

Descriptions of the water masses that contribute to the California Current System are given in Tibby (1941), Sverdrup, et al., (1942) and Reid, et al., (1958). Four major sources are discussed by the authors:

(1) Subarctic Water Mass - from the north.

(2) Central Water Mass - from the west and northwest.



(3) Equatorial Water Mass - from the south.

(4) Water derived from upwelling sources.

These sources were simplified in Tibby (1941) and Sverdrup, et al., (1942) into two extreme sources named "Subarctic North Pacific" and "Equatorial Pacific".

The percent of each water mass comprising a sample can be defined by entering Figure 3 with a T-S pair. However, the determination of percentage composition by this means cannot be used for water above depths of about 100 m. This restriction is due to vertical mixing in the nearsurface layer related to the effects of wind and local changes due to heat and mass fluxes across the air-sea interface. Any mixing along surfaces of constant  $\sigma_t$  would be severely masked in these shallower depths by the effects of turbulent vertical mixing. Also, below 1000 m the differences in the T-S relationships of the two extreme water masses are negligible. For intermediate depths, as might be expected, the percentage of equatorial water decreases in the direction of northward flow. The Undercurrent is characteristically warmer and more saline than the California Current, and it has a salinity maximum on the  $\sigma_t = 26.54$  surface. Off





Monterey and below 800 m, the water is greater than 60% Equatorial Water and this percentage increases both with depth and movement towards lower latitudes (Brown, 1974).



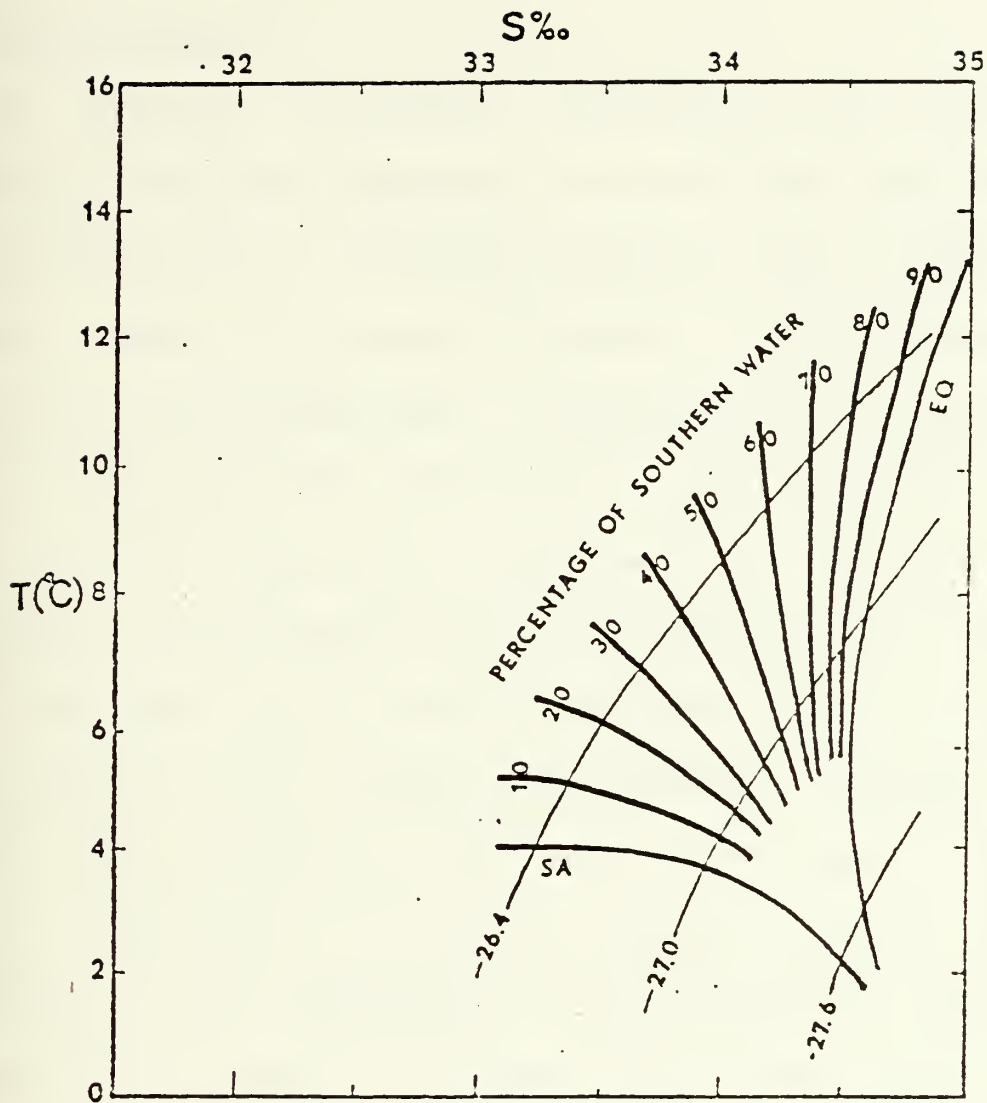


Figure 3. Graph Showing T-S Curves Defining Subarctic Water and Equatorial Pacific Water, and Curves for Various Percentages of Equatorial Pacific Water Assuming Mixing Along Surfaces of Equal  $\sigma_t$  (Brown, 1974).



### III. CZCS OCEAN COLOR IMAGES AND UPPER OCEAN OPTICAL PROPERTIES

#### A. INTRODUCTION

The physical processes of absorption and scattering relate the upwelling radiance just beneath the sea surface to the constituents of the water (Gordon, 1976). Except for coastal waters and waters influenced by river discharge, biological constituents play a dominant role in these processes (Smith and Baker, 1978; Jerlov, 1976). Optically, the most important biological constituent is phytoplankton, microscopic plant organisms that photosynthesize and make up the first link of the oceanic food web (Steele, 1970). Chlorophyll-a is the dominant photosynthetic pigment, and absorbs light strongly in the blue and red regions of the visible spectrum (400 to 700 nm) (Hovis, et al., 1980). Therefore, as the concentration of phytoplankton increases, the color of the water is shifted toward green hues from the deep blue of its pure state. By measuring upwelled radiance (backscattered daylight) in specific spectral bands, we can determine the concentrations of phytoplankton pigments in the ocean (Gordon, et al., 1980; Gordon, et al., 1983).



This chapter first describes the CZCS sensor and its capabilities, and then the measured signal is discussed. Algorithms that are currently applied to this signal to correct for atmospheric effects are discussed. Finally, the algorithms designed to convert the corrected radiance values to phytoplankton concentrations,  $C$ , and irradiance attenuation coefficient,  $k$ , are presented.

## B. SYSTEM DESCRIPTION

### 1. The Nimbus-7 Coastal Zone Color Scanner (CZCS)

The CZCS was built by the Ball Brothers Research Corporation to NASA's specifications. The instrument is a spatially imaging multispectral scanner. Six spectral bands are precisely coregistered and internally calibrated. The swath width of the CZCS is slightly more than 1600 km. Characteristics of its five visible (443, 520, 550, 670, 750 nm) and one thermal IR (10.5 to 12.5  $\mu$ m) channels are summarized in Table I. The CZCS has an active scan of 78 degrees centered on nadir and a field of view of 0.0485 degrees, yielding a geometric instantaneous field of view of 825 m (at nadir) from a spacecraft altitude of 955 km. It can tilt the scan plane 20 degrees from nadir in 2 degree increments along the satellite track to minimize the influence of





direct sun glint. The Nimbus-7 spacecraft is in a sun-synchronous orbit with ascending node near local noon.

TABLE I  
Characteristics of the CZCS  
(Hovis, et al., 1980)

Band Number	Wavelength (nm)	Gain	Saturation Radiance (mW/cm <sup>2</sup> sr μm)	Measured signal/noise
1	433 to 453	3	5.41	158/1
		2	7.64	
		1	9.23	
		0	11.46	
2	510 to 530	3	3.50	200/1
		2	5.10	
		1	6.20	
		0	7.64	
3	540 to 560	3	2.86	176/1
		2	4.14	
		1	5.10	
		0	6.21	
4	660 to 680	3	1.34	118/1
		2	1.91	
		1	2.32	
		0	2.88	
5	700 to 800		23.90	350/1
6	10,500 to 12,500			0.22 K*

\* Noise equivalent temperature difference at 270 K.



## 2. Measured Signal

The designed purpose of the CZCS experiment was to provide estimates of the nearsurface concentrations of phytoplankton pigments (defined to be chlorophyll-a and its associated degradation products, called "phaeopigments") by measuring the spectral radiance backscattered out of the ocean (Gordon and Clark, 1981). The radiance scattered out of the ocean that reaches the sensor is a very small portion of the total radiance received. Consider the physical setting where solar irradiance  $F_0(\lambda)$  at a wavelength  $\lambda$  is incident on the top of the atmosphere at a zenith angle  $\theta_0$  and azimuth  $\phi_0$  and the scanner is detecting total radiance  $L_t(\lambda)$  at a nadir angle  $\theta$  and azimuth angle  $\phi$ .  $L_t(\lambda)$  consists of radiance which has been scattered by the atmosphere and sea surface, radiance generated by Fresnel reflection of the direct (unscattered) solar irradiance from the rough ocean surface (sun glint), and solar irradiance scattered from beneath the sea surface  $t_d(\lambda)L_w(\lambda)$ , where  $t_d(\lambda)$  is the diffuse transmittance.

Observations (Gordon, et al., 1983; Gordon, et al., 1980) produce values of  $L_t(\lambda)$  in the blue that are ten times greater than  $L_w(\lambda)$ . These effects are principally due to



scattering by the air (Rayleigh scattering) and by microscopic particles suspended in the air (aerosol scattering), both of which increase the radiance detected at the sensor. Fresnel reflection (sun glint) can be ignored as the tilting capability of the CZCS minimizes its effect. However the scattering effects, both Rayleigh and aerosol, must be removed from  $L_t(\lambda)$  to give usable values for the upwelled radiance  $L_w(\lambda)$ .

### C. CZCS GEOPHYSICAL ALGORITHMS

#### 1. Atmospheric Corrections

From the signal description in section A of this chapter, we can construct the following formula

$$L_t(\lambda) = L_r(\lambda) + L_a(\lambda) + t_d(\lambda)L_w(\lambda) \quad (1)$$

where

$L_t$  = Total radiance

$L_r$  = Radiance due to Rayleigh scattering

$L_a$  = Radiance due to aerosol scattering

$L_w$  = Upwelled radiance from beneath the sea surface

$t_d$  = Diffuse transmittance of the atmosphere

$\lambda$  = Wavelength



As previously mentioned  $L_t$  is the total radiance measured by the CZCS. The Rayleigh scattering term can be expressed as

$$L_r(\lambda) = \frac{F_o(\lambda)}{4\pi} \frac{\tau_r(\lambda)}{\cos \theta} \left[ P_r(\alpha_-) + \{\rho(\theta) + \rho(\theta_o)\} P_r(\alpha_+) \right] T_{O_3}(\lambda), \quad (2)$$

Where

$F_o$  = The instantaneous extraterrestrial solar irradiance.

$\tau_r$  = The Rayleigh optical thickness of the atmosphere.

$P_r$  = The Rayleigh scattering phase function.

$\alpha_-$  = The scattering angle through which photons are backscattered from the atmosphere to the sensor without interacting with the sea surface.

$\alpha_+$  = The forward scattering angle of those photons which are scattered in the atmosphere toward the sea surface (sky radiance) and then specularly reflected from the surface into the field of view of the sensor ( $\rho(\theta_o)$  term) as well as photons which are first specularly reflected from the sea surface and then scattered by the atmosphere into the field of view of the sensor ( $\rho(\theta)$  term).

$\rho$  = The Fresnel reflectance of the air-sea interface.





$T_{O_3}$  = The two-way ozone transmittance of the atmosphere.

$\theta$  = The sensor zenith angle at the observed point on the sea surface.

$\theta_0$  = The solar zenith angle at the observed point on the sea surface.

The aerosol scattering term is found using the 670 nm channel, where there is only a negligibly small contribution by the  $L_w$  term. (This is referred to as the "black ocean" assumption.) We calculate aerosol radiance at  $\lambda = 670$  as

$$L_a(670) = L_t(670) - L_r(670) \quad . \quad (3)$$

The key assumption in this algorithm is that the ratio of aerosol wavelengths is constant over a scene, and is given as

$$\epsilon(\lambda, 670) = \frac{L_a(\lambda)}{L_a(670)} \quad . \quad (4)$$

$\epsilon$  is calculated using either simultaneous direct radiance measurement from a ship, or upwelled radiance values modelled at a clear water pixel (Gordon and Clark, 1981). The latter method is discussed in section 2 of this chapter.



Returning to equation (1),  $t_d(\lambda)$  is the diffuse transmittance of the atmosphere and sea surface, which may be approximated as

$$t_d(\lambda) = \frac{[1 - \rho(\theta)]}{m^2} \exp \left[ - \left\{ \frac{\tau_r(\lambda)}{2} + \tau_{O_3}(\lambda) \right\} / \cos \theta \right], \quad (5)$$

where all terms have been previously defined except  $m$ , which is the index of refraction of water relative to air and is assumed to be 4/3 for the wavelengths (400 - 700 nm).

We have now developed the basics for extracting the upwelled radiance values,  $I_w$ , from the CZCS detected signal,  $L_t$ .

## 2. Clear Water Radiance

The scene constant,  $\epsilon$ , given in equation (4) is calculated as

$$\epsilon(\lambda, \lambda_o) = (\lambda / \lambda_o)^n \frac{F_o(\lambda) \exp[-\tau_{O_3}(\lambda)(\sec \theta + \sec \theta_o)]}{F_o(\lambda_o) \exp[-\tau_{O_3}(\lambda_o)(\sec \theta + \sec \theta_o)]}, \quad (6)$$

where  $n$  is called the Angstrom coefficient. Equation (6) can be rewritten as

$$\epsilon(\lambda, \lambda_o) = (\lambda / \lambda_o)^n \frac{F_o(\lambda)}{F_o(\lambda_o)} \frac{T_{O_3}(\lambda)}{T_{O_3}(\lambda_o)}, \quad (7)$$



where  $T_{O_3}(\lambda) = \exp[-\tau_{O_3}(\lambda)(\sec \theta + \sec \theta_o)]$  and where for the CZCS  $\lambda_o = 670$  nm.

Gordon and Clark (1981) developed the concept of clear water radiance for atmospheric correction of CZCS imagery. The strategy employed in this study was to find an area of the image that could be assumed to have a chlorophyll concentration less than  $0.25 \text{ mg/m}^3$ . At this low concentration,  $L_w$  at 520 and 550 nm are assumed to be essentially constant for a given solar elevation. Then, given these "clear water values" of  $L_w(\lambda)$  at one position,  $L_a(\lambda)$  is calculated using equation (1).  $\epsilon(\lambda, 670)$  are found from equations (4) using the computed  $L_a(\lambda)$  and  $L_a(670)$  value. Finally, rearranging equation (7) we find that

$$n(\lambda) = \frac{\ln \left\{ \epsilon(\lambda, \lambda_o) / \left[ \frac{F_o(\lambda) T_{O_3}(\lambda)}{F_o(\lambda_o) T_{O_3}(\lambda_o)} \right] \right\}}{\ln(\lambda/\lambda_o)} \quad (8)$$

Values for  $n$  at 520 and 550 nm ( $n(520)$  and  $n(550)$ ) are computed, then averaged to estimate  $n(443)$ . The Angstrom coefficient at 443 nm cannot be directly measured in this way



because  $L_w(443)$  is highly sensitive to even minute fluctuations in chlorophyll concentrations at low concentration.

An important aspect of this algorithm is that neither surface measurements of  $L_w(\lambda)$ , nor any properties of the aerosol are required to implement the atmospheric correction.

### 3. Bio-optic Parameters

#### a. Chlorophyll Concentrations

Determination of chlorophyll concentrations

$C$  from ratios of  $L_w(\lambda)$  relates the surface value of  $C$  to the ratio of the upwelled radiance at two different wavelengths (Morel and Prieur, 1977; Gordon and Clark, 1981). The basis for this is that to a first approximation  $L_w$  is proportional to the ratio of the volume backscattering coefficient,  $B(\lambda)b(\lambda)$ , and the volume absorption coefficient,  $a(\lambda)$ , of the water plus its constituents (Gordon, et al., 1983). The contributions from the individual constituents can be summed to provide a total value for each optical coefficient. Moreover the contributions to  $B(\lambda)$ ,  $b(\lambda)$ , and  $a(\lambda)$  arising from phytoplankton and their pigments are assumed to be proportional to chlorophyll concentration  $C$ . Taking a ratio of  $L_w$  at two different wavelengths and applying the assumption  $L_w(\lambda) \propto B(\lambda)b(\lambda)/a(\lambda)$ , we obtain





$$\frac{L_w(\lambda_1)}{L_w(\lambda_2)} = \frac{B(\lambda_1)b(\lambda_1)a(\lambda_2)}{B(\lambda_2)b(\lambda_2)a(\lambda_1)} \quad (9)$$

Because of the non-linearities involved in the individual constituent contributions to  $B(\lambda)$ ,  $b(\lambda)$ , and  $a(\lambda)$ , we appeal to a heuristic observation that

$$\frac{L_w(\lambda_1)}{L_w(\lambda_2)} = R(C, K, \dots) \quad (10)$$

i.e., the ratio of two upwelled radiances is a function  $R$  of the chlorophyll concentration,  $C$ , and the diffuse attenuation coefficient,  $k$ , as well as other optically important constituents of seawater. It was then assumed that  $R$  is related to  $C$  through a log linear model of the form

$$\text{Log } C = \text{Log } A_0 + A_1 \text{ Log } R(\lambda_1, \lambda_2) \quad (11)$$

which was empirically fit to observations to determine coefficients  $A_0$  and  $A_1$ . Thus, pigment concentrations are computed from CZCS data using the equation

$$C = A_0 R^{A_1} \quad (12)$$

The empirical coefficients presented by Gordon, et al. (1983) have been adopted by NASA and are:

Case I:  $C \leq 1.5$  for  $R(443, 550)$

$$A_0 = 1.1297959$$

$$A_1 = -1.71$$



Case II:  $C > 1.5$  for  $R(443,550)$ , but  
 $C < 1.5$  for  $R(520,550)$

$$A_0 = 1.1297950$$

$$A_1 = -1.71$$

Case III:  $C > 1.5$  for  $R(520,550)$

$$A_0 = 3.3265955$$

$$A_1 = -2.44$$

where  $C$  is in  $\text{mg/m}^3$ .

#### b. Diffuse Attenuation Coefficient

A similar development of the algorithm for the determination of the diffuse attenuation coefficient,  $k(\lambda)$ , is given by Austin (1981). Like the chlorophyll concentration algorithm, this algorithm derives a value based on the ratio of  $L_w$  at two wavelengths.  $k$  can be defined as

$$k(\lambda) = \frac{-1}{F(\lambda, z)} \frac{dF(\lambda, z)}{dz} \quad (13)$$

Equation (13) can be solved for irradiance  $F(\lambda, z)$  to obtain

$$F(\lambda, z_2) = F(\lambda, z_1) \exp \left[ -k(\lambda)(z_2 - z_1) \right] \quad (14)$$

Hence

$$k(\lambda) = \frac{1}{z_2 - z_1} \ln \left[ \frac{F(\lambda, z_2)}{F(\lambda, z_1)} \right] \quad (15)$$



Empirically derived coefficients from spectral data yield

$$k(490) = 0.0833 \left[ \frac{L_w(443)}{L_w(550)} \right]^{-1.491} + 0.022 \text{ m}^{-1} \quad (16)$$

(Austin, 1981).

#### D. SIGNAL FACTORS

Many factors have been accounted for with these algorithms by either mathematical and empirical models or heuristic assumptions. The determination of the total radiance values in the first four channels of the CZCS allows us to apply the corrections to determine upwelled radiance. The constituents of the water which affect its absorption and scattering properties are then empirically derived.

The distribution of phytoplankton is controlled by many local, mesoscale and global factors, including solar radiation, global weather patterns, and ocean circulation patterns. The mesoscale events of upwelling or eddy circulation can have important regional effects. These factors are too numerous and varied to be modelled on a theoretical basis. However, empirical modelling can produce relatively accurate and consistent results.

The measurement of these bio-optical parameters from space allows us to remotely determine their relationships to



physical events in the regions under study. Time scales, spatial scales and specific features can be discerned using the known (or hypothesized) relationships between inherent optical properties of the ocean water constituents and the forcing involved in their distribution.



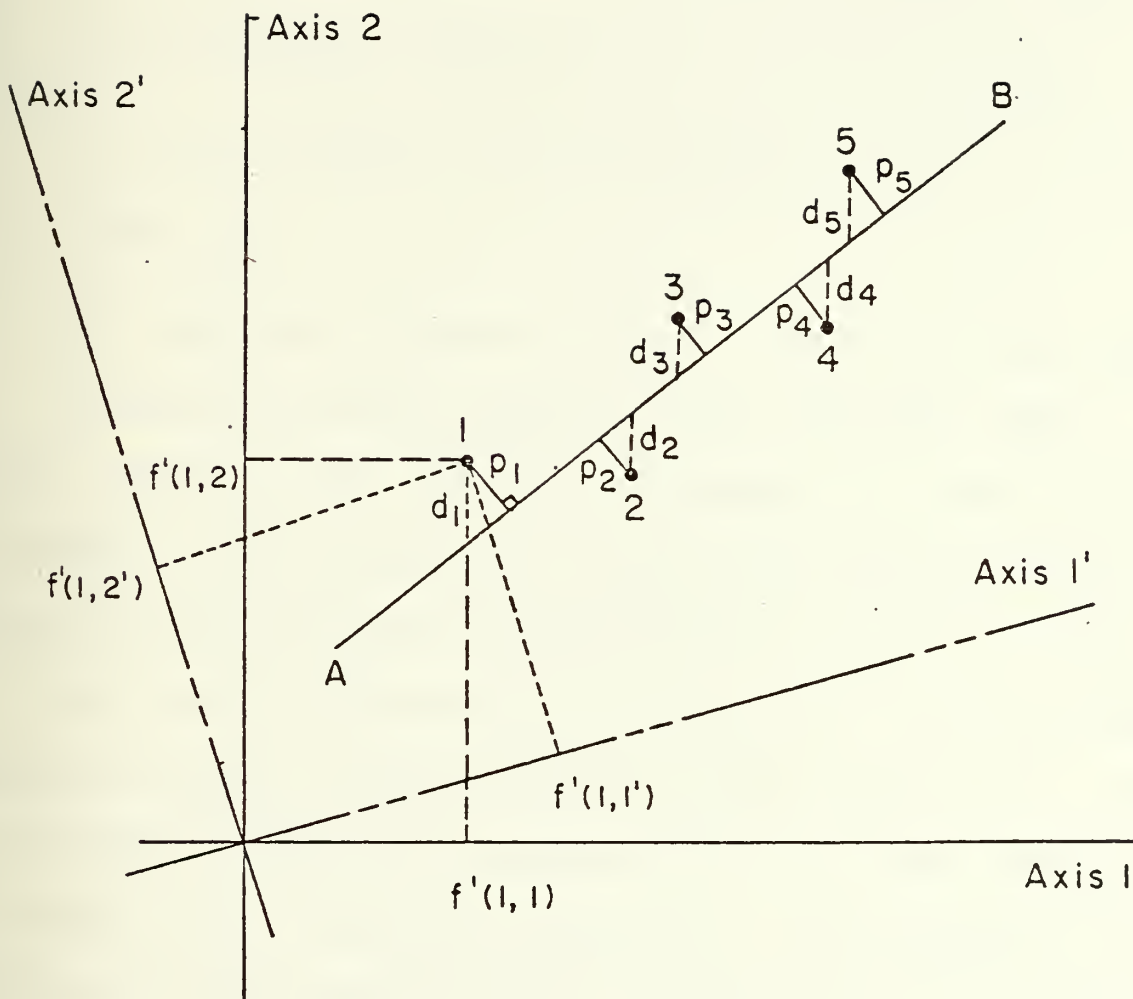


#### IV. EMPIRICAL ORTHOGONAL FUNCTION ANALYSIS METHODS

##### A. INTRODUCTION

The concept of principal component analysis has been presented and utilized in different forms over the past eighty years. Fitting a line to a data set was usually accomplished using a least squares method. Distances to this line from each point were measured parallel to an arbitrarily set axis. From the early work of Pearson (1901), this method was adapted so that the perpendicular distances from each point to the best fit line were measured. Figure 4 illustrates this difference and shows that the first method is tied to a coordinate system while the Pearson approach is independent of coordinate systems. This new method laid the foundation for the development of principal component decomposition techniques. These techniques have since been utilized in many forms and referred to by similar names in a number of disciplines. Applications in psychology by Eckert and Young (1936, 1939), although somewhat different in their development, contain the essential elements of data analysis and principal component decomposition as used in geophysical disciplines today.







Meteorological applications by Lorenz(1956), Kutzbach(1967), and Rinne, et al.(1979) demonstrated the convenience of representing a large climatological field with a smaller set of values. These areas include:

- (1) Non-linear statistical prediction (Lorenz, 1956),
- (2) Non-linear dynamical prediction (Lorenz, 1956),
- (3) 500 mb height field representation (Rinne, et al., 1979), and
- (4) Sea level pressure, surface temperature, and precipitation pattern representations (Kutzbach, 1967)

Other uses of EOF analysis techniques in oceanography include the representation of ocean color spectra (Mueller, 1976) and of wave spectra (Aranuvachupun and Thorton, 1983).

The principal difficulties encountered in principal component analysis problems relates to the selection of the 'meaningful' subset of components and to their physical interpretation. Methods of selection of the principal components are also widely varied. Preisendorfer, et al.(1981) discussed two methods which together involve seventeen different testing rules. Empirical selection of a cutoff value for variance or forcing factors can also be utilized.



Visual inspection of the data which leads to a clear cut (albeit subjective) choice is also an option.

The enormous data volume inherent in satellite data sets begs application of the techniques of principal component analysis. Principal component analysis techniques often allow the efficient representation of a large data set by its first few principal components with a negligible loss of information. The advantage gained is reduction in the number of variables needed to represent the data. Reducing a data set to its principal components can also aid in the interpretation of the data by separating noise from the signal. Principal component analysis theory can be applied to preliminary explorations within a relatively unstructured domain of knowledge, one in which the fundamental laws governing the processes under study are still being defined. (Preisendorfer, et al., 1981)

A brief review of the EOF analysis follows to provide background for the later analyses. The reader is referred to Preisendorfer, et al. (1981) for a more complete development and history. The following matrix algebra notation is adopted throughout this thesis.

1. No underscore denotes a scalar.....X
2. A straight line underscore denotes a vector....X





3. A curved line underscore denotes a matrix..... $\underline{\underline{X}}$
4. A straight line overbar denotes a mean value... $\bar{X}$
5. The use of a superscript "T" denotes a matrix transpose.

## B. EOF EQUATIONS

### 1. Raw Data Conversion

Following Preisendorfer, et al. (1981) let  $\underline{\underline{F'}}$  be the raw (uncentered) data matrix,

$$\underline{\underline{F'}} = \begin{bmatrix} f'(1,1) & f'(1,2) & \dots & f'(1,p) \\ f'(2,1) & f'(2,2) & \dots & f'(2,p) \\ \vdots & \vdots & & \vdots \\ f'(n,1) & f'(n,2) & \dots & f'(n,p) \end{bmatrix}, \quad (17)$$

where  $f'(i,j)$  is the measurement in the  $i$ 'th time point and  $j$ 'th spatial position. In the present investigation, each member of  $\underline{\underline{F'}}$  will correspond to an optical parameter measured by the CZCS at a particular time and spatial position. To convert the raw data matrix,  $\underline{\underline{F'}}$ , to a centered data matrix,  $\underline{\underline{F}}$ , the temporal means are computed and subtracted from  $\underline{\underline{F'}}$ . The temporal mean vector  $\underline{\bar{f}}(x)$  is calculated as

$$\underline{\bar{f}}(x) = \frac{1}{n} \sum_{t=1}^n f'(t,x) \quad (18)$$

The centered data matrix,  $\underline{\underline{F}}$ , is then defined as



$$F = \begin{bmatrix} f'(1,1) - \bar{f}(1) & f'(1,2) - \bar{f}(2) & \dots & f'(1,p) - \bar{f}(p) \\ f'(2,1) - \bar{f}(1) & f'(2,2) - \bar{f}(2) & \dots & f'(2,p) - \bar{f}(p) \\ \vdots & \vdots & & \vdots \\ f'(n,1) - \bar{f}(1) & f'(n,2) - \bar{f}(2) & \dots & f'(n,p) - \bar{f}(p) \end{bmatrix} \quad (19)$$

Each element  $f(t,x)$  of  $\underline{F}$  consists of a raw data measurement with the temporal mean removed. The centered data matrix,  $\underline{F}$ , can be written as

$$\underline{F} = \underline{F}' - \underline{\bar{F}} \quad (20)$$

where  $\underline{\bar{F}}$  is the matrix containing as rows the transpose of the mean vector  $\underline{\bar{f}}^T = [\bar{f}(1), \bar{f}(2), \dots, \bar{f}(p)]$ .

## 2. Principal Direction of Scatter

To find the direction,  $\underline{e}_1$ , (in the space domain) along which the scatter (or variance) of the data set is greatest, consider the projection of the data vectors  $\underline{f}(t)$  along an arbitrary direction  $\underline{e}_1$

$$D(t, \underline{e}_1) = \underline{f}^T(t) \underline{e}_1 \quad (21)$$



Squaring this length and summing over all  $n$  observations, gives a measure of the scatter of the data along the direction,  $\underline{e}_1$ , namely

$$D^2(\underline{e}_1) = \sum_{t=1}^n \left[ \underline{f}^T(t) \underline{e}_1 \right]^2 . \quad (22a)$$

The righthand side of (22a) can be expanded to yield

$$D^2(\underline{e}_1) = \sum_{t=1}^n \left[ \underline{e}_1^T \underline{f}(t) \underline{f}^T(t) \underline{e}_1 \right] \quad (22b)$$

$$= \underline{e}_1^T \left[ \sum_{t=1}^n \underline{f}(t) \underline{f}^T(t) \right] \underline{e}_1 . \quad (22c)$$

The next step is to define the "Scatter Matrix",  $\underline{S}$ ,

$$\underline{S} = \underline{F}^T \underline{F} , \quad (23)$$

with elements

$$s(i,j) = \sum_{t=1}^n \underline{f}(t) \underline{f}^T(t) . \quad (24)$$

Expanding the above equation produces for each member of  $\underline{S}$

$$s(i,j) = \sum_{t=1}^n (\underline{f}'(t,i) - \bar{\underline{f}}(i)) (\underline{f}'(t,j) - \bar{\underline{f}}(j))^T . \quad (25)$$

If the matrix is normalized by dividing by  $(p - 1)$ , then when  $i \neq j$ , the members of  $\underline{S}$  are covariance values, and when  $i = j$  (the trace of the matrix) the members are variance values (i.e. each element is the variance of  $f$  at a single spatial grid point). The scatter matrix,  $\underline{S}$ , is symmetric.



Therefore, it generally has  $p$  non-negative eigenvalues  $\lambda_j$  ( $j = 1, \dots, p$ ) and associated eigenvectors  $\underline{e}_j$  ( $j = 1, \dots, p$ ), provided that the rank of  $\underline{S}$  is equal to  $p$ .

### 3. Principal Component, Eigenvalue and Eigenvector Representation

The first principal component of an observation vector  $\underline{f}$  is defined to be the linear combination

$$a_1 = e_{11}f_1 + e_{12}f_2 + \dots + e_{1p}f_p = \underline{e}_1^T \underline{f} \quad (26)$$

whose sample variance

$$s_{a_1}^2 = \sum_{i=1}^p \sum_{j=1}^p e_{1i}e_{1j} s_{ij} = \underline{e}_1^T \underline{S} \underline{e}_1 \quad (27)$$

is a maximum for all possible vectors  $\underline{e}$ , subject to the constraint that

$$\underline{e}_1^T \underline{e}_1 = 1 \quad (28)$$

Introducing the Lagrange multiplier  $\lambda_1$ , the maximum variance must satisfy

$$\begin{aligned} \frac{\partial}{\partial \underline{e}_1} \left[ s_{a_1}^2 + \lambda_1 (1 - \underline{e}_1^T \underline{e}_1) \right] &= \frac{\partial}{\partial \underline{e}_1} \left[ \underline{e}_1^T \underline{S} \underline{e}_1 + \lambda_1 (1 - \underline{e}_1^T \underline{e}_1) \right] \\ &= 2(\underline{S} - \lambda_1 \underline{I}) \underline{e}_1 = \underline{0} \end{aligned} \quad (29)$$

For non-trivial solutions,  $\lambda_1$ , must be chosen such that

$$\left| \underline{S} - \lambda_1 \underline{I} \right| = 0 \quad (30)$$





and, therefore,  $\lambda_1$ , is an eigenvalue of  $S$ , and  $\underline{e}_1$  is its associated eigenvector. Furthermore

$$S \underline{e}_1 = \lambda_1 \underline{e}_1, \quad (31)$$

and since  $\underline{e}_1^T \underline{e}_1 = 1$

$$\underline{e}_1^T S \underline{e}_1 = \lambda_1 = s_{a_1}^2, \quad (32)$$

i.e., the first eigenvalue of  $S$  is interpretable as the sample variance of  $S$ . If we expand this development to the other eigenvalues and eigenvectors of  $S$ , we obtain

$$E = [\underline{e}_j]; j = 1, \dots, p, \quad (33)$$

the eigenvector matrix and

$$L = D[\lambda_j]; j = 1, \dots, p, \quad (34)$$

the diagonal eigenvalue matrix.

Thus,

$$S E = E L. \quad (35)$$

In terms of  $E$  the constraint  $\underline{e}_1^T \underline{e}_1 = 1$  becomes  $E^T E = I$ . Where  $I$  is the identity matrix. Therefore, if we multiply both sides of equation (35) by  $E^T$  we obtain

$$S = E L E^T. \quad (36)$$



Now, using the definition provided for  $\underline{f}$  and equation (20), the principal component matrix can be defined as

$$\underline{A} = \underline{F} \underline{E} \quad . \quad (37)$$

This is the desired principal decomposition of  $F$  where

$$\underline{A}^T \underline{A} = (\underline{F} \underline{E})^T \underline{F} \underline{E} \quad (38a)$$

$$= \underline{E}^T \underline{F}^T \underline{F} \underline{E} \quad (38b)$$

$$= \underline{E}^T \underline{S} \underline{E} \quad (38c)$$

$$= \underline{E}^T \underline{E} \underline{L} \quad (38d)$$

$$= \underline{L} \quad . \quad (38e)$$

## C. PARTITIONED EOF ANALYSIS

### 1. Purpose

The EOF analysis method outlined above works very well for a large continuous data set. However, geophysical data sets are rarely continuous. In the case of satellite data, cloud cover results in many gaps. Sometimes these gaps can be bridged by linear interpolation, e.g., when they are small and surrounded by good data. Often this is not the case and so a scheme of utilizing non-continuous data is necessary. Here, the purposes of partitioning are:



(1) To maximize the sample size in the presence of cloud cover, thus allowing statistical computations for subregions;

(2) To highlight spatial structures of variance features locally, before absorbing them into the modes of the overall domain; and

(3) To achieve computational convenience.

Briefly, partitioning permits EOF analysis using small subsets of the overall data set. These subsets are partitioned to yield continuous data in each subdomain. An EOF analysis is completed on each individual subset, and an eigenvalue matrix, an eigenvector matrix and a principal component matrix are obtained. The next step is to perform an EOF analysis to join the principal components of the subsets. This second EOF analysis produces 'joining functions' which relate two non-overlapping subsets.

## 2. Rules and Methods

When performing the partition of any data set certain rules must be observed to maintain the statistical reliability of the computations. Two obvious and basic rules are:



(1) The minimum partition size (number of pixels) must be greater than or equal to the sample size (i.e., if there are 25 sample days each partition must have 25 or more pixels). In practice, the spatial dimension will be required to be significantly greater than the sample size.

(2) The partition size should not be so small that the spatial structure is dominated by noise (e.g., a partition boundary will not be placed in a major feature, such as a front or eddy of length scale much less than the partition size).

The methods involved in the partitioning are subject to the above principles, together with a general understanding of the physical processes occurring in the study domain. Four tracklines at 35N, 35 22'N, 35 40'N and 35 53'N, were used to aid in this initial trial of partitioning (Fig. 5). The radiance values and computed optical parameters along each trackline were plotted versus distance from the coast. These plots were aligned to pictorially represent the data and its gaps (due to clouds). The partitioning scheme was





# INSERT A

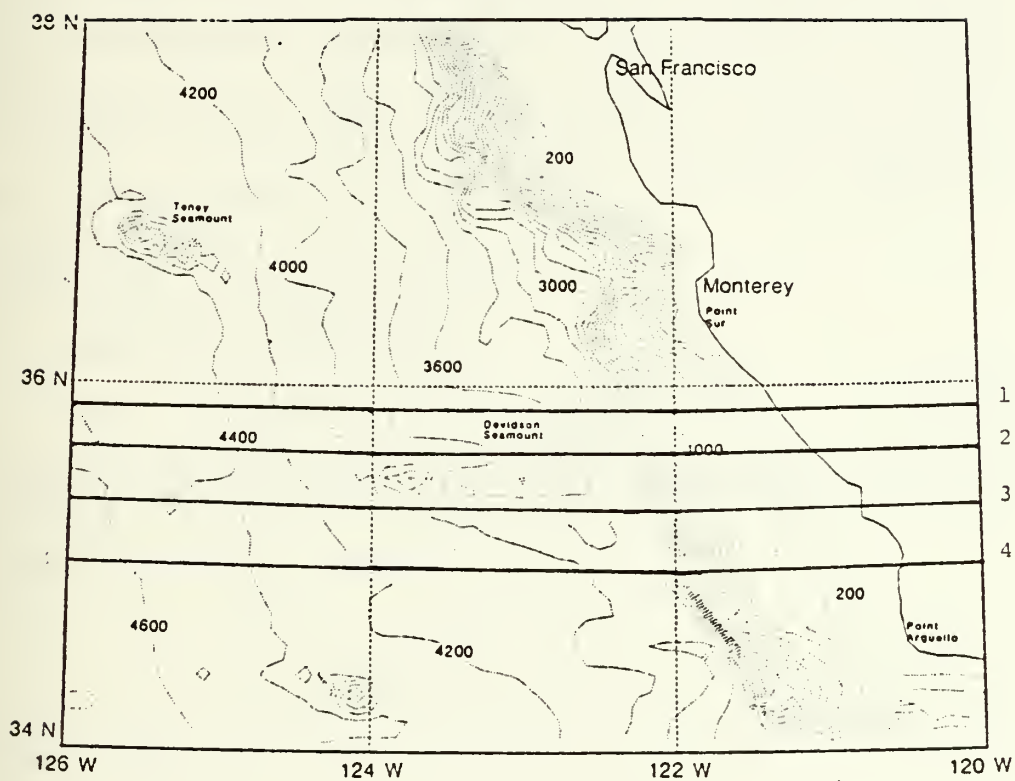


Figure 5. Trackline plots.



then applied to try and produce subsets that were as complete (continuous) as possible over the time domain. The total data matrix is thus partitioned into P subdomains

$$\mathbf{F}_t = \mathbf{F}_p ; p = 1, \dots, P , \quad (39)$$

where the subscript t denotes the total data set and subscript p denotes the partitions of the data set. Each  $\mathbf{F}_p$  is the data matrix for grid points falling within grid partition p, and contains all time points for which complete data were acquired in that subdomain.

### 3. Equation Development

The EOF decomposition discussed in B, is applied to each partition separately, such that for each partition, p, the scatter matrix is given by

$$\mathbf{S}_p = \mathbf{F}_p^T \mathbf{F}_p , \quad (40)$$

and from (36)

$$\mathbf{S}_p = \mathbf{E}_p \mathbf{L}_p \mathbf{E}_p^T , \quad (41)$$

where  $\mathbf{E}_p$  = Eigenvector matrix of the spatial partition p, and

$\mathbf{L}_p$  = Eigenvalue matrix for partition p.



The matrix of principal components for each partition is given by

$$\mathbf{A}_p = \mathbf{F}_p \mathbf{E}_p \quad . \quad (42)$$

Equations (38) require that

$$\mathbf{L}_p = \mathbf{A}_p^T \mathbf{A}_p \quad , \quad (43)$$

and so (41) can be written as

$$\mathbf{S}_p = \mathbf{E}_p \mathbf{A}_p^T \mathbf{A}_p \mathbf{E}_p^T \quad . \quad (44)$$

Relating this to a global scatter matrix,  $\mathbf{S}_G$

$$\mathbf{S}_G = \begin{bmatrix} \mathbf{S}_1 & & & \\ \mathbf{C}_{12} & \mathbf{S}_2 & & \\ \vdots & \vdots & \ddots & \\ \mathbf{C}_{1p} & \mathbf{C}_{2p} & & \mathbf{S}_p \end{bmatrix} \quad (\text{SYM}) \quad (45)$$

Where  $\mathbf{C}_{12}$  represents the matrix of covariances between grid points in domains 1 and 2, and so forth.

Now the joining process is developed. For any number of partitions (two are used in this development),

$$\mathbf{S}_1 = \mathbf{F}_1^T \mathbf{F}_1 = \mathbf{E}_1 \mathbf{A}_1^T \mathbf{A}_1 \mathbf{E}_1^T \quad (46)$$

and

$$\mathbf{S}_2 = \mathbf{F}_2^T \mathbf{F}_2 = \mathbf{E}_2 \mathbf{A}_2^T \mathbf{A}_2 \mathbf{E}_2^T \quad , \quad (47)$$



where the subscripts denote partition number.

For this combined set the scatter matrix is given by

$$\mathcal{S}_{12} = \begin{bmatrix} \mathcal{E}_1^T & \mathcal{E}_1 & \mathcal{E}_2^T & \mathcal{E}_1 \\ \mathcal{E}_1^T & \mathcal{E}_2 & \mathcal{E}_2^T & \mathcal{E}_2 \end{bmatrix} \quad (48)$$

Using equations (46) and (47),

$$\mathcal{S}_{12} = \begin{bmatrix} \mathcal{E}_1 & 0 \\ 0 & \mathcal{E}_2 \end{bmatrix} \begin{bmatrix} \mathcal{A}_1^T & \mathcal{A}_1 & \mathcal{A}_2^T & \mathcal{A}_1 \\ \mathcal{A}_1^T & \mathcal{A}_2 & \mathcal{A}_2^T & \mathcal{A}_2 \end{bmatrix} \begin{bmatrix} \mathcal{E}_1^T & 0 \\ 0 & \mathcal{E}_2^T \end{bmatrix} \quad (49)$$

The joining functions,  $\mathcal{J}$ , are defined as the eigenvectors of the central matrix given in (49). Finally using (41), (43) and (44), (49) becomes

$$\mathcal{S}_{12} = \begin{bmatrix} \mathcal{E}_1 & 0 \\ 0 & \mathcal{E}_2 \end{bmatrix} \mathcal{J}_{12} \mathcal{L}_{12} \mathcal{J}_{12}^T \begin{bmatrix} \mathcal{E}_1^T & 0 \\ 0 & \mathcal{E}_2^T \end{bmatrix} \quad (50)$$

The joining functions,  $\mathcal{J}$ , relate the separate subscenes to each other across an overall study domain. The interpretation of these functions should allow examination of the variations that occur throughout the domain and localized effects on the individual partitions of the domain.





#### D. INTERPRETATION

The coordinate system defined by the eigenvectors gives the domain for the principal components. In the present study, as well as most geophysical applications, the principal components can be thought of as temporal amplitudes and the eigenvectors as their spacial modulators (Preisendorfer, et al., 1981).

The  $i$ -th principal component is that linear combination of the data field which explains the  $i$ -th largest portion of the total field variance. Essentially the eigenvectors define a direction of variance, while the principal components give the amplitude of the variance in the direction of the associated eigenvector.

Once a data set has been reduced to a set of eigenvectors and associated amplitudes, the question of signal versus noise arises. A decision as to which components of the data field have significance, and which components of the data field have no physical meaning must be made. Some sort of a selection process must be defined and applied. Bases for these selection processes should have their roots in the physical processes being studied.



## V. RESULTS

### A. INTRODUCTION

The major focus of this thesis was to achieve a first step towards the analysis of the obtained data set. Much of the energy in producing these results was directed toward the processing of the data to a usable form for EOF analysis. Appendices A and B give a detailed discussion of the processing techniques utilized and an accounting of all adjustments applied to the data.

The results obtained in this thesis encompass three distinct areas. The first result emerged from the data processing and a discovery of the breakdown in the black ocean assumption. The remaining areas are interrelated as one deals with the data set prior to the EOF analysis, while the other attempts to relate this to a statistical meaning using EOF analysis methods.

### B. CORRECTIONS FOR NON-ZERO $L_w(670)$ IN COASTAL WATERS

Preliminary examination of this data set showed that, near the California coast, the assumption that  $L_w(670) = 0$  breaks down (Chapter III, Section C). This finding presented a need for an adjustment algorithm.



At pixels where the upwelled radiance at 670 nm,  $L_w(670)$ , is significantly greater than zero, calculated values of  $L_w(443)$  are often  $< 0.01$  ( $\text{mw}/(\text{cm}^2\text{-sr-m})$ ) (approximately 1 digital count in CZCS channel 1). This is unreasonable even in moderately turbid ocean waters. Smith and Wilson (1981) observed that in coastal waters off California, where pigments and/or sediment concentration are relatively high, it is not uncommon for the subsurface upwelling radiance  $L_w(670)$  to be non-zero. They developed an iterative procedure to account for this, which is similar to that developed independently and used in the present processing.

The procedure involves two major steps.

In the first step, which is invoked when  $L_w(443) < 0.01$ :

1. Set  $I_w(443) = 0.01$ , a minimal value for daylight backscatter and slightly less than one digital count in CZCS channel 1.
2. Decrease  $L_a(670)$  and increase  $L_w(670)$  to be consistent with the new value of  $L_w(443)$  (using equations (4) and (1)).
3. Recalculate  $L_w(520)$  and  $L_w(550)$ .
4. Recalculate  $C_1$ ,  $C_2$ ,  $K(490)$ ,  $K(520)$ .



The second step is based on the assumption that the  $C_2$  algorithm (equation (12), case III) is robust and insensitive to moderate errors in  $L_a(670)$ . This assumption was supported by sensitivity calculations which showed  $C_2$  values to vary by less than 30 percent for wide variations in  $\epsilon(\lambda, 670)$ . If  $C_1 - C_2 > 0.5$  and  $C_1 > 2$ , the correction is presumed unreasonable due to  $L_a(670)$  being too large (and correspondingly,  $L_w(670)$  being too small). Next, values of  $K(490)$  and  $K(520)$  are estimated, which are consistent with  $C_2$ :

1. Estimate a ratio  $L_w(443)/L_w(550)$  consistent with  $C_2$  by inverting the  $C_1$  algorithm (Equation(12) with case I coefficients) using the  $C_2$  values.
2. Increase  $L_w(670)$  and decrease  $L_a(670)$  to be consistent with the new values of  $L_w(443)$ .
3. Recalculate  $L_w(443)$ ,  $L_w(520)$ , and  $L_w(550)$
4. Recalculate  $C_1$ ,  $C_2$ ,  $K(490)$ ,  $K(520)$ .
5. Iterate this procedure until  $C_1$  and  $C_2$  agree.

Data acquired aboard the R/V Acania during the Optical Dynamics Experiment (ODEX) provide a tentative basis for assessing the validity and performance of the above adjustment algorithm. In Figure 6 values of  $1/K(490)$  calculated





from CZCS data, acquired on 16 October 1982, are compared with preliminary calculations of  $1/K(490)$  from selected ODEX stations. The transect shown is along 35N (partition 4). Stations 24 and 25 were occupied 1.5 hours before the Nimbus-7 CZCS observation, and 2 hours after it, respectively. Station 21 was occupied 9 hours, and stations 19 and 13 one and two days, respectively, prior to the satellite pass. The  $1/K(490)$  values at these stations were calculated from the graphical displays of raw irradiance profiles (at a wavelength of 490 nm) presented in the preliminary R/V ACANIA ODEX CRUISE REPORT (Mueller, Zaneveld and Smith 1982).

Panel 6a compares the CZCS and in situ  $1/K(490)$  values before the above adjustment was applied, and figure 6b compares them after the correction. Agreement in both cases is excellent in the transparent waters at stations 21, 24 and 25: no adjustment for  $L_w(670)$  was required in this region. In the inshore portion of the transect, however, agreement is obviously poor before the  $L_w(670)$  adjustment, and much improved afterwards. This result is preliminary, and subject to possible revision by cognizant ODEX investigators when their data have been brought to publishable form.



Nevertheless, the  $L_w(670)$  adjustment algorithm so overwhelmingly improves the CZCS estimates of  $K(490)$  that its use in this thesis project is fully justified and essential.

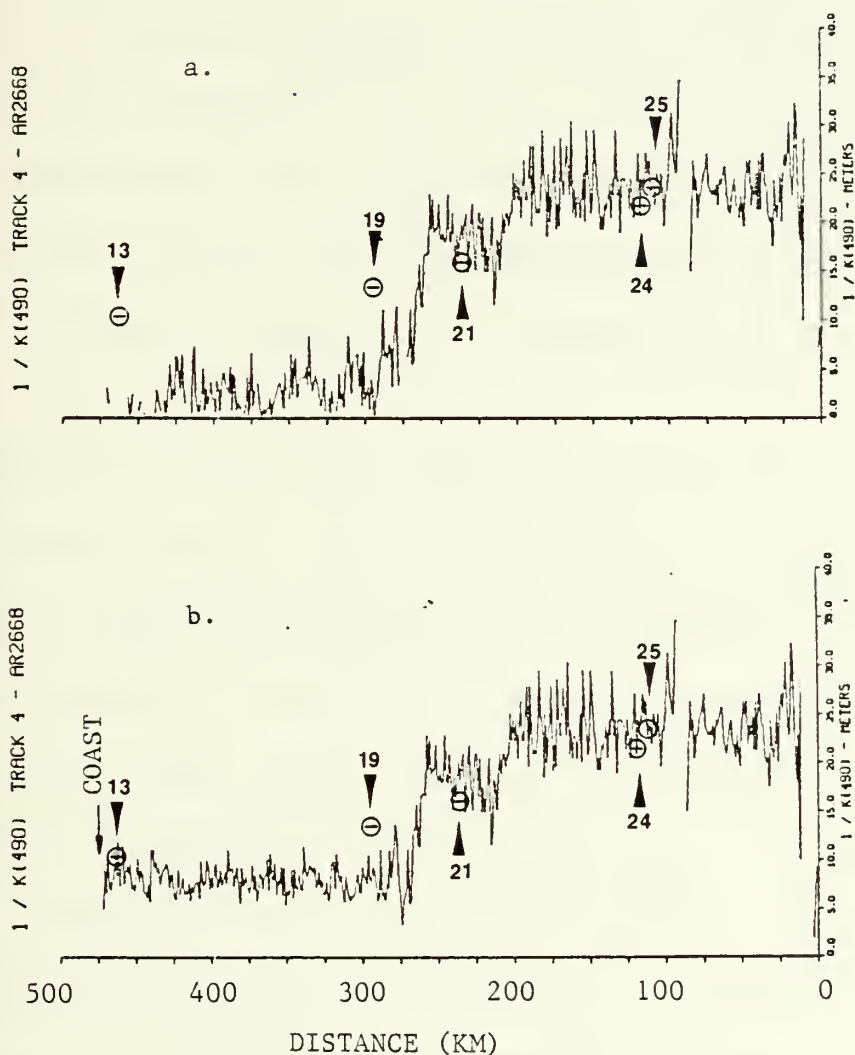


Figure 6. Comparison Plots For  $1/K(490)$  Between Track 4 and Selected ODEX Stations. Panels (a) and (b) respectively are Before and After Adjustments for Non-Zero Values of  $L_w(670)$ .



### C. DATA STRUCTURE

Figures 7 through 10 show the optical depth parameter,  $1/K(490) = Z_{90}(490)$  along each track for the available data scenes. (Gordon and McCluney (1975) showed that  $Z_{90}(\lambda)$  is the depth over which 90 percent of  $I_w(\lambda)$  is backscattered.) The plots are oriented so that the coast is on the right-hand side (positive  $x$ ), while time of the data scene goes from earliest to latest in the positive direction along the ordinate of each figure. The scale of  $1/K(490)$  is in meters.

Chapter II and III give background into the oceanography of the region and how that can be related to ocean optical parameters. The structures depicted in figures 7 through 10 will be discussed in terms of ocean eddy and front visualizations which result from these relationships. Relatively high values of  $1/K(490)$  indicate water with lower concentrations of chlorophyll and sediment. In general these concentrations may be expected to decrease with distance offshore. Abrupt changes in  $1/K(490)$  are usually associated with ocean frontal structure and eddies.



# 1. Partition 1 (Zonal Transect at 35 53N)

The only data available from 1979 (23 Nov) is from winter and shows relatively little structure, (Fig. 7). This image was obtained after the end of the upwelling season and the surface waters were homogeneous to at least 225 km offshore.

The 1980 data series shows more structure. Beginning on 17 May 80, an eddy of approximately 40 km diameter was centered approximately 180 km offshore. Sixteen days later the entire track shows several eddy-like features ranging in size from 4 km to 20 km. Three days later, on 6 June 80, the track has lost much of this structure, although 1/K(490) generally increases in the offshore direction. This trend persisted and strengthened slightly through June 1980. By 1 August 1980, a distinctive pattern had developed with nearly uniform turbid waters adjacent to the coast, and an abrupt (15 km) frontal transition to much more transparent waters at a distance approximately 95 km offshore. This pattern is suggestive of the zonal scale of bio-optical response to coastal upwelling over a single season.





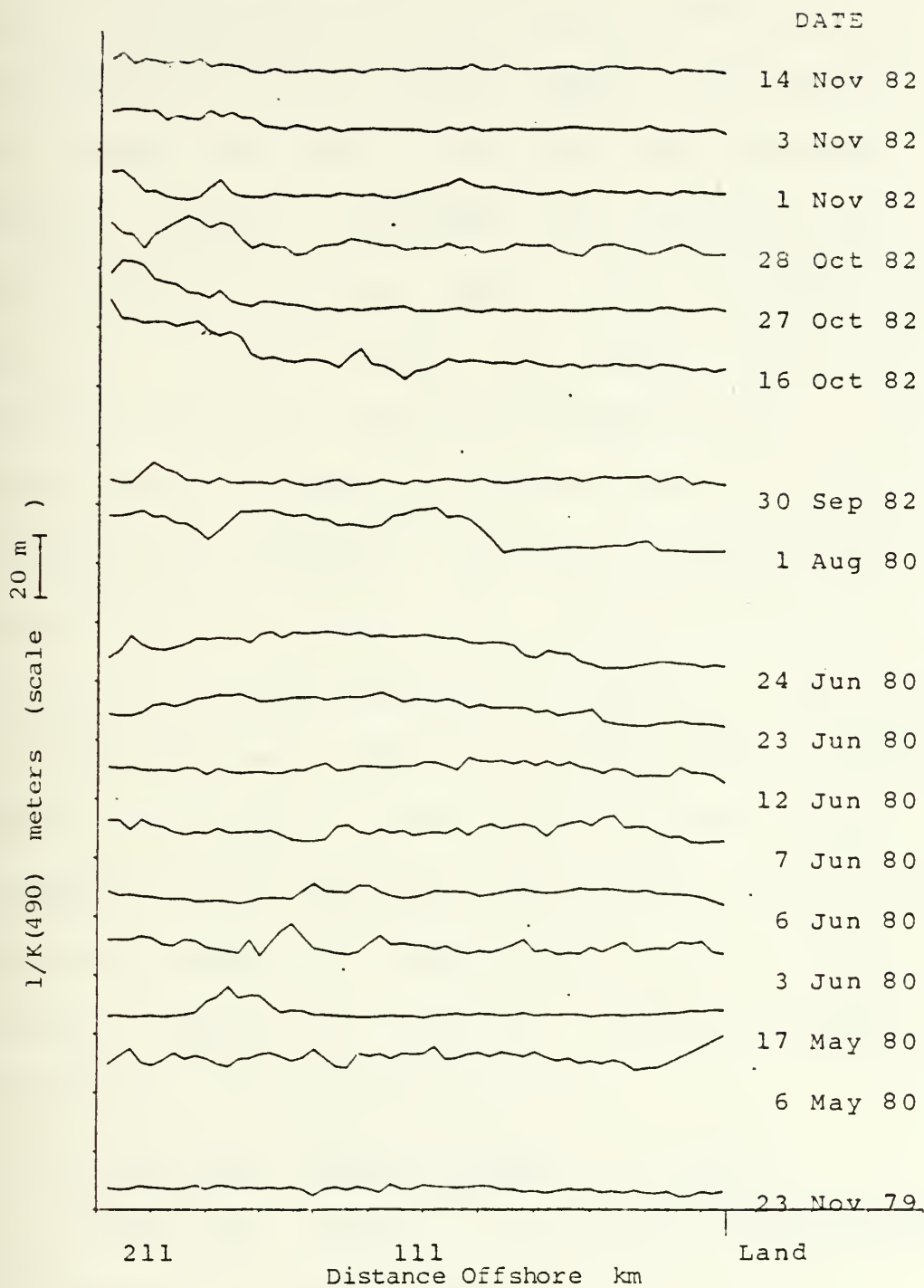


Figure 7. The Optical Depth Parameter,  $1/K(490)$ , Across Partition 1 (35 53N)



The 1982 scenes are all in the late fall to early winter. The transect from 30 September 1982 shows uniformly turbid water (5 to 10 m optical depth) with little structure, except for a weak, clear-water eddy signature 200 km offshore. Between 30 September and 16 October, more transparent (20 to 25 m optical depth) water intruded from offshore to within 190 km of the coast, with a frontal transition region of scale approximately 15 km. Over the ensuing month, this clear intrusion appeared to evolve into a field of less organized, eddy-like anomalies with scales ranging from 10 to 50 km. The 2-dimensional character of this pattern evolution should be studied in a future analysis of this data set. Such an analysis, which is beyond the scope of the present thesis, may indicate whether these changes are best interpreted as breakdown of a spatially continuous intrusion of offshore water, or as simply due to advection transporting entirely different water mass features into view at this location.

## 2. Partition 2 (Zonal Transect at 35 40N)

Track two (Fig. 8) is located along latitude 35 40' N (south of the first track).



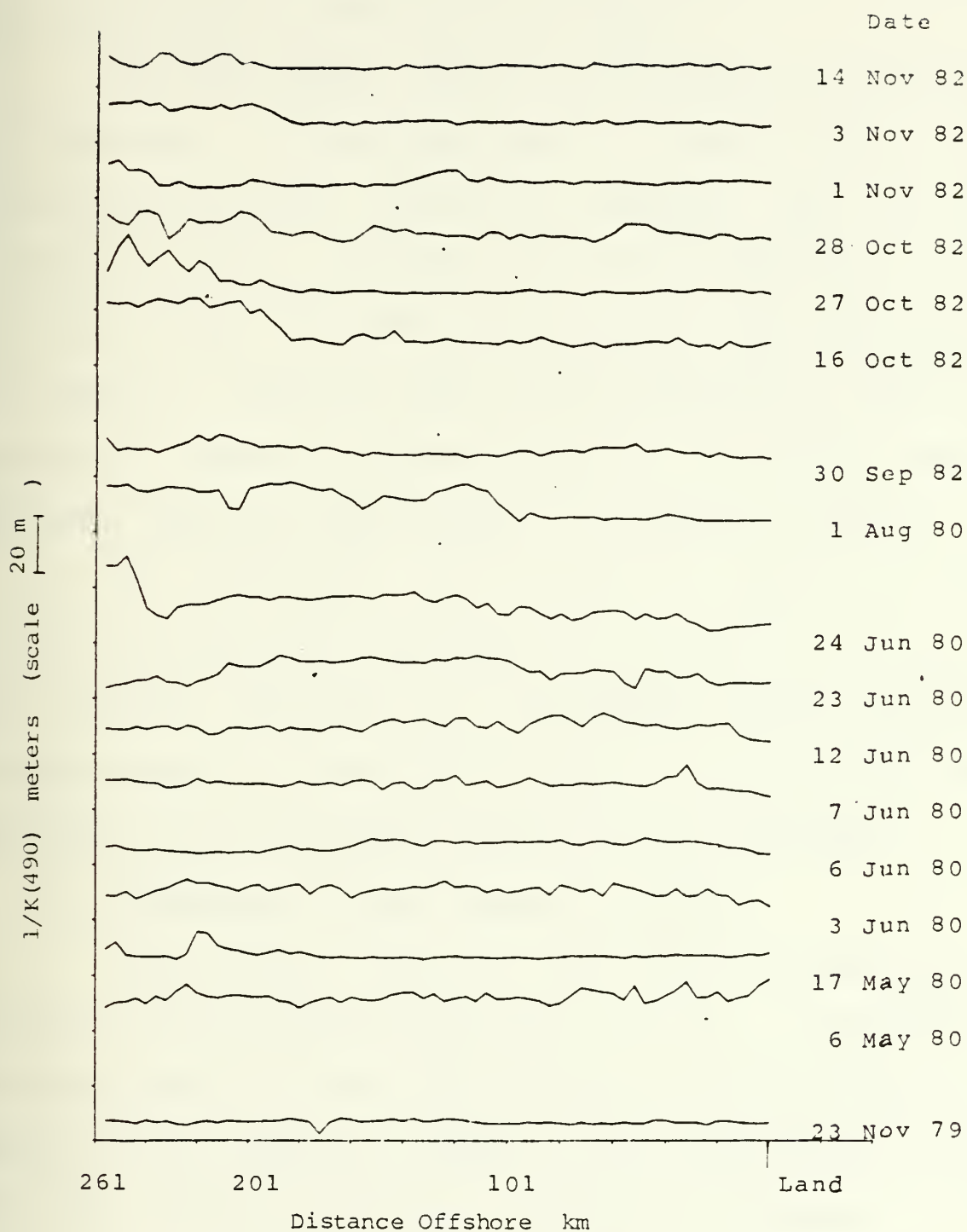


Figure 8. The Optical Depth Parameter,  $1/K(490)$ , Across Partition 2 (35 40N)



Again, the 1979 data set is limited to one day late in the year and is virtually featureless.

The 1980 series starts in late spring (6 May 1980) and progresses through late summer (1 August 1980). The same general features found in the northern track are also evident in track 2. However, the general appearance of the frontal boundary is broken by additional eddy structures. In addition, organized ocean frontal structures, which are apparently related to similar features in Partition 1 data, are here displaced approximately 15 km further offshore.

The 1982 scenes from partition 2 show the same front/eddy development presented in the data from the northern transect (partition 1). An offshore frontal boundary formed between 30 September 1982 and 16 October 1982, and evolved to a less organized pattern of eddy signatures.

### 3. Partition 3 (Zonal Transect at 35 22N)

Along track 3 (Fig. 9) the features already discussed for the previous partitions occurred. An additional feature here is a strong clear-water eddy signature approximately 220 km offshore, evident on the third of June 1980. The data suggest an eddy-like intrusion of transparent offshore water, approximately 40 km in diameter. (A feature of





similar diameter, but centered approximately 40 km closer inshore appears simultaneously in partition 4 (see below). This feature is short-lived, however, as no evidence of it remains three days later. This strange phenomenon is another candidate for future investigation in a 2-dimensional analysis.

In general, frontal boundaries along partition three are farther offshore in both the 1980 and 1982 series than apparently related frontal signatures in partitions one and two. Again, this may suggest the importance of bottom steering of the mean flow over diverging isobaths.

#### 4. Partition 4 (Zonal Transect at 35 00N)

The southernmost track at 35 00 N (Fig. 10) has similar patterns, including the offshore displacement of frontal boundaries. The location of the frontal boundary is at its farthest offshore position in this track.

The transient eddy feature of 3 June 1980, as discussed in partition 3, appears here to have a latitudinal extent large enough to span partitions 3 and 4 which are roughly 45 km apart. This is consistent with the zonal scale of the feature (approximately 40 km).



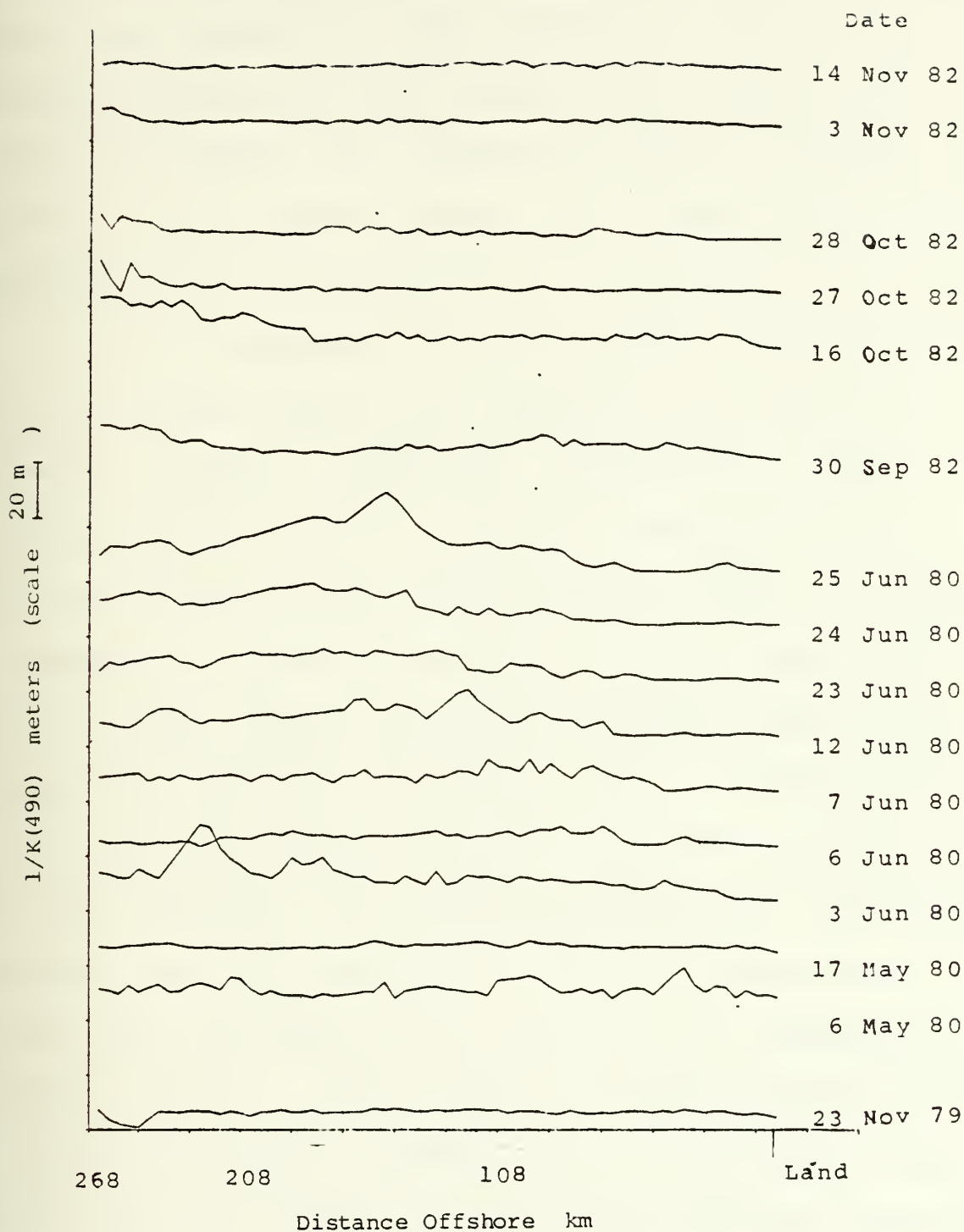


Figure 9. The Optical Depth Parameter,  $1/K(490)$ , Across Partition 3 (35 22N)



There also is a longitudinal displacement of approximately 40 km which suggests an eddy of slightly oblong shape that roughly parallels the coast. Questions of whether such features are coherent and continuous from one transect to another can be easily resolved in future 2-dimensional analyses.

It is reasonable to expect a band of surface water with low optical depth to lie adjacent to the coast, due to enhanced nearshore biological productivity during the upwelling season and due to northward transport of more turbid water masses by the Davidson Inshore Current in winter. In contrast, offshore waters tend to be far more transparent, at least during the seasons covered by this data set. It may be anticipated therefore, that an obvious optical front will persistently delineate the boundary between what may be classified as nearshore and offshore bio-optical regimes, and that intrusions of eddy-like surface water features from one regime to the other will be illuminated by optical contrast. Additionally, horizontal gradient structure in bio-optical processes will, within each regime, often (but not always) accompany the physical structure associated with ocean fronts and eddies and produce optical



depth structure of similar scales. The scales of previously observed structures in the California Current region may thus be expected to be present in the horizontal structure of optical depth. It is clear from the above discussion and the review of Chapter II that this is in fact the case. In the next section these structures will be discussed from a statistical viewpoint using EOF analysis.

#### D. EOF ANALYSIS

##### 1. Eigenvalues and Degrees of Freedom

Table II is a listing of the eigenvalues for the spatial covariance matrix calculated from the data in each partition analyzed. The cumulative percentages of the total variance are included. The first ten eigenvalues are listed here. In each case, they account for roughly 98 percent of the variance. The eigenvalues are presented graphically in figures 11 through 14, which include both the eigenvalues listed in Table II, and the additional eigenvalues that contain the noiser-appearing, higher spatial frequencies of variability (and together account for less than 2 percent of the total sample variance). We have assumed that 98 percent of the variance is an adequate cutoff for calculations.





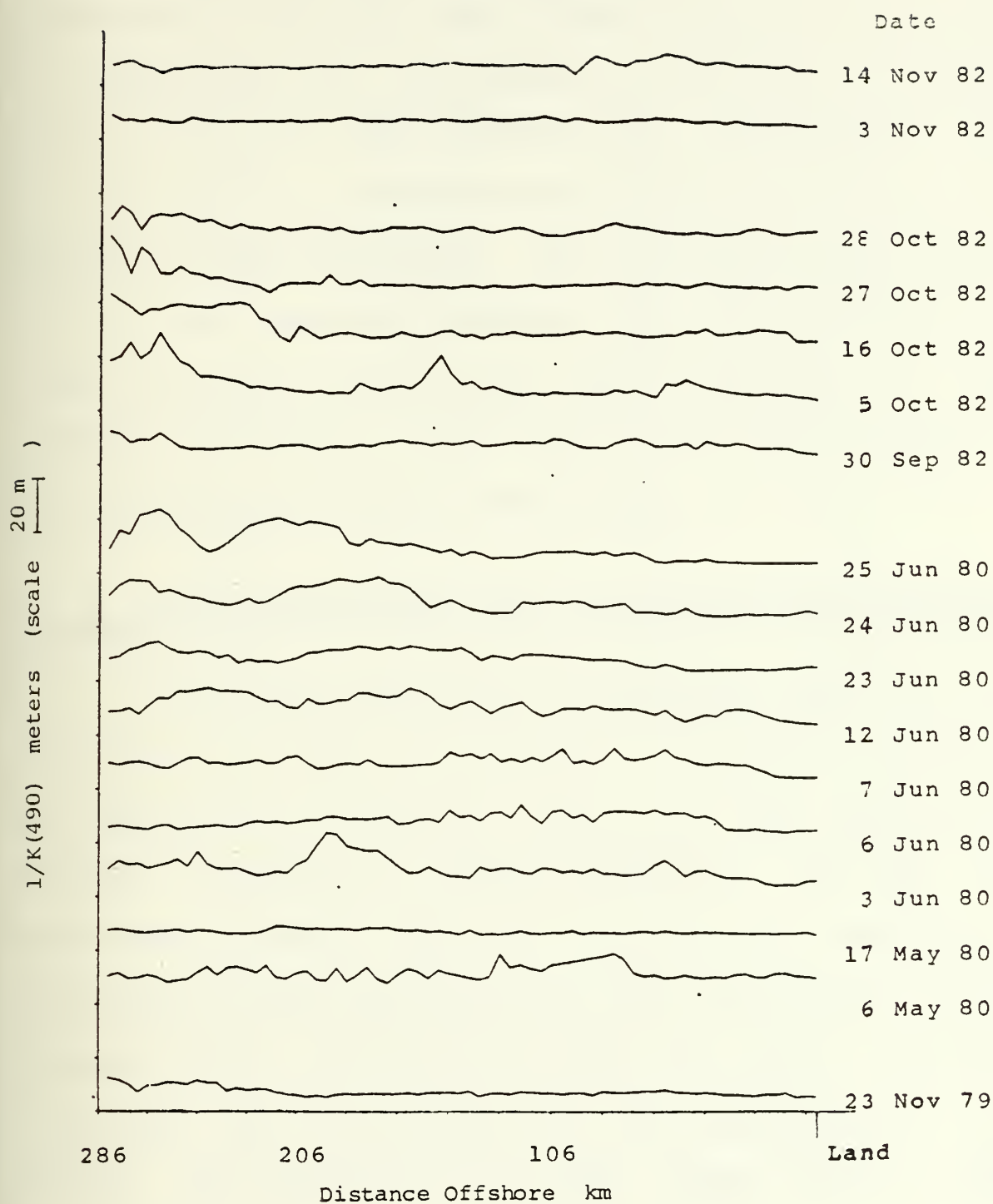


Figure 10. The Optical Depth Parameter,  $1/K(490)$ , Across Partition 4 (35 00N)



The major features seen in the eigenvalues are the differences in the first value between partitions 1, 2, and 3, and partition 4. The variance in partition 4 is more evenly distributed over the first three eigenvalues. All four partitions have reached roughly 90 percent of the variance by the sixth eigenvalue. The difference in the structure of the eigenvalues suggests that partition four is either affected by additional factors not found in the northern partitions, or that some factors which influence the northern partitions are absent here.

## 2. Data Reconstruction Using Eigenvectors and Principal Components

Before the eigenvectors and principal components are interpreted, how they are combined to reconstruct a particular observation is explained. Recall that each eigenvector defines a direction of spatial variability, and that its associated principal components represent the amplitude of variations in that direction at certain time points. In the present context a "direction" takes the form of  $1/K(490)$  variations that are coupled at all grid points of the domain, and "direction" in this sense may be best



TABLE II

Eigenvalue Data for Partitions 1 through 4

Order	Partition 1		Partition 2	
	Eigenvalue	Cumulative	Eigenvalue	Cumulative
	(m <sup>2</sup> ) -	Percentage	(m <sup>2</sup> )	Percentage
1	271.40	41.60	365.90	43.70
2	174.90	68.41	217.40	69.67
3	72.17	79.47	99.00	81.49
4	37.72	85.25	43.60	86.94
5	26.90	89.37	28.85	90.39
6	17.69	92.08	20.39	92.83
7	14.80	94.35	15.12	94.64
8	10.59	95.97	13.63	96.27
9	7.02	97.05	7.90	97.21
10	5.08	97.83	5.98	97.92

Order	Partition 3		Partition 4	
	Eigenvalue	Cumulative	Eigenvalue	Cumulative
	(m <sup>2</sup> ) +	Percentage	(m <sup>2</sup> )	Percentage
1	557.40	54.18	273.70	35.52
2	210.60	74.65	183.60	59.35
3	97.76	84.15	119.80	74.90
4	58.08	89.79	44.14	80.63
5	32.93	92.99	40.87	85.93
6	20.72	95.00	35.96	90.60
7	13.86	96.35	24.42	93.77
8	9.48	97.27	13.38	95.51
9	8.29	98.08	8.22	96.58
10	5.74	98.64	7.00	97.49

illustrated either as a curve (for one-dimensional transects) or contour plots (for two-dimensional domains). Given a temporal mean value for each grid point of a domain, the eigenvector multiplied by the principal component for a specific time yields a modifier to the mean signal.

For example, to view the contributions of the first five eigenvectors to the observed signal for 3 June 1980



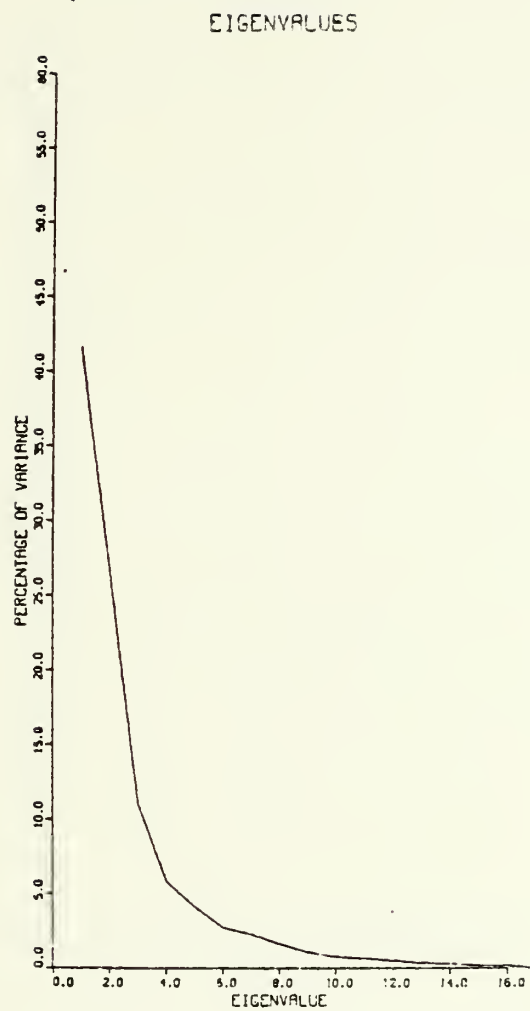


Figure 11. Eigenvalues for Partition One





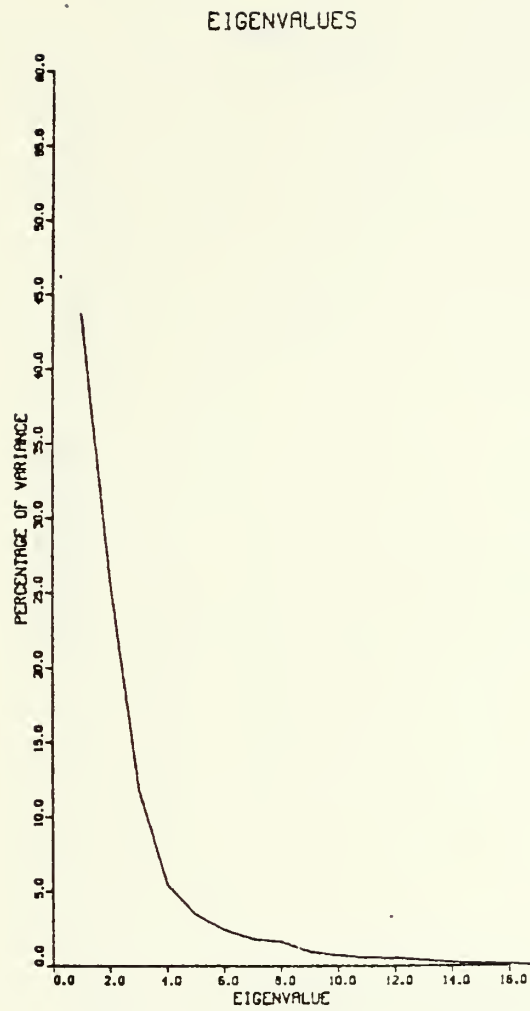


Figure 12. Eigenvalues for Partition Two



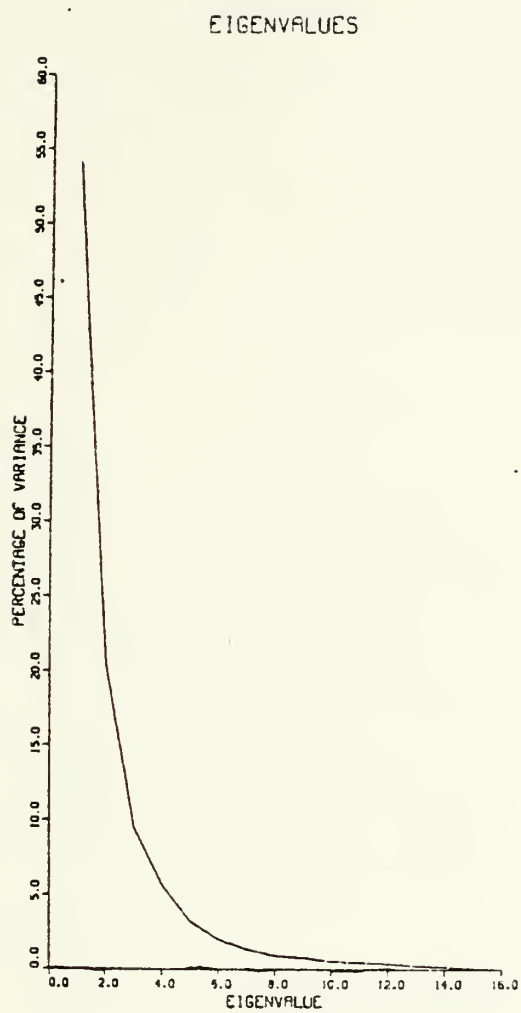


Figure 13. Eigenvalues for Partition Three



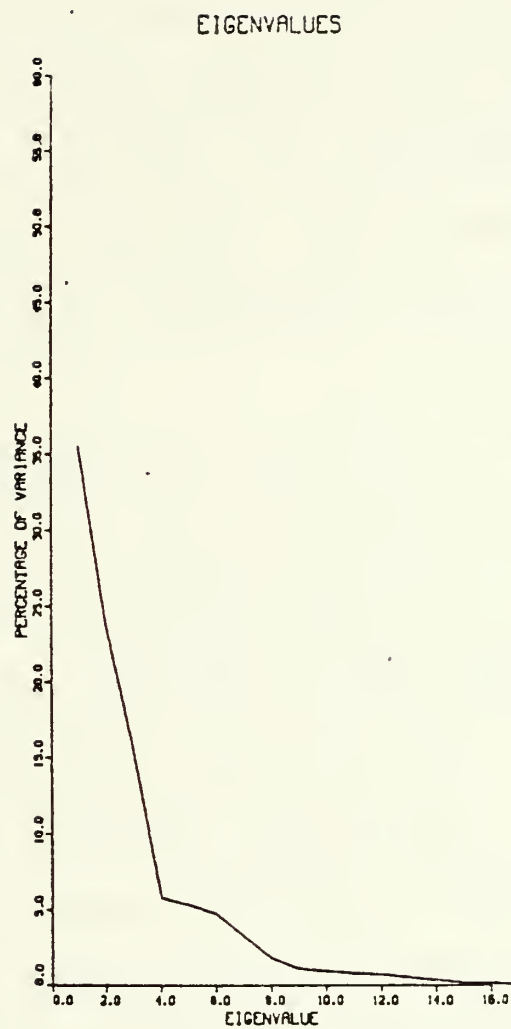


Figure 14. Eigenvalues for Partition Four



partition 3), we multiply each eigenvector by its principal component. The stepwise reconstruction of the observed vector from 3 June 1980 data (partition 3) from its principal components and eigenvectors is illustrated (Fig. 15).

It is clear that the first eigenvector primarily accounts for variations in zonal spatial structure with scales of order 200 km or greater, and with significant amplitudes only beyond 80 km offshore. This aspect of the information contained in eigenvectors will be discussed in later sections.

Figure 15b illustrates the previously accumulated signal with a solid curve, and now the dotted curve represents the addition of the second eigenvector as modified by the second principal component. This mode accounts for variations across the entire transect with scales of order 100 km. Figure 15c shows the contribution of the third eigenvector and principal component. This mode has almost no effect on the signal (as will be subsequently discussed, this happens to be an anomalous case). The contributions of the fourth and fifth eigenvectors and principal component are illustrated in Figs. 15d and 15e. Comparing Fig. 9 with the final dotted curve shows that the data





from partition three of VIS113 on 25 Jun 1980 and the reconstructed curve agree with the use of five eigenvalues, and that a fair representation can be reconstructed using only the first two eigenvectors.

### 3. Mean Structure

The mean optical depth ( $1/k(490) = Z_{90}$ ) transect profiles for partitions 1 through 4 are illustrated in Figs. 16 through 19 and are repeated for ease of comparison in Figs. 24 through 27. The mean vector in each track represents the tendency of the signal, while the eigenvectors scaled by the principal components give the perturbations of the mean. In all four partitions, the mean value of optical depth tends to increase with distance offshore. This tendency is expected since the coastal waters should contain higher concentrations of sediment and phytoplankton, especially during the upwelling season (Traganza, et al., 1979). There is a general lack of significant eddy-like structure in the mean vectors from all four transects (although very low amplitude perturbations of scale five-to-ten km are apparent in the means).



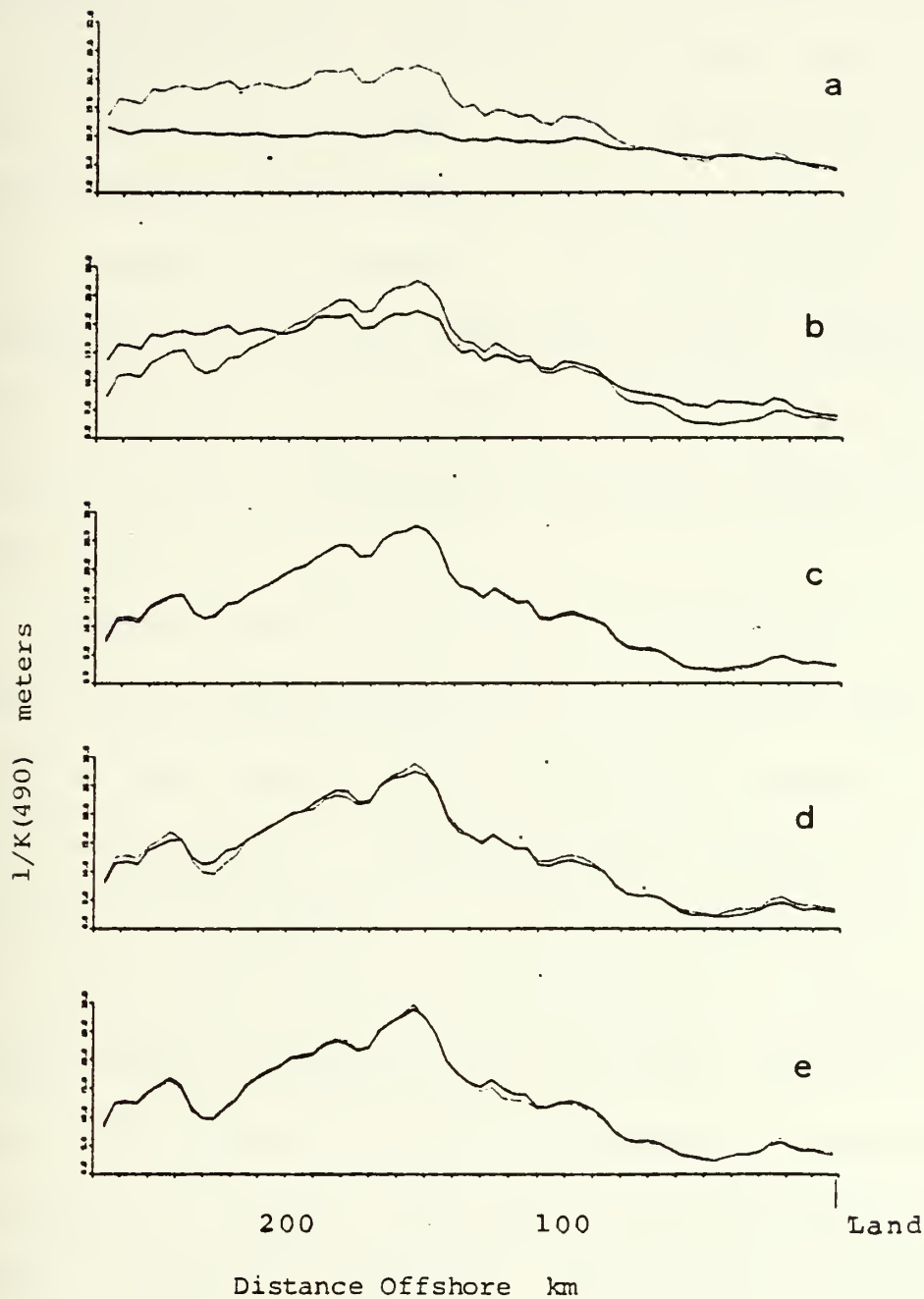


Figure 15. Reconstruction of Optical Depth Transect of 3 June 1980 (Partition 3) from Mean (Solid Curve, Panel a) and Successive Contributions of Eigenvectors 1 to 5 (Dashed Curves) in Panel a to e Respectively.



#### 4. Structural Content of Eigenvectors and Principal Components

The eigenvector discussion involves many intercomparisons of the partitions. Each partition's first ten eigenvectors are plotted, (Figs. 16 through 19 and 24 through 27). To organize the discussion, the first eigenvector will be discussed for all four partitions before proceeding to discuss the second, and so forth. The associated principal components are also illustrated, (Figs. 20 through 23 and 28 through 31).

The structure in the first eigenvector of each of the partitions is characterized by a band of low variability adjacent to the coast, and the structure offshore of that band is dominated by a scale extending from there to the offshore end of the domain. The "node" marking the onshore limit of significant variation in this mode is progressively farther offshore, proceeding from the south through the partitions. The "node" of partition 1 begins at approximately 45 km offshore, and by partition 4, the "node" is 100 km offshore. There is a tendency for variance to decrease in the amplitude of the first eigenvector as the offshore boundary is approached. This may be an artifact of the



outer boundary and should be investigated further over a larger domain to better estimate the dominant scale. Partition 4, which has the largest spatial extent, shows more and larger offshore structure to beyond 180 km.

The associated principal components, which modify the eigenvectors before they are applied to the mean, show the time variations. Across the four tracks, the first eigenvectors/principal components vary in phase with each other. In all four transects there is a large difference between the first principal component of the only 1979 image (early winter) and those from 1980 (early spring). This marked difference is certainly a manifestation of seasonal variations in the California Current system (Pavlova, 1966; Hickey; 1979). Most of the first principal components variability in all cases is observed in the 1980 series (upwelling season), and the record contains relatively little variability in the 1982 series (Davidson Current season). Coherency of the variations differs from partition-to-partition with no apparent pattern. The first eigenvector and principal component appear to have their foundations in the offshore seasonal variation and large scale eddy structure that occurs during the upwelling season. In the first mode,





the inshore zone influenced by upwelling tends to remain turbid throughout the year, whereas the dominant variations in optical depth occur offshore of the upwelling zone.

The shapes of second eigenvectors from the four partitions are similar, but vary in an oscillatory fashion from the northern partition to the southern partition. The first partition (northern) shows negative values beyond approximately 180 km offshore, and then small amplitude positive values from there to the coast. Partition two and three depict a mirror image pattern to that of the first partition. Partition four shows much the same pattern as partition one. The phase relation in the principal components shows no pattern between partitions one and two, but the series for partitions three and four both suggest phase reversal from the first partition. This negative-to-positive-back-to-negative pattern of behavior weakly suggests a wave-like meridional oscillatory structure, with an offshore peak (180 km offshore) in the vicinity of partitions two and three. Resolution of this meridional characteristic feature will require a 2-dimensional analysis. The distance of separation of the partitions suggests a wavelength of the order of 120 km. Again, the majority of the variability occurs



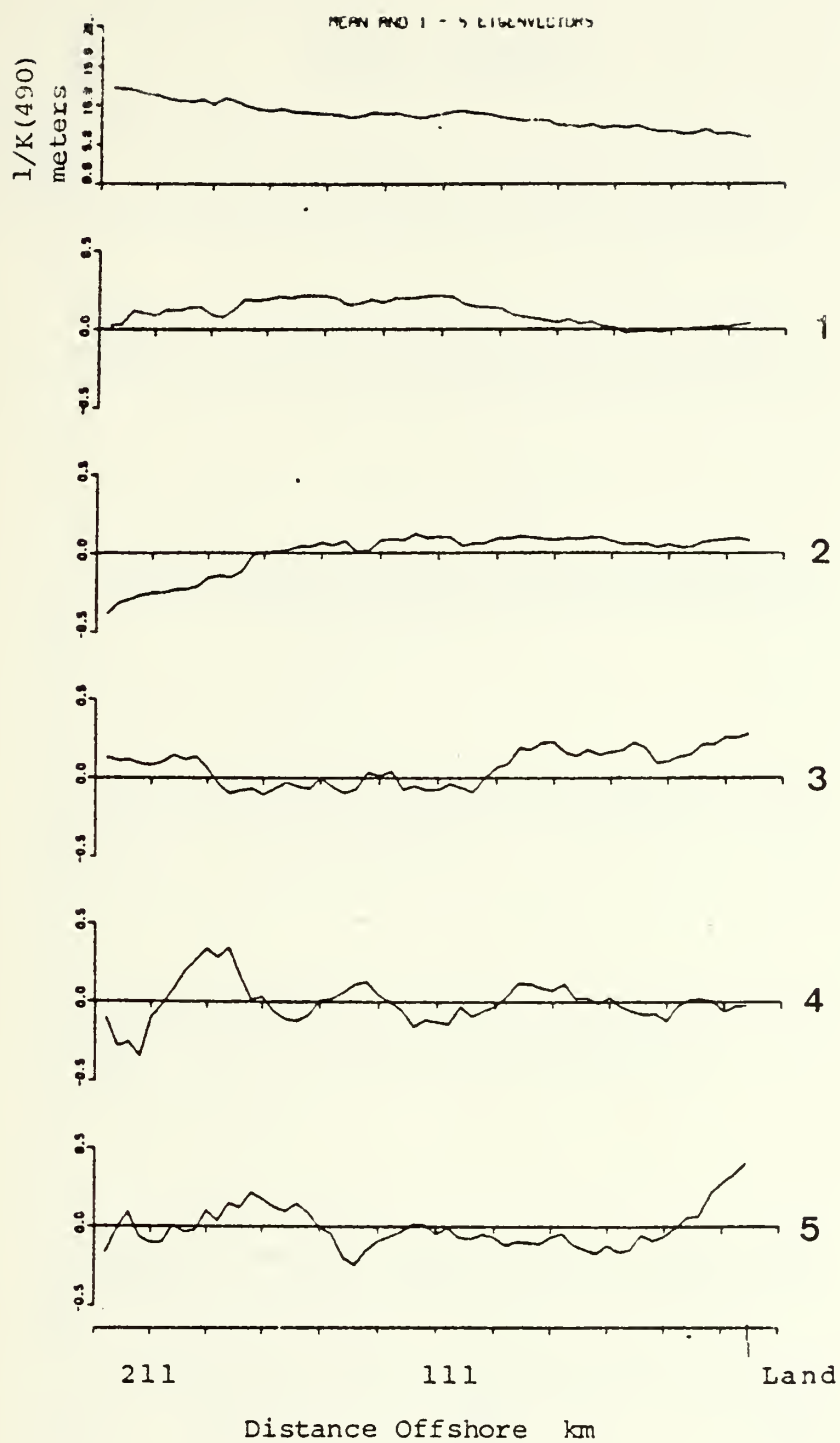


Figure 16. Mean and Eigenvectors 1 to 5 for Partition One.



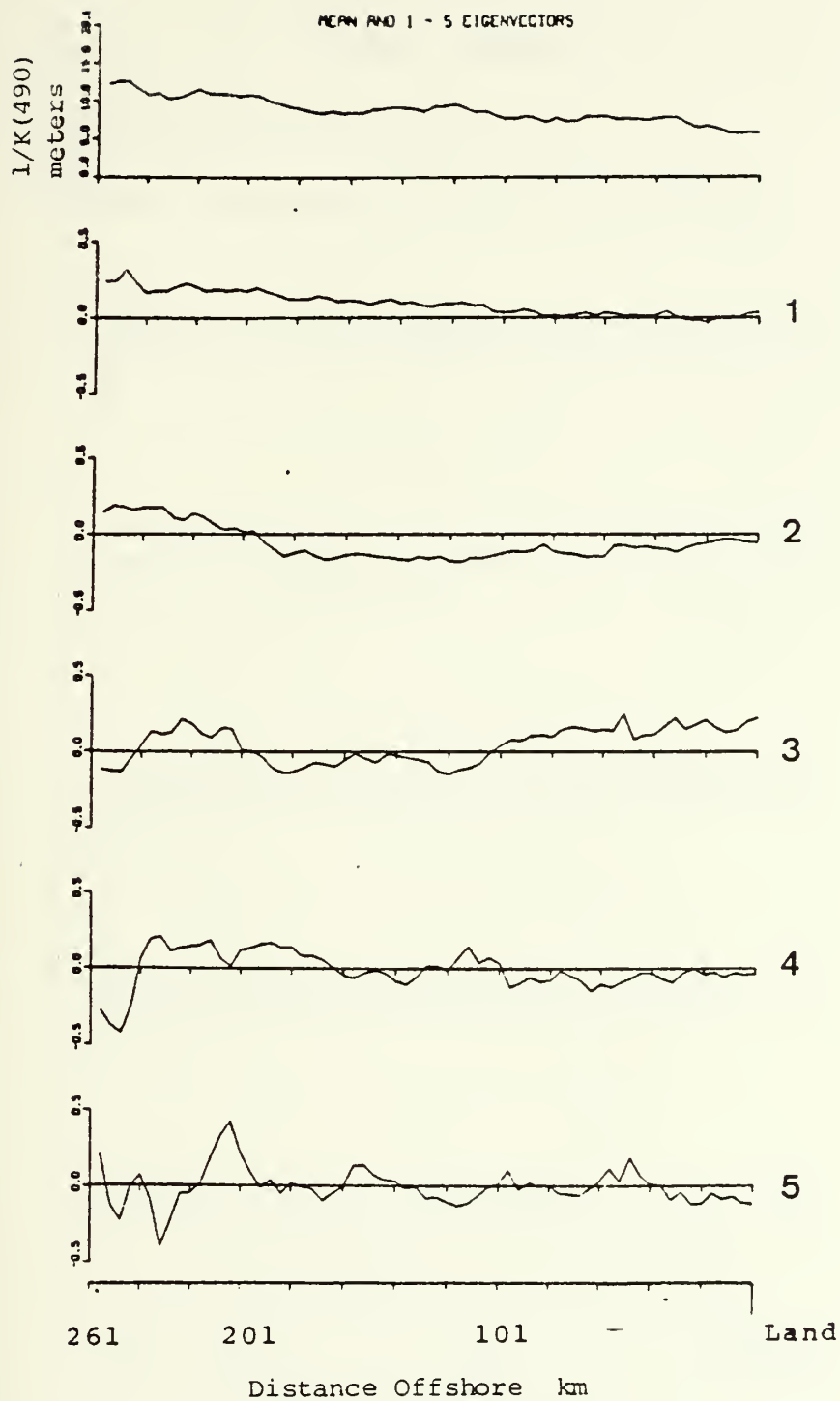


Figure 17. Mean and Eigenvectors 1 to 5 for Partition Two.



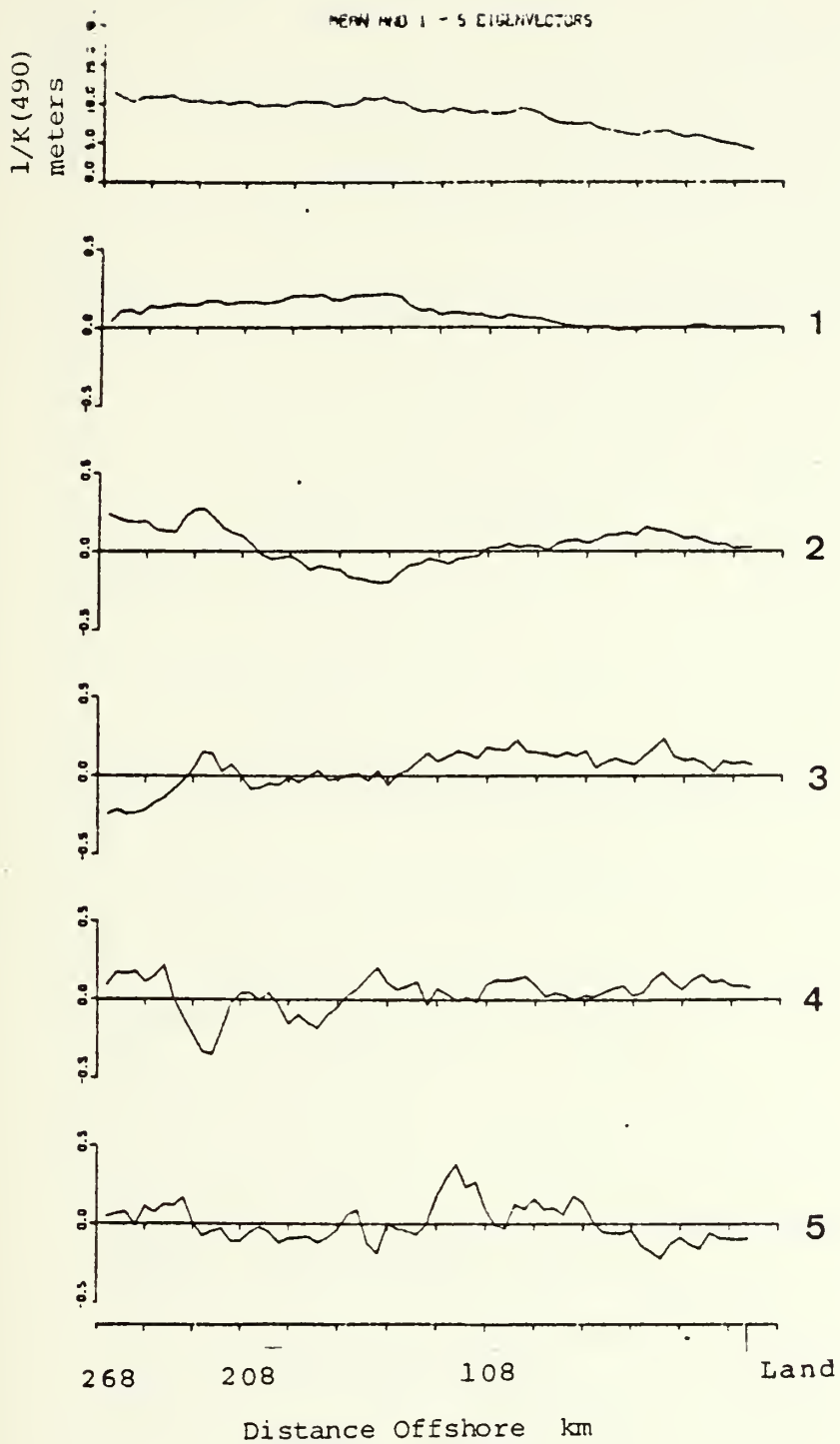


Figure 18. Mean and Eigenvectors 1 to 5 for Partition Three.





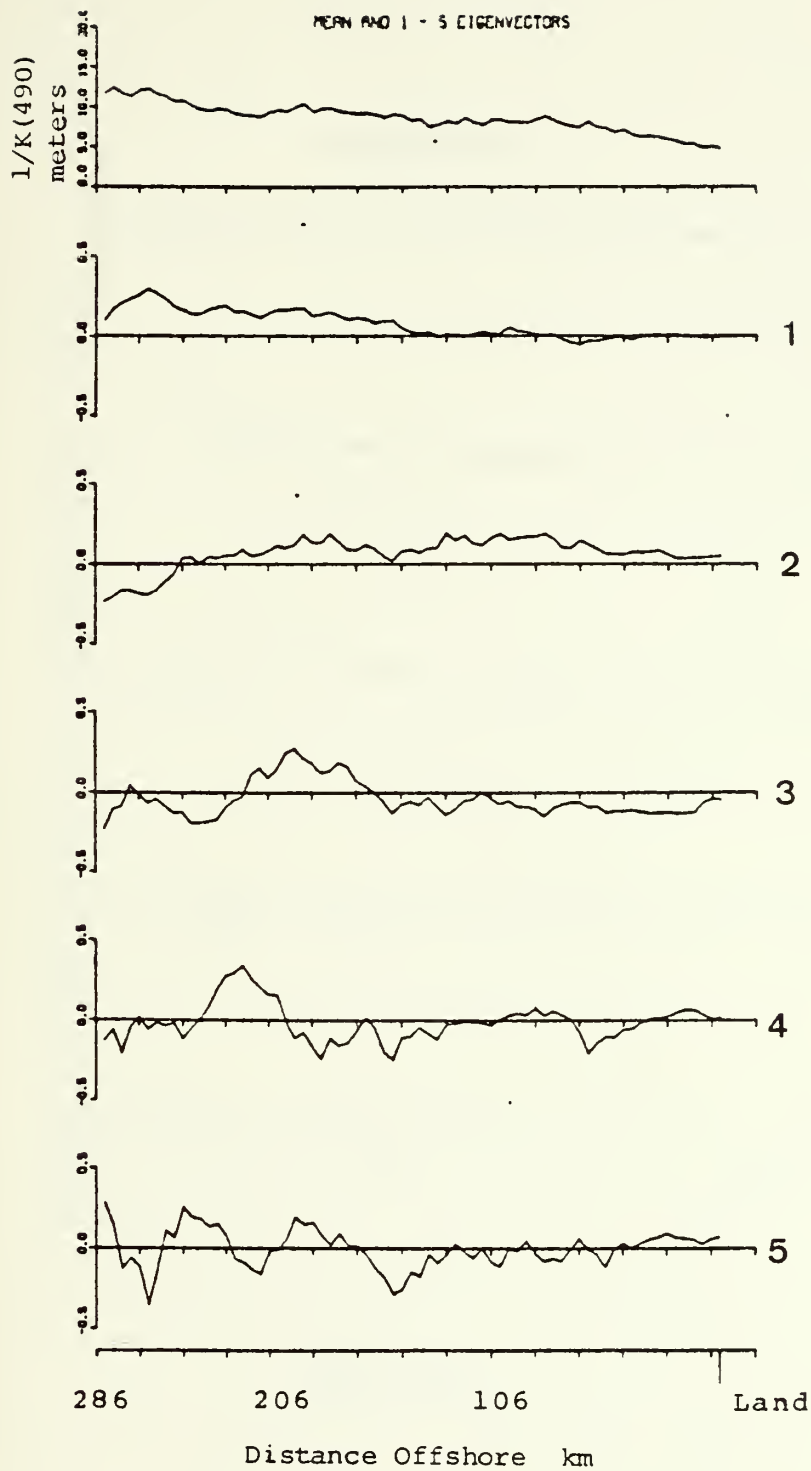


Figure 19. Mean and Eigenvectors 1 to 5 for Partition Four.



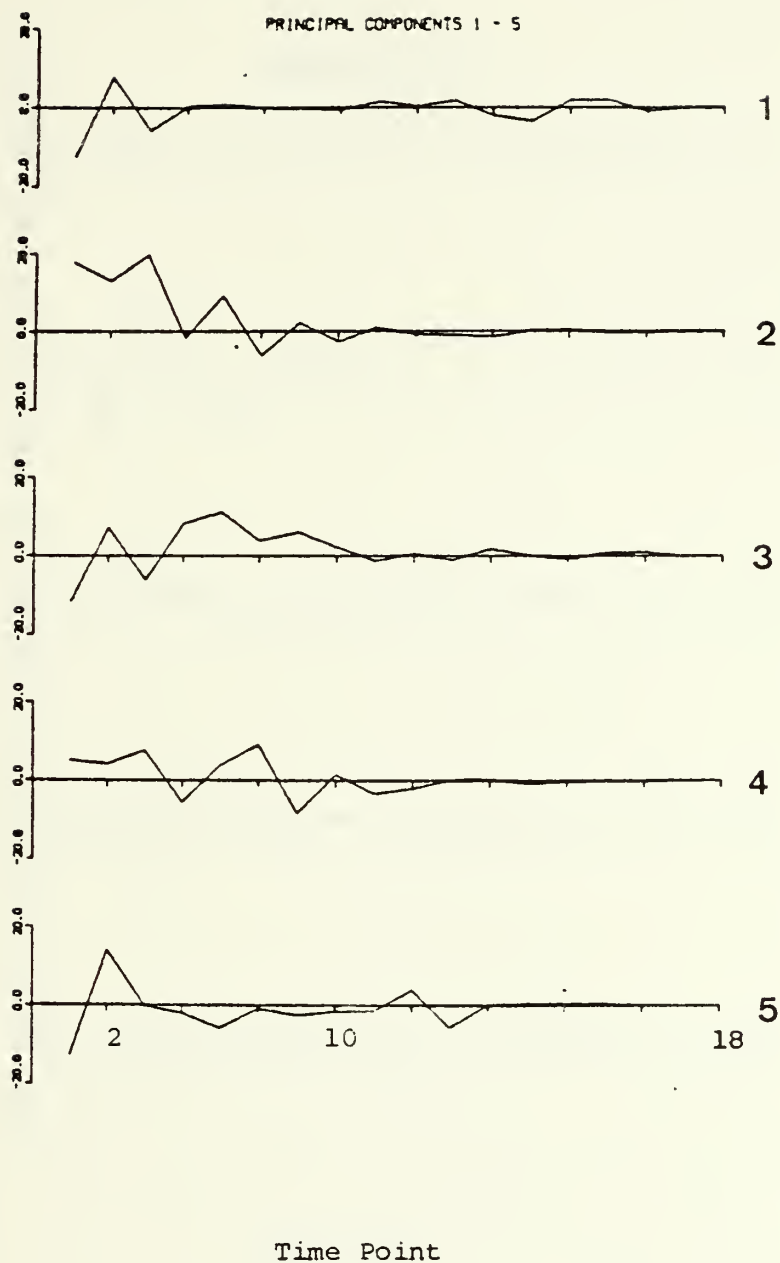


Figure 20. Principal Components 1 to 5 for Partition One.



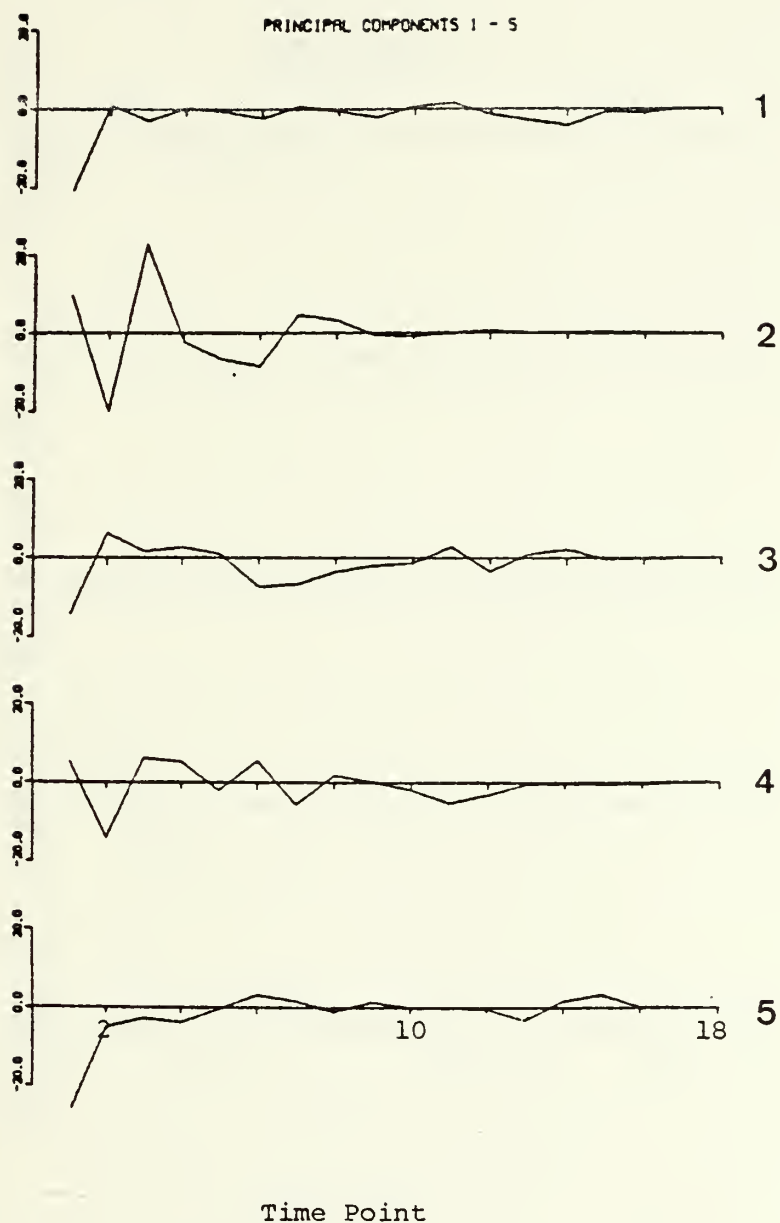


Figure 21. Principal Components 1 to 5 for Partition Two.



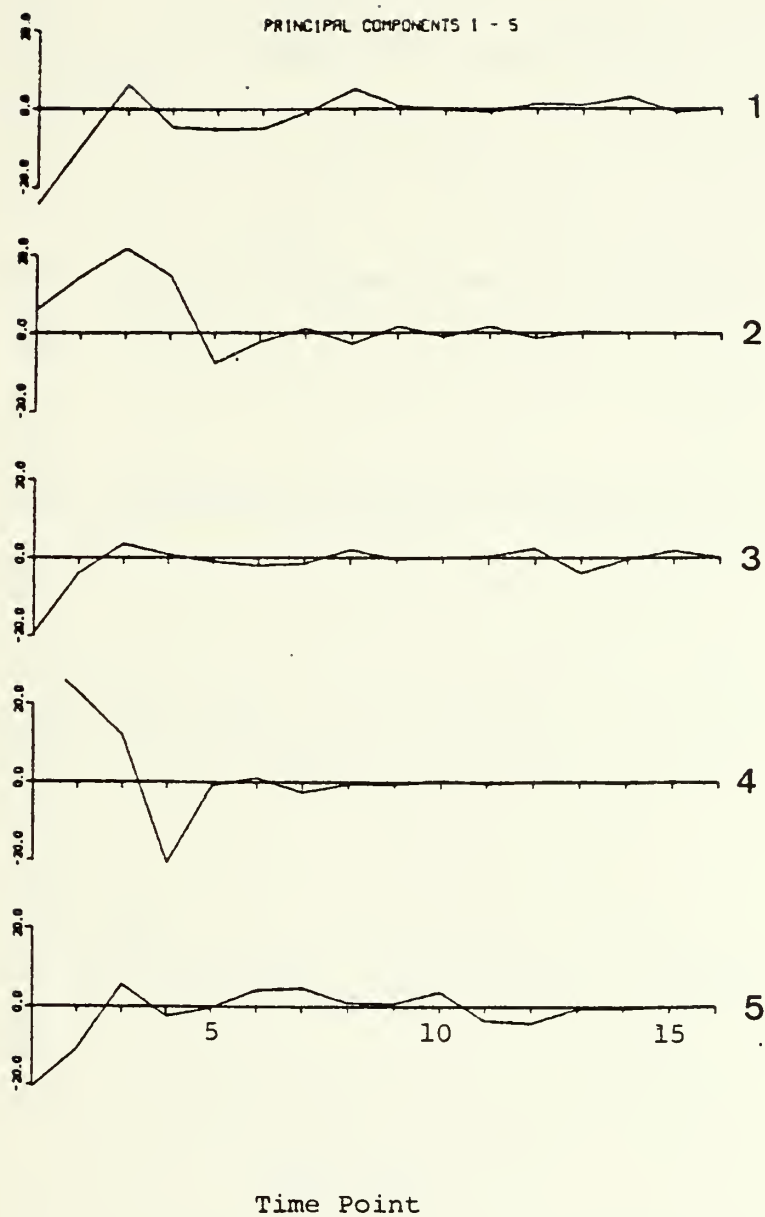


Figure 22. Principal Components 1 to 5 for Partition Three.





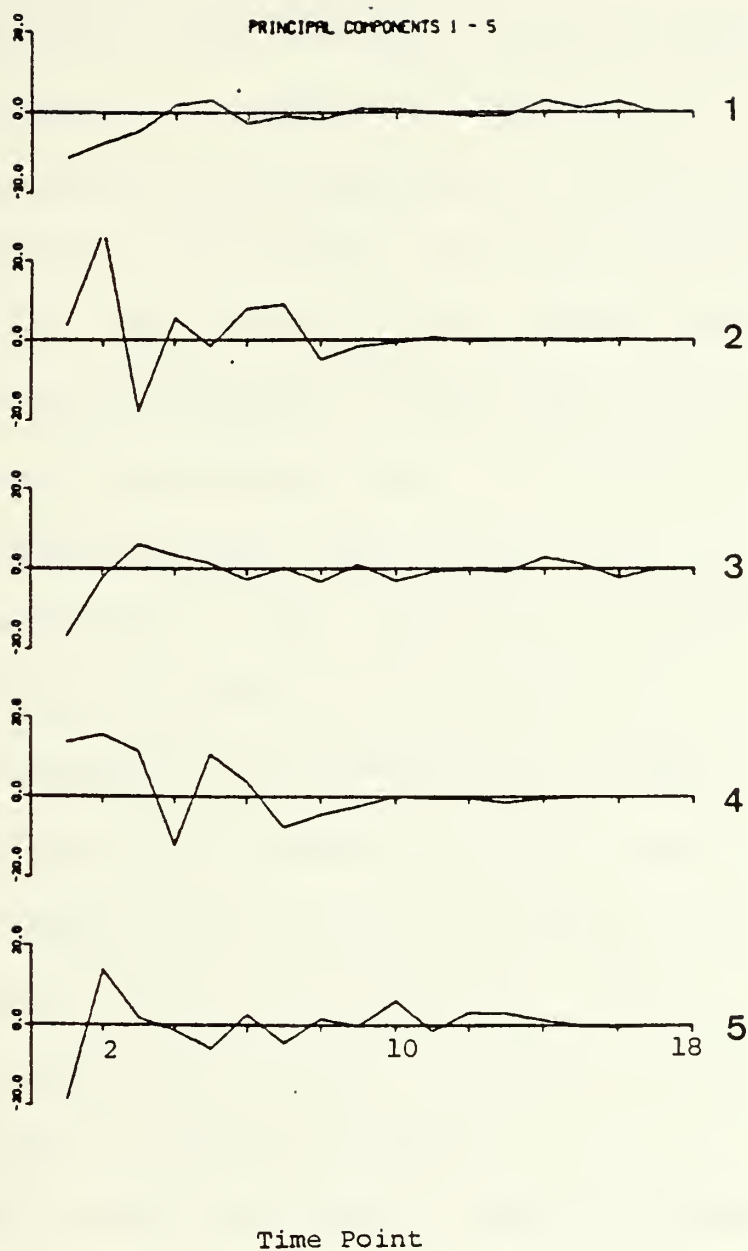


Figure 23. Principal Components 1 to 5 for Partition Four.



during the 1980 series. More nearshore structures are apparent in this eigenvector, as is an increase in nearshore variability, as compared to the first eigenvector.

The third eigenvector has a similar behavior for the first two partitions. The perturbations are of roughly the same spatial scale (45 km) and appear to be in phase. However, the third and fourth partitions show an opposite behavior in the far offshore region (beyond 180 km). Numerous smaller scale features (of the order of 10 km or less) are apparent in this eigenvector. In general, higher spatial frequencies become increasingly important in higher order eigenvectors. The principal components show an increase in the variability of the 1982 series with the wide range of variability still present in the 1980 series. This eigenvector shows the largest nearshore amplitudes of all the eigenvectors, which suggests it may be closely linked to the nearshore structure of upwelling. There is little suggestion of a temporal relation evident in the third principal components of the four tracks.

The fourth eigenvector shows an increase in frequency (decrease in wavelength) of the represented variability scales. Features range in size from 18 - 45 km, with



numerous smaller scale perturbations. The average wavelength and range of variability is approximately the same for all four partitions. The principal components for partitions one, three and four qualitatively suggest coherency. However, eigenvector behavior is opposite in partition three and similar in partition four when compared to partition one. A prominent feature approximately 180 km offshore in the fourth eigenvector of partition one, seems to be shifted outward to 210 km offshore in partition four. This time/space relationship between the structures of partition one and four again suggests a meridional oscillation worthy of future investigation through a 2-dimensional analysis.

The fifth eigenvector shows features of scale that range from 5-42 km. The much smaller features (less than 5 km) are not dealt with as they are essentially part of the background noise expected in any natural system. Little can be said about the correspondence of the four partitions with just a visual inspection. However, nearshore structure appears in the eigenvectors with more variability than in previous eigenvectors of the 1982 series. The 1980 series still demonstrates the largest overall variability, and the



large interannual differences between the one scene in 1979 and the 1980 scenes is still evident. The principle components of partition one and four show excellent agreement in amplitude and phase for the first five time points, but as structural variability decreases with time, so does correspondence. The quantitative correspondence of these variations is beyond the scope of this thesis, but it should be investigated in future analyses of this data set.

The sixth through the tenth eigenvectors are characterized by variation of such high frequency that little can be said of the relationships between the partitions. Scales of structural features in these eigenvectors range from 1 to 35 km, with no suggestion of a temporal relation between partitions. The principal components show that the 1980 data again dominates the variance, but at these higher frequencies the increased contribution of the 1982 data to the total variance is very apparent. Because of this disorganized structure, detailed interpretation is not attempted for eigenvectors of order greater than 5.





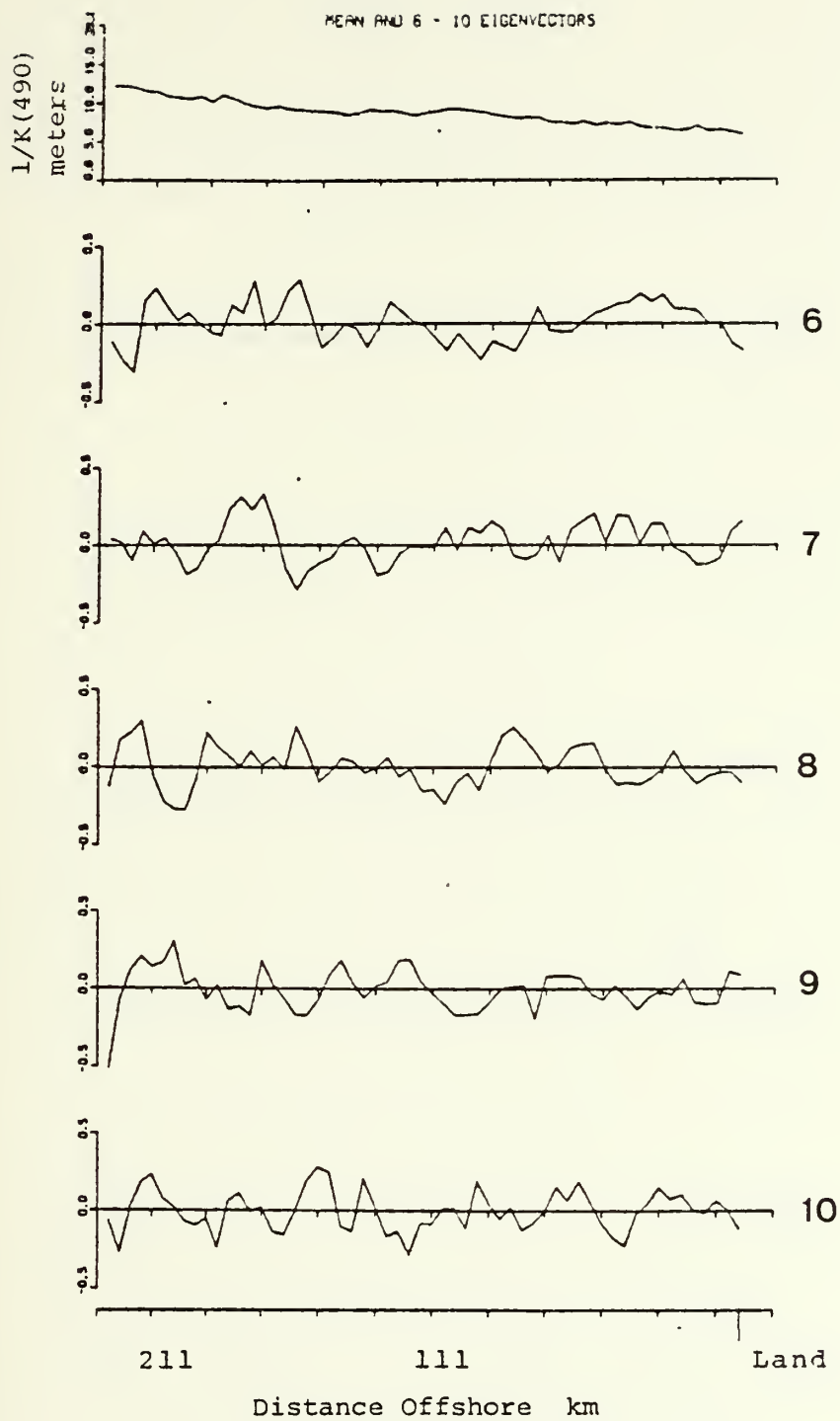


Figure 24. Mean and Eigenvectors 6 to 10 for Partition One.



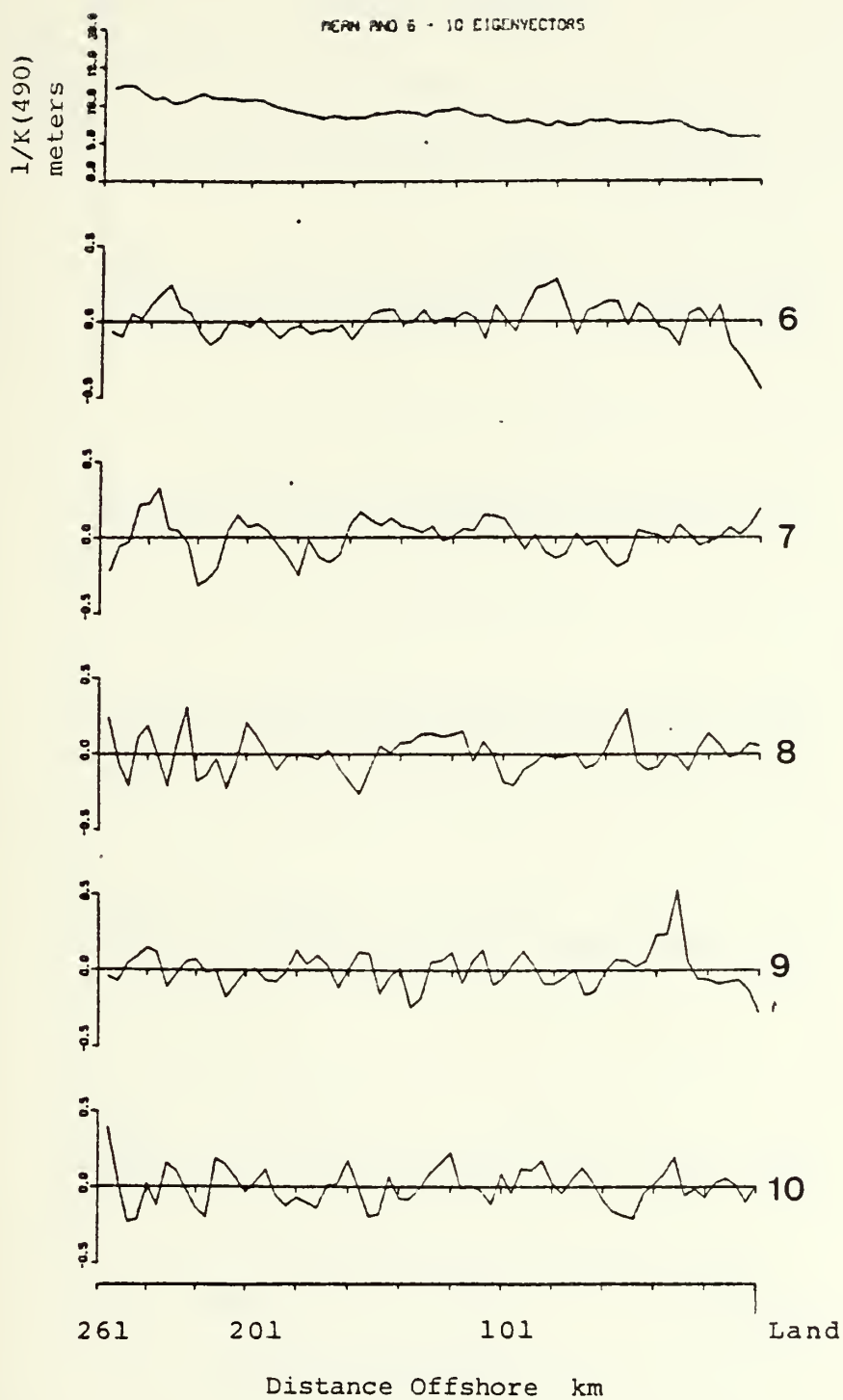


Figure 25. Mean and Eigenvectors 6 to 10 for Partition Two.



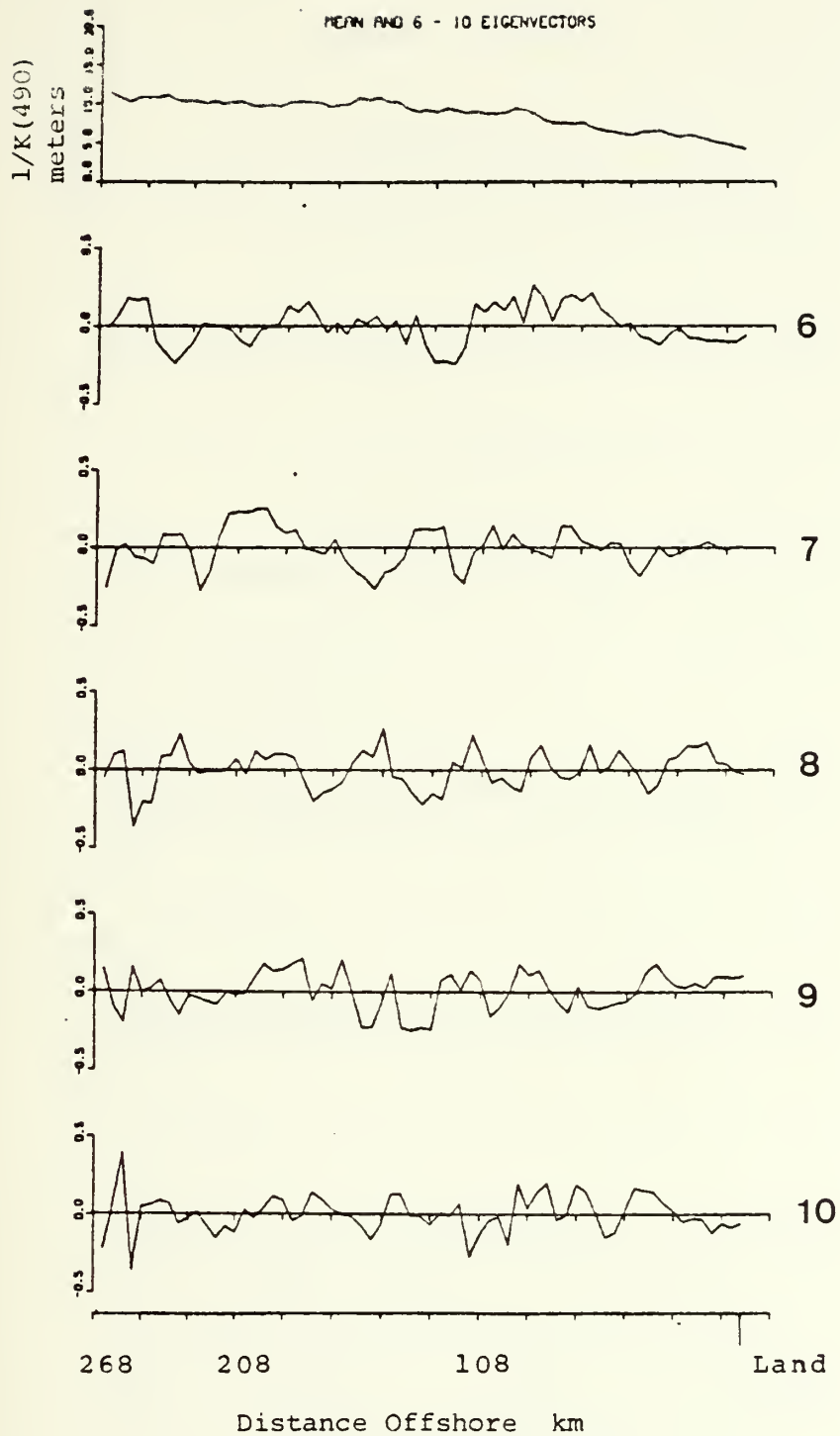


Figure 26. Mean and Eigenvectors 6 to 10 for Partition Three.



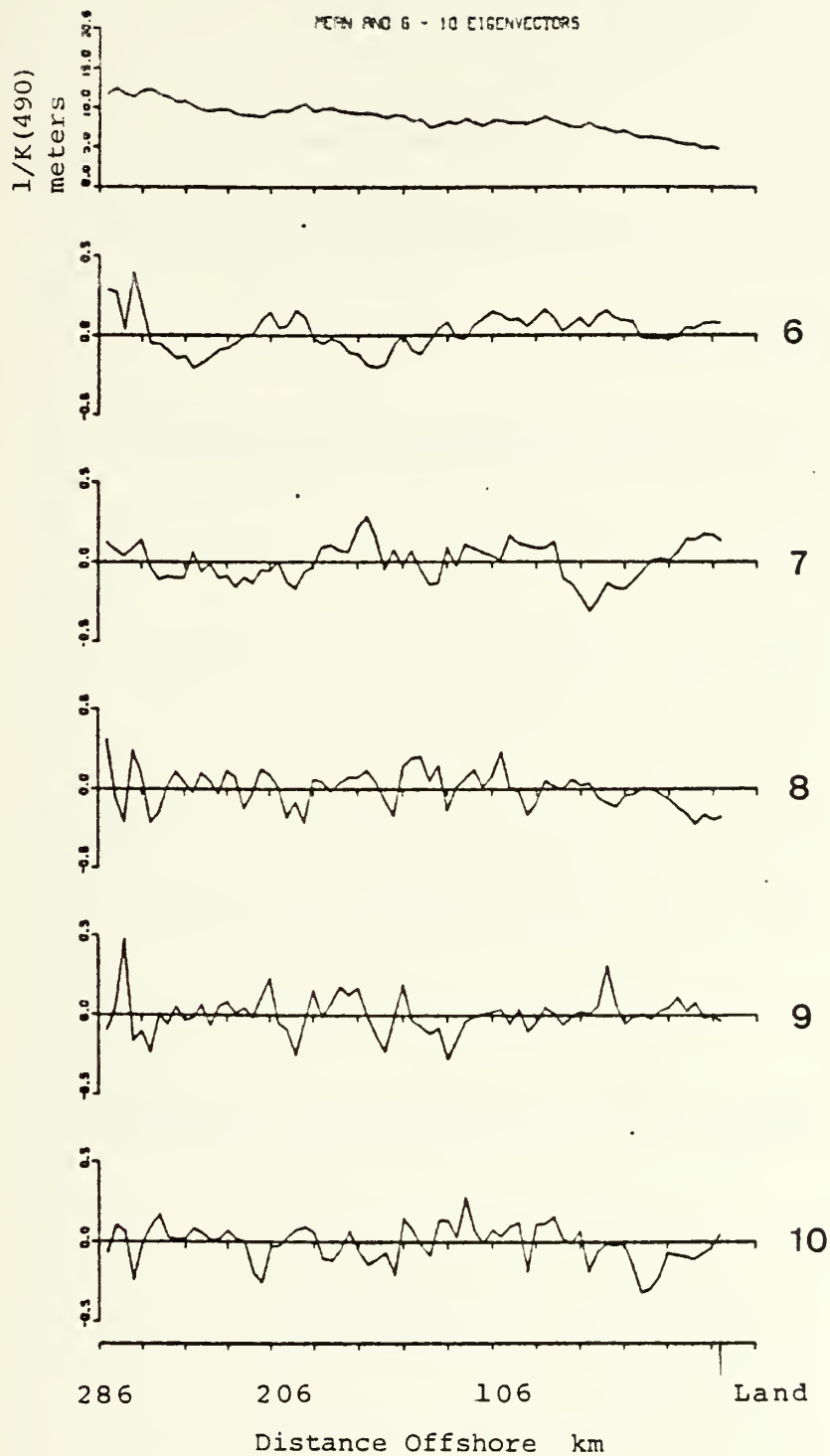


Figure 27. Mean and Eigenvectors 6 to 10 for Partition Four.





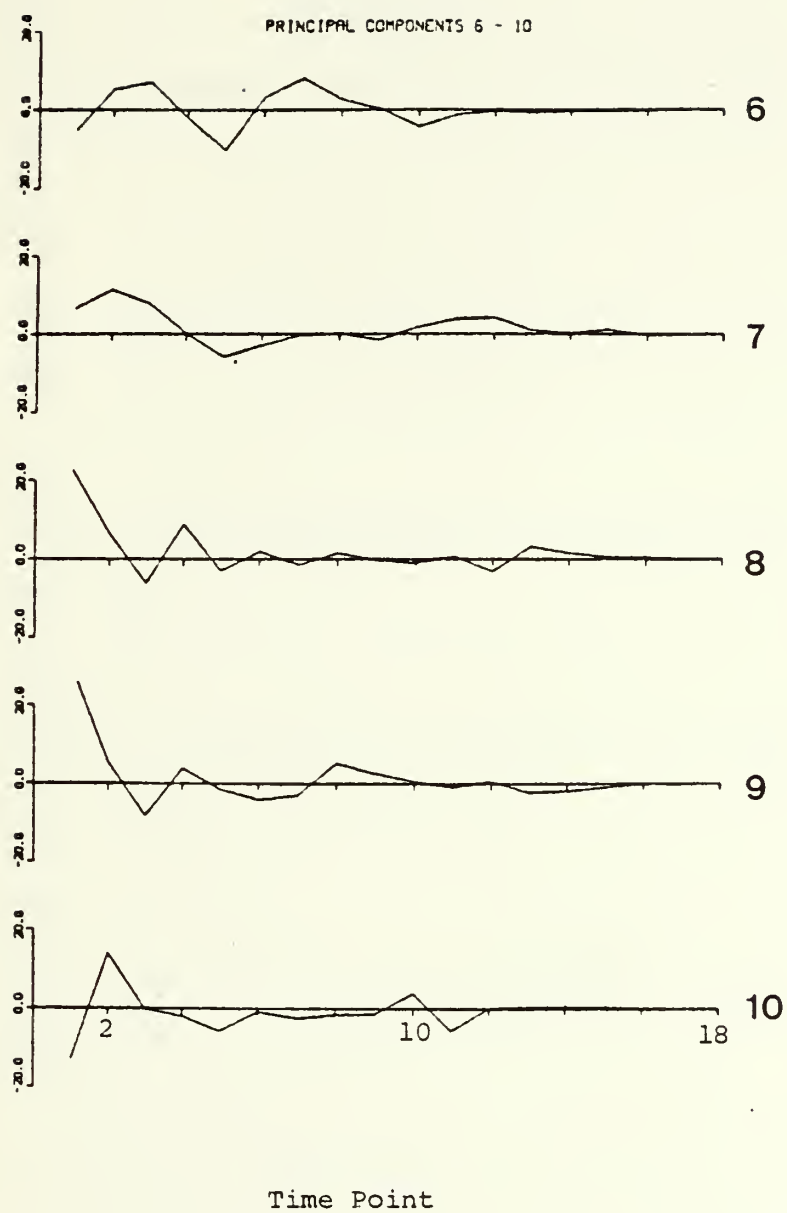


Figure 28. Principal Components 6 to 10 for Partition One.



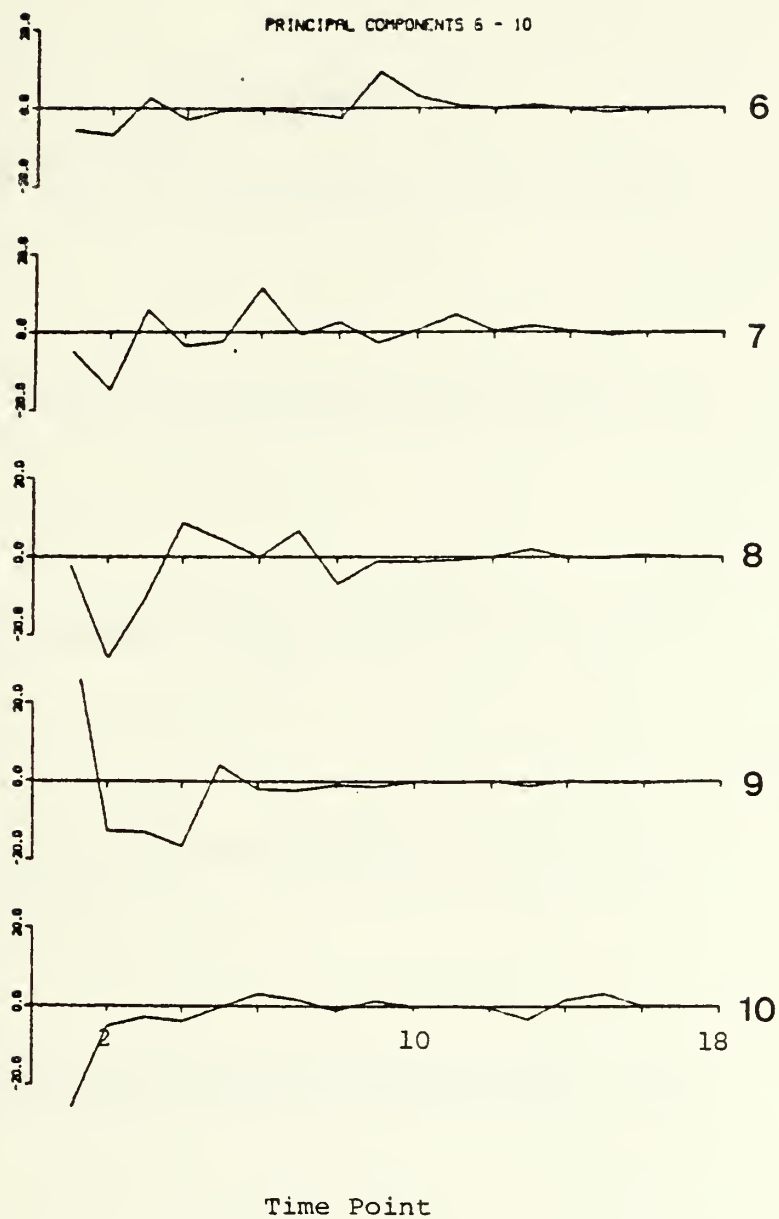


Figure 29. Principal Components 6 to 10 for Partition Two.



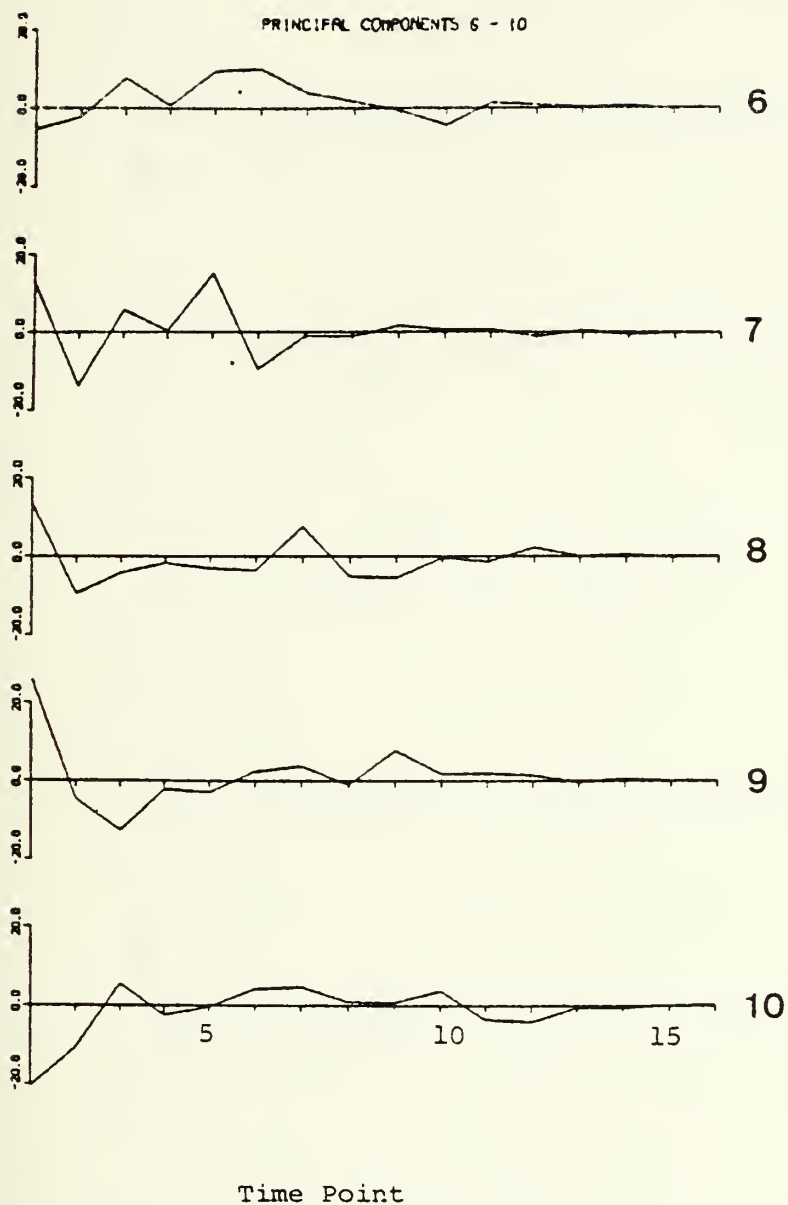


Figure 30. Principal Components 6 to 10 for Partition Three.



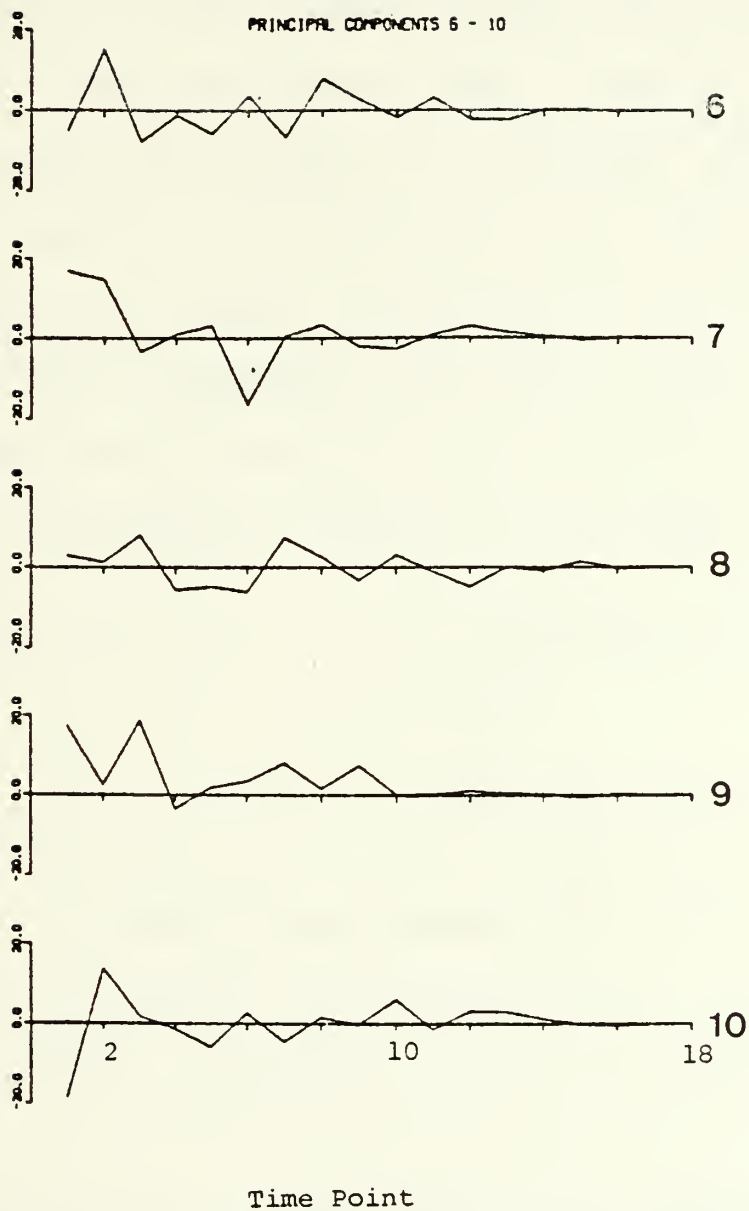


Figure 31. Principal Components 6 to 10 for Partition Four.





## 5. The Joining Of Two Partitions

Only a cursory treatment of the joining function results is presented. Partition one and two were examined and analyzed as per the joining function development given in Chapter IV. The analysis was based on performing the EOF analysis on partitions one and two combined, and then comparing this result to those obtained from the separate EOF analyses that were joined. It was found that the joining function principle components were within .0001 m of those computed using the two partitions as one data set. Furthermore, using ten degrees of freedom, it was found that

$$\mathbf{J}^T \mathbf{J} = \mathbf{I} \quad (\text{within } 2.5 \times 10^{-6}) \quad (51)$$

and

$$\mathbf{E}^T \mathbf{E} = \mathbf{I} \quad (\text{within } 8.0 \times 10^{-6}) \quad (52)$$

This result is based on the orthogonality of the eigenvectors as  $\mathbf{J}$  is the matrix of eigenvectors of the covariance matrix of principal components for the two partitions combined.

Additionally, a comparison of the principal components yielded (For a joint sample size of 17)

$$\left(\frac{1}{16}\right) \mathbf{A}^T \mathbf{A} = \mathbf{L} \quad (\text{within } 1.4 \times 10^{-3}) \quad (53)$$



Representing the principal components of the joining functions with  $\underline{Y}$ , it follows that

$$\left(\frac{1}{16}\right) \underline{Y}^T \underline{Y} = \underline{L} \quad (\text{within } 5.0 \times 10^{-4}) \quad (54)$$

Again the small difference demonstrates the utility of the joining process.

The eigenvalues obtained by thus joining the eigenvectors and principal components from partitions 1 and 2 are given in Table III, together with fractions of total sample variance. At face value, the first ten eigenvalues account for 98.55% of total sample variance. Recall however, that the input data were represented in truncated form, using only the first ten principal components from each of the partitions. This original approximation retained only 97.89% of the total variance computed from the original data, hence, it is necessary to adjust the apparent truncation of the joined result accordingly. The results of this adjustment are given in the third column of Table III and show that assuming that only the first ten eigenvectors are significant actually leads to a truncation to 96.50% of the total sample variance. While 3.5% precision is an acceptable level of approximation for most problems in geophysical



data interpretation, the effects of successive truncation must be given careful attention when applying the partitioned method to EOF analysis.

This example indicates strongly that the partitioning approach to EOF analysis can provide computationally acceptable results when applied to satellite image data. The example also emphasizes that proper care must be given to controlling successive truncation in the partition joining process. It is left to future projects to investigate questions such as joining partitions on the basis of partially intersecting samples to provide optimal functions for interpolating satellite data into cloudy regions, and to interpretation of partition joining functions to illuminate spatial correlations between locally important structures (e.g., topographically generated mesoscale eddies) and the dominant structure of the overall domain (e.g., that associated with the evolution of the synoptic scale upwelling front over the continental slope and shelf over the course of the upwelling season). It is questions of this kind that address the ultimate utility of partitioned EOF analysis. The present effort is limited to preliminary work to establish foundations of feasibility and procedural constraints.



TABLE III

## Eigenvalue Data for Joining Process

Order	Eigenvalue <sup>2</sup> (m )	Percentage of Variance	Cumulative Percentage
1	594.00	40.74	40.74
2	401.60	27.54	68.28
3	171.70	11.78	80.06
4	67.35	4.62	84.68
5	63.86	4.38	89.06
6	47.57	3.26	92.32
7	34.34	2.36	94.68
8	23.17	1.59	96.27
9	20.52	1.41	97.68
10	12.70	0.87	98.55





## VI. DISCUSSION AND CONCLUSIONS

Zonal transects of optical depth ( $1/k(490)$  m) measured with the Nimbus-7 CZCS have been analysed to investigate bio-optical structure over the continental shelf and slope off central California. Samples of cloud free data were selected and processed for latitudes 35-53N, 35-40N, 35-22N and 35-00N. The data were observed in 1979, 1980, and 1982 during the months May through November. The zonal structure in these samples was analysed using EOF's computed separately for each section. Meridional variance structure was analysed only qualitatively through inspection of similarities in features contained in EOF's of the different transects and in the temporal sequences of associated principal components. Finally, the computational feasibility of applying partitioned EOF analysis methods to this type of data was investigated by joining the EOF's of the two northernmost transects to form estimates of the EOF's of the combined spatial domain.

The first eigenvectors for four zonal transects of optical depth  $1/(k490)$  each contained dominant scales of order



200 km or greater, and accounted for between 35 and 54 percent of the total variance. They are each also characterized by a band of low variability in optical depth in the inshore region influenced by upwelling and the Davidson Inshore Current. This band is confined within 45 km of the coast at 35° 53' N, and monotonically broadens to approximately 100 km at 35°N latitude. This behavior is possibly related to the broadening of the continental shelf and slope with longshore distance south of Monterey. Hurlburt (1979) showed that the topographic beta effect plays a fundamental role in the dynamics associated with mesoscale (order 100 km) longshore variations in topography by affecting the strength of the longshore flow. Also, the influence of topography can produce barotropic flow beyond its immediate vicinity. For mesoscale variations in coastline geometry, the coastal currents and the patterns of vertical motion tend to follow the coastline, but not with uniform strength. Coastal current widths tend to be narrower than the scale of coastline variability. In these terms, the meridional variation in scales present in the first EOF's are qualitatively consistent with the longshore variations in bathymetry of the study domain.



The second eigenvectors account for zonal structure with dominant scale of order 120 km, and with nearly uniform amplitude from the coast to a node approximately 150 km offshore in partitions 1, 2, and 4. The second eigenvector for partition 3 (35 20N) is anomalous in that it is dominated by a zonal waveform with nodes spaced at approximately 80 km, or roughly half the dominant scale of its counterparts. The reason for this behavior should be investigated.

The third eigenvectors are dominated by scales ranging from approximately 60 to 100 km (between nodes). The shapes and scales vary more strongly from partition-to-partition than was the case with the first two eigenvectors.

Across each transect, zonal features with wavelengths 100 km and greater appear. The suggestion of an oscillatory behavior in the meridional direction needs to be studied further. Resolving such a feature requires a more detailed study involving a 2-dimensional analysis of the study domain.

The large eddy field associated with the shoreward boundary of the California Current was observed in the data set. The scales of this eddy field were of the same magnitude as the spatial scales employed in the partitions.



This necessitated placing the partition boundary within this eddy field and cutting away some of the features. The seasonal development of a synoptic scale upwelling front off the California coast is strongly suggested in the data and its eigenvectors. The smaller eddies associated with this pattern ranged from 5 to 100 km in scale.

The convergence of the eigenvalues to roughly 98 percent of the variance after the tenth value was of particular interest. This was true for all four partitions and although this is not an overwhelming reduction in the degrees of freedom of the initial system, it is significant.

Satellite images, and other fields of oceanic and atmospheric variables, provide massive data sets. Large amounts of computer time must often be expended for processing these data sets at even relatively primitive levels. Analyses and interpretations are, moreover, made difficult by the sheer volume of data. EOF analysis provides a viable method for mathematically representing satellite data fields in a compact and easily manipulated form. Data transformed using EOF's illuminates, and facilitates analysis of, the time and space scales associated with a given variable over the domain; the present study has exercised this attribute of





EOF's on a descriptive level. In addition, the compact principal component representation of satellite images provides an efficient form for analysing the response of spatial structure in, for example, optical depth to forcing by wind stress and currents, acting through a bio-optical model; this is a logical avenue for future research to build on the present results.

Considering purely computational aspects of EOFs, the well-known symmetry of eigenvector solutions in the time and space domain can be used to great advantage in the analysis of satellite image data. The number of spatial grid points in even the single trackline partitions of the present study yield large, but computationally tractable, scatter matrices. The larger arrays associated with 2-dimensional area partitions, each with several hundred grid points, will clearly exceed sizes admitting direct computation of spatial EOFs. The linear algebra and scalings involved in using the smaller time domain scatter matrix for computation of space domain EOF's is reviewed in Appendix C.

The partitioned method of EOF analysis illuminates correlations between variability in spatially separate sub-regions. The present results demonstrate the computational



feasibility of this piecewise approach when applied to CZCS optical depth data. There is every reason to believe that the method may be equally well applied to other CZCS parameters and to infrared imagery of SST. Further work in this area should aim to determine whether the joining functions linking EOF's from separate domains are sufficiently stationary to provide a basis for optimally interpolating satellite image data of these types over cloud-covered areas of a particular day's image. Other applications to be explored include determination of the extent to which correlations between 3-dimensional in situ data and 2-dimensional satellite data in small sub-regions may be extended to other parts of the larger domain covered by satellite data alone.



## APPENDIX A

### SATELLITE DATA PROCESSING METHODS

#### A. INTRODUCTION

Data processing was divided into three major levels. Level-I processing includes all steps required to take the original data tape to a Level-I tape. Level-II processing includes all steps between a Level-I tape and a Level-II tape. Level-III processing includes the steps involved to take the Level-II output to a usable form. The following sections briefly describe the steps involved in the three levels of processing.

Computer hardware utilized was that resident at the Naval Postgraduate School, Monterey, California. The main frame computer used was the IBM 3033AP while the mini-computer used was the Apple-II. Computer software referred to in this section is either a system utility resident to the IBM system or a locally generated program. Documentation of the locally generated programs can be obtained from:

Dr. J. L. Mueller (Code 68My)

Department of Oceanography

Naval Postgraduate School

Monterey, California 93943



The software involved has many system-dependent features, as well as features inserted for convenience. Users of these programs on other systems are cautioned to review the documentation carefully prior to attempting to transfer the software.

## B. LEVEL-I PROCESSING

Figure 32 is a schematic diagram illustrating the processing steps for Level-I and should be referred to throughout this discussion. The master tape (raw satellite data) was obtained from the Scripps Institution of Oceanography, San Diego, California. Table IV gives a summary of the master tapes utilized in this study. The data were in the form of a standard magnetic tape in a binary format with 6250 bits per inch (BPI). The tapes were originally created using a Hewlett Packard (HP) - 3000 which has a characteristic high order, low order bit arrangement opposite to the IBM system. Therefore, before using this raw data in the IBM 3033AP, it had to undergo a byte swap routine. This byte swap was accomplished when the unformatted working backup tape was made using local program VISBKV. After the unformatted backup tape is made a variable blocked spanned (VBS) format tape is produced using the system utility IEBGENER.





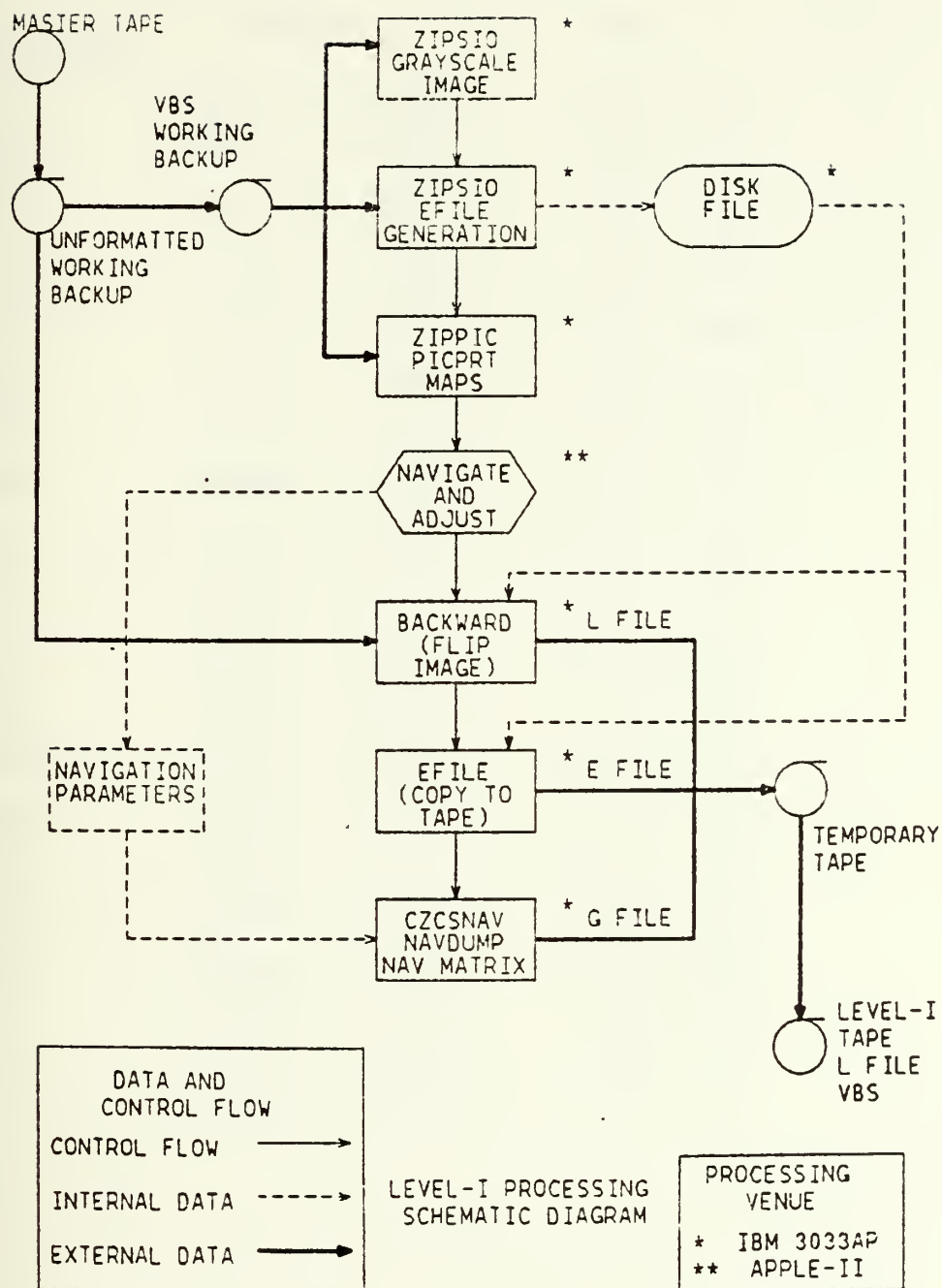


Figure 32. Level-I Processing Schematic Diagram



TABLE IV  
Satellite Data Tapes

Tape Designation	Source	Date	SST available
VIS017	Nimbus 7 (CZCS)	16 OCT 1979	no
VIS032	Nimbus 7 (CZCS)	12 NOV 1979	no
VIS040	Nimbus 7 (CZCS)	23 NOV 1979	no
VIS094	Nimbus 7 (CZCS)	6 MAY 1980	yes
VIS095	Nimbus 7 (CZCS)	5 MAY 1980	yes
VIS097	Nimbus 7 (CZCS)	17 MAY 1980	yes
VIS104	Nimbus 7 (CZCS)	3 JUN 1980	yes
VIS105	Nimbus 7 (CZCS)	6 JUN 1980	yes
VIS106	Nimbus 7 (CZCS)	7 JUN 1980	yes
VIS117	Nimbus 7 (CZCS)	12 JUN 1980	yes
VIS111	Nimbus 7 (CZCS)	23 JUN 1980	yes
VIS112	Nimbus 7 (CZCS)	24 JUN 1980	yes
VIS113	Nimbus 7 (CZCS)	25 JUN 1980	yes
VIS126	Nimbus 7 (CZCS)	1 AUG 1980	yes
AR0000	Nimbus 7 (CZCS)	30 SEP 1982	no
AR2642	Nimbus 7 (CZCS)	5 OCT 1982	no
AR2668	Nimbus 7 (CZCS)	16 OCT 1982	no
AR2685	Nimbus 7 (CZCS)	27 OCT 1982	no
AR2686	Nimbus 7 (CZCS)	28 OCT 1982	no
AR2691	Nimbus 7 (CZCS)	1 NOV 1982	no
AR2693	Nimbus 7 (CZCS)	3 NOV 1982	no
AR2704	Nimbus 7 (CZCS)	14 NOV 1982	no



This format is used in conjunction with unformatted read statements to minimize computer time. These two copied tapes serve as the working tapes for the remainder of the Level-I processing, and the master tape is archived.

Using the VBS formatted tape, a Versatec plotter grayscale is produced using local program ZIPSIO. This program also unpacks the Event file (hereafter referred to as the E-file) and writes it to a storage disk. The grayscale depicts the satellite pass in picture form for hand analysis of landmarks. Line numbers and pixel numbers are taken off the grayscale for clear, cloud-free landmarks. These values are entered into local program ZIPPIC to generate a 'PICPRINT'. This is a matrix of radiance value centered on the individual landmarks line and pixel number. These PICPRINTS are then contoured by hand (using a threshold value of 18 counts for land or clouds) to determine an exact time and pixel number for the landmark. The landmark's latitude, longitude, line number and pixel number with additional housekeeping data are entered into local program CZCSNAV on the Apple II. This program is interactive and prompts for necessary inputs. Additionally this program adjusts roll, pitch and yaw to reduce the root mean squared



distance error in the navigation problem. The mean rms value obtained for all the adjusted, utilized data was approximately 1.09 n.mi.. The final product of this step generates a set of navigation parameters that are used to generate a navigation matrix. This step is accomplished using local program CZCSNAV2 to generate the navigation matrix and NAVDUMP to write the navigation matrix (hereafter referred to as the G-file) to a temporary formatted tape.

The E-file is copied from its temporary disk storage to the temporary tape as the G-file. Additionally the Data file (hereafter referred to as the L-file) is first reversed from its bottom-to-top orientation to a top-to-bottom orientation using local program BACKWARD. This program also puts the L-file to the previously mentioned temporary storage tape. Finally, these files on the temporary tape are copied to a Level-I tape using the system utility IEBGENER. The only difference between the temporary tape and the final Level-I tape is that the L-file is copied into an unformatted file which will aid in the speed of further processing.





### C. LEVEL-II PROCESSING

Figure 33 is a schematic diagram illustrating the processing steps for Level-II. The Level-I tape generated by the steps discussed in the previous section is the input tape for this processing. Only the L-file is affected by the Level-II processing as the E-file and G-file are copied straight to the Level-II tape using the system utility IEBGENER. The L-file is used to generate output for calculating the proper values of the Angstrom coefficient for each scene. This is done using local program CZPARMS2 and an assumed value for the Angstrom coefficient. Chapter III Section C.2. discusses the importance and method of finding these values. Next, the computed Angstrom coefficients with the L-file are rerun through CZPARMS2 to regenerate the L-file. This regeneration involves taking the raw counts of each channel and applying the bio-optic algorithms discussed in Chapter III to produce values for chlorophyll and K. At this point the adjustment algorithm discussed in Chapter V has not been applied. Analyses of the initial Level-II output precipitated the need for the corrective algorithm, which was then applied during Level-III processing.



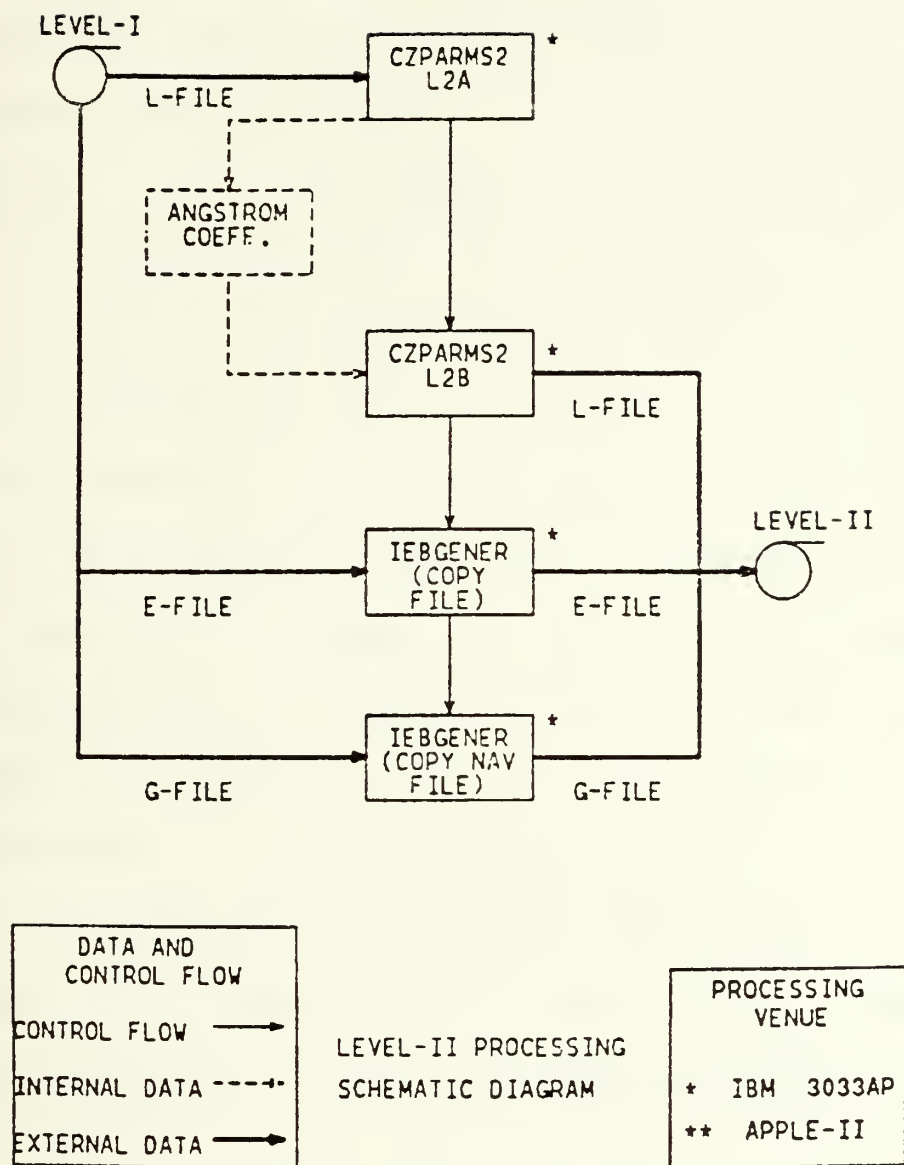


Figure 33. Level-II Processing Schematic Diagram



#### D. LEVEL-III PROCESSING

Figure 34 illustrates the Level-III processing steps. The Level-III processing basically takes the data obtained in Level-II and marries it to the navigation matrix generated during Level-I processing. Using the four designated tracks (Fig. 5), the coastal starting points from each track were entered into local program TEDDUMP to provide the navigation block of the track origin. The G-file contains data (in latitude and longitude values) every sixteenth pixel and sixteenth line. Once the origin block is established the exact line and pixel was interpolated using local program FINDPIX on the Apple II. With this starting point local program DATA4 was entered to generate every 1 km along each track an associated line and pixel number which was then converted into the appropriate data values. This output was written to storage for later processing. It was here that the adjustment algorithm was applied, producing the final version of the data in a navigated form.



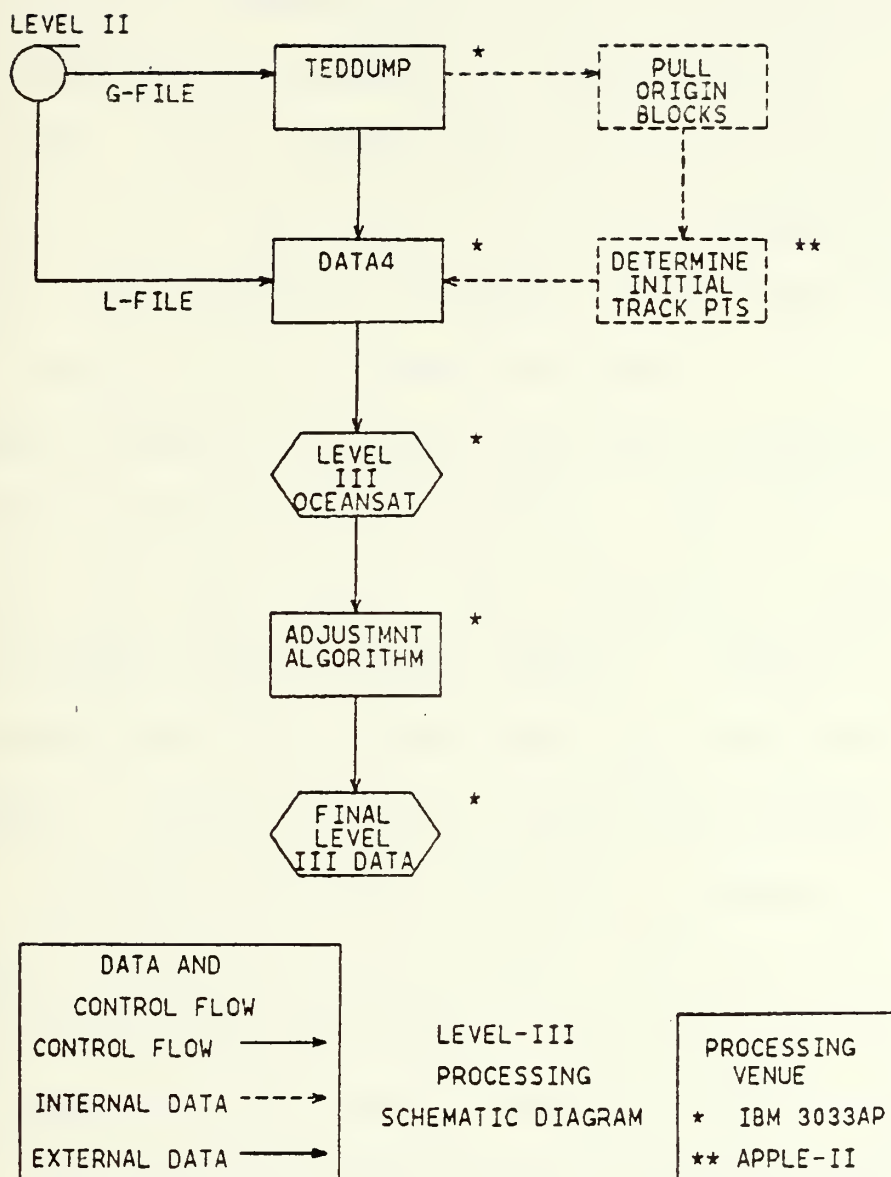


Figure 34. Level-III Processing Schematic Diagram





## APPENDIX B

### DATA CONDITIONING

To apply the Level-III data to the analytic techniques certain conditioning steps were necessary prior to beginning. Much of the conditioning applied to the data was dependent on the data itself as to its completeness and behavior. This discussion focusses on the steps necessary prior to using the EOF analysis techniques.

Figure 35 depicts the steps involved in this discussion and should be referred to as a guide. First the Level-III data for the four tracks and twenty-two scenes were extracted using local program PACKJOB. Twenty-two files each contained the data for the four tracks for each particular scene. These data were plotted using local program PARPLOT and the DISSPLA utilities resident on the IBM-3033AP. The format of the plot was chosen to give an indication of either good data or bad data with no structure. This plot was used to decide on the partitioning scheme. Four partitions were selected and their details are listed in Table V.



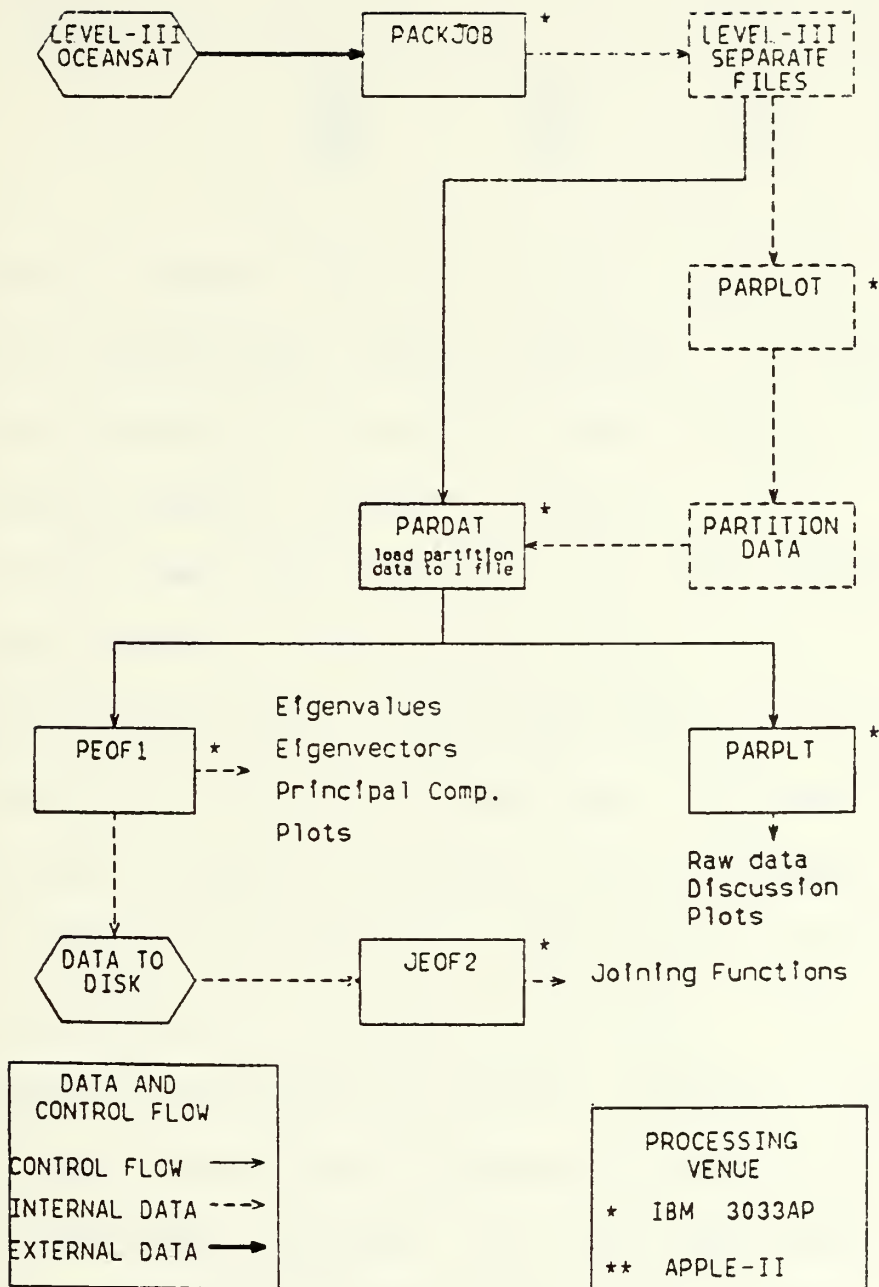


Figure 35. Data Conditioning Schematic Diagram



TABLE V  
Partition dimensions

Track No.	Partition No.	Min Grid	Max Grid	Ntime	Nspace
1	1	180	410	17	231
2	2	165	425	17	261
3	3	200	467	16	268
4	4	200	485	17	286

Figures 36 through 39 show the plots generated by parplot and the partitioning given in Table IV. The objective of the partitioning was to find the most complete data over time and space possible given ten samples.

Data from these four partitions was then entered into local program PARDAT. This program applied most of the conditioning to the data set. Only the K(490) data was utilized from this point on although this program could be easily altered to focus on another optical parameter. The data were searched to find good points and bad points and a control arrangement for later use was made. The raw data were scaled and inverted to produce  $1/K(490)$  values in meters. Next the data were averaged by every fourth point to smooth out noise features. At this point data strings with gaps existed for each applicable scene. Next a linear interpolating routine was applied to obtain continuous data at each time point. Finally, the data for all scenes and



tracks were combined and written to disk in a single data file. To this point the conditioning applied has consisted of partitioning the data into four partitions, rejecting incomplete scenes, scaling the K(490) values, averaging the data by every four values, and applying linear interpolation to fill in the remaining gaps.

The conditioned data was then plotted using local program PARPLT and the DISSFIA system utilities. The plots generated are figures 7 through 10 and were used in Chapter V Section B to discuss the data and its relationship to the regional oceanography.

The final steps of the data conditioning involved applications of the EOF analysis techniques. Local program PEOF1 produced eigenvalues, eigenvectors, and principle components for each partition and plotted the output. Figures 11 through 14 and 16 through 31 are the plots produced. The eigenvalues, eigenvectors and principle components were all written to disk for later use. The local program JEOF2 was designed to produce the joining function that related partition one to partition two.





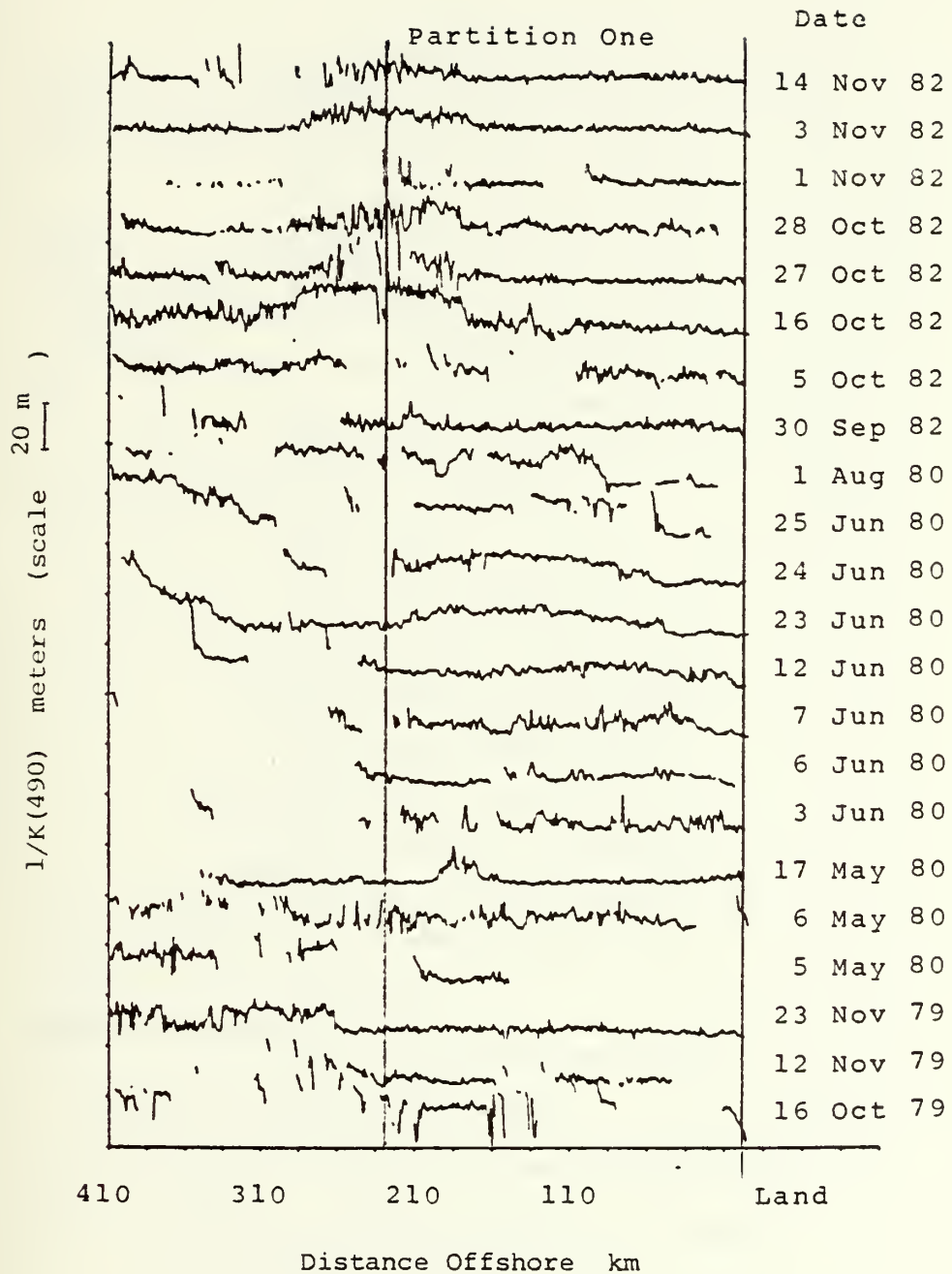


Figure 36. Partitioning Scheme for Track One (35 53 N)



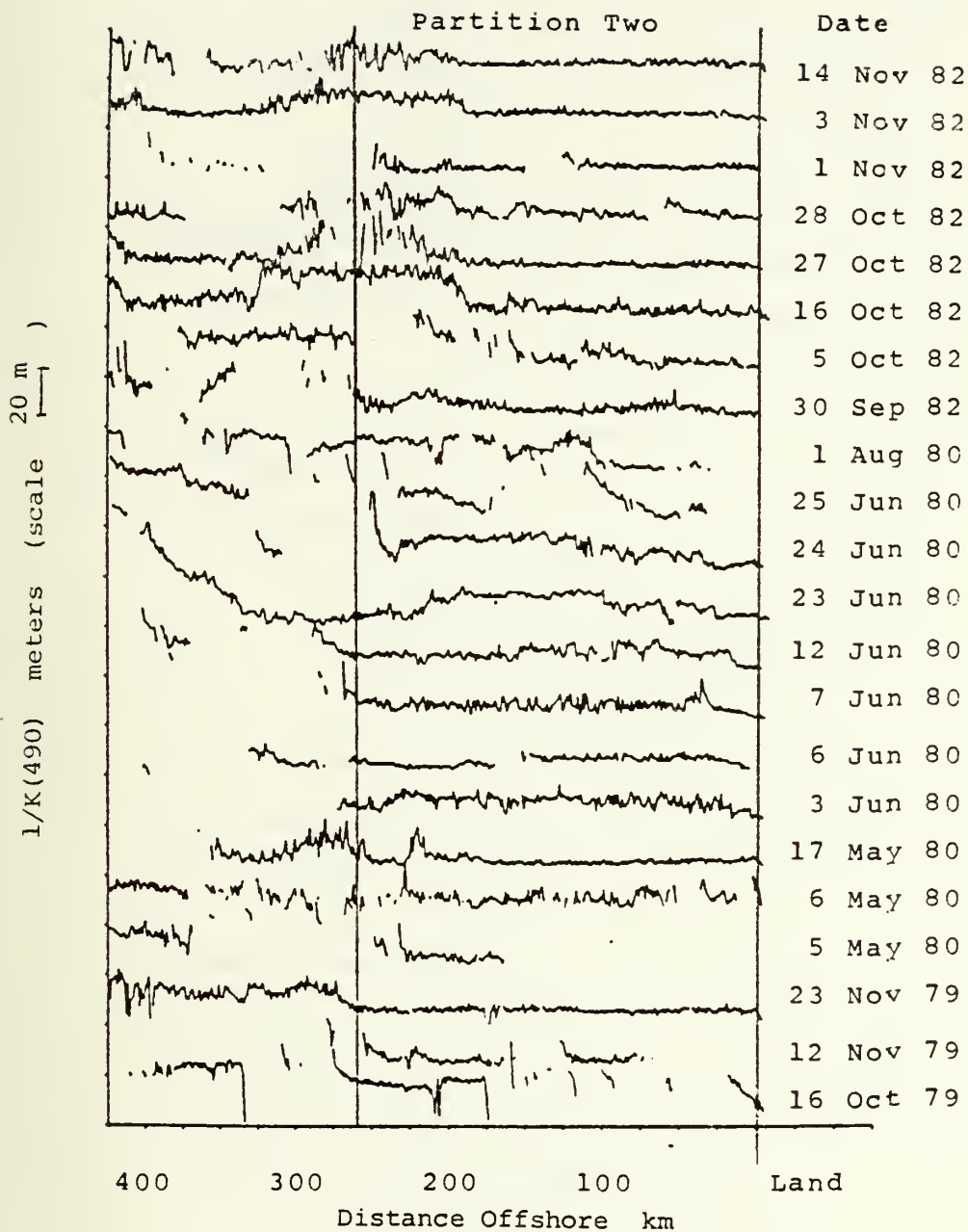


Figure 37. Partitioning Scheme for Track Two (35 40 N)



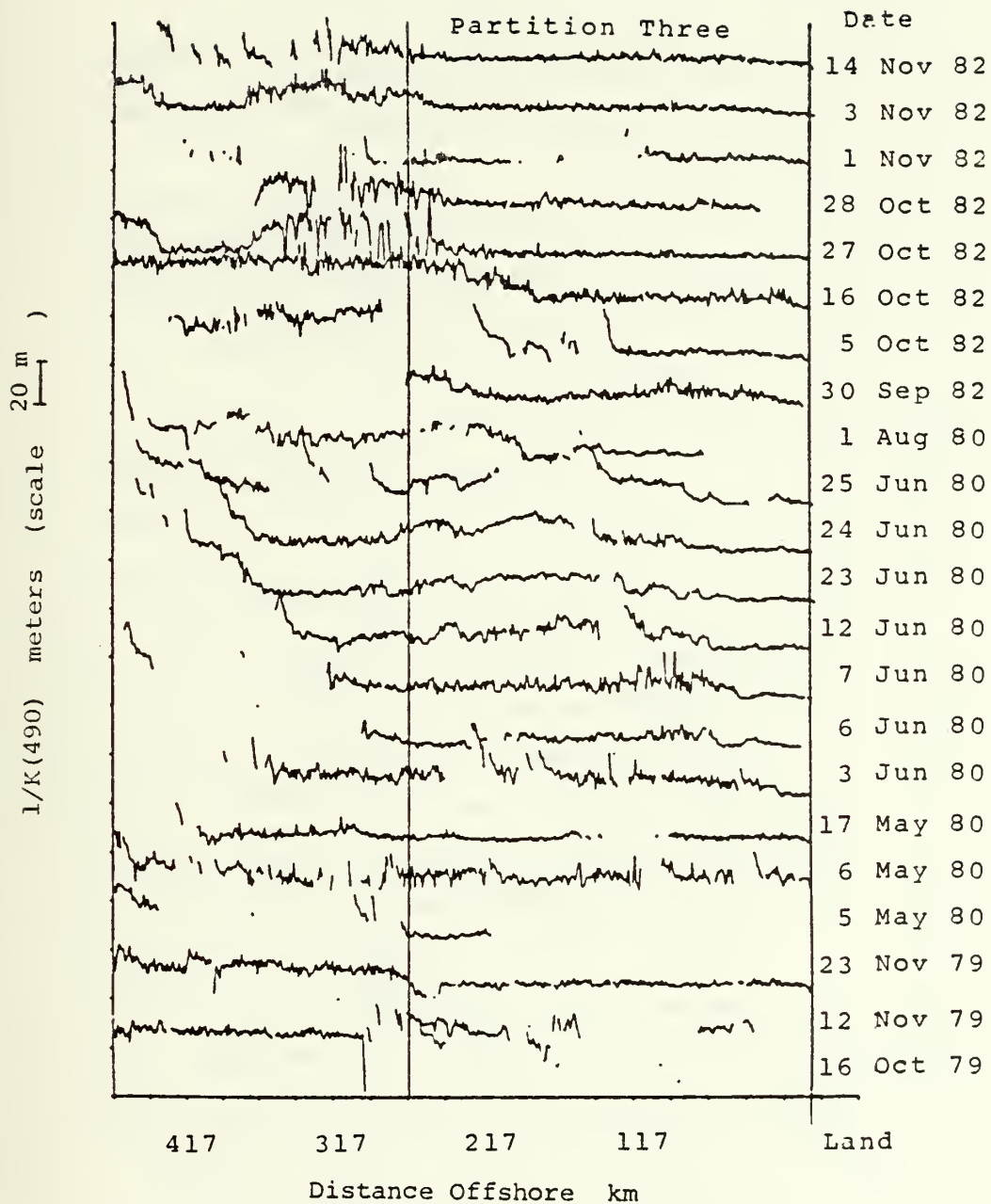


Figure 38. Partitioning Scheme for Track Three (35 22 N)



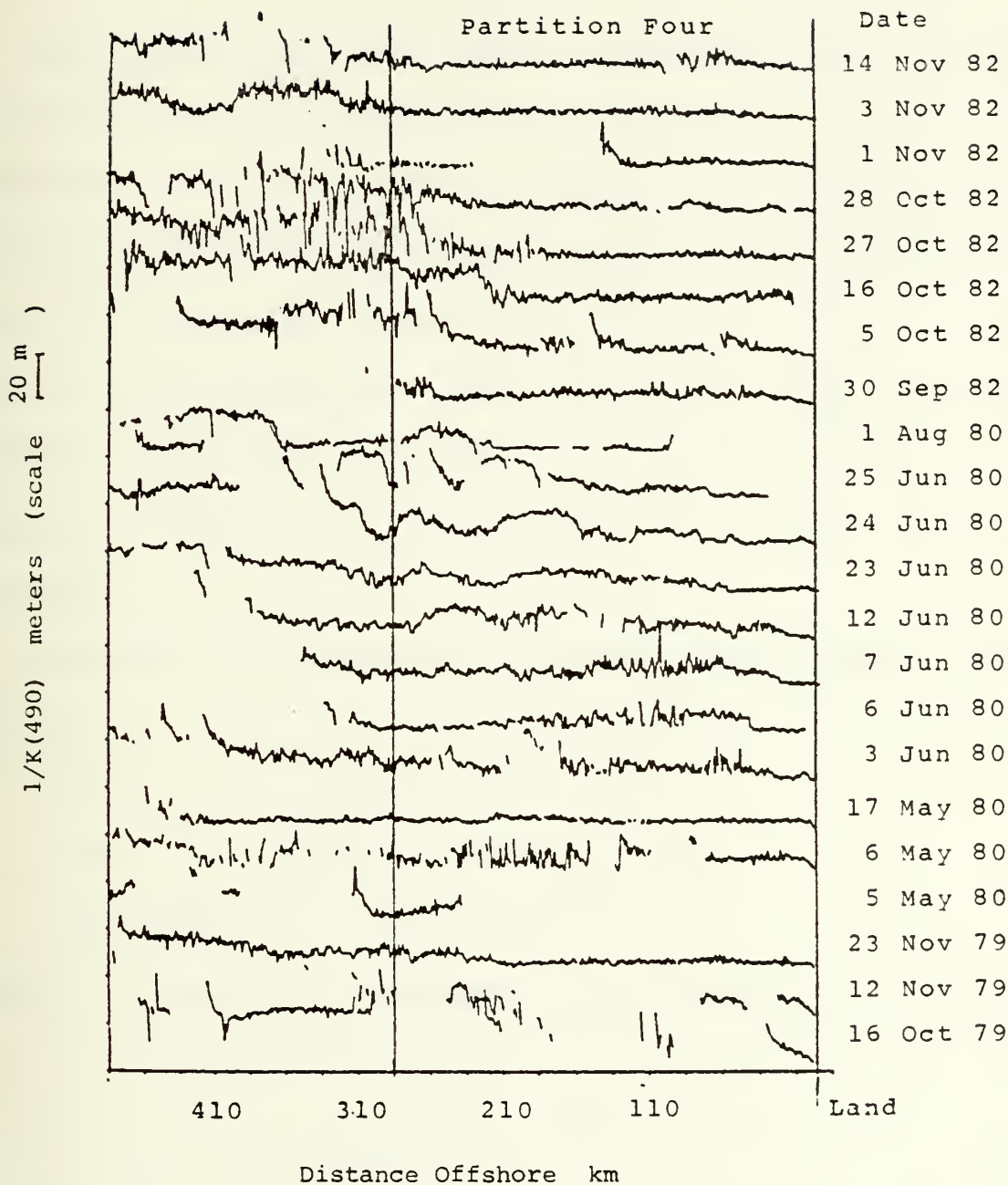


Figure 39. Partitioning Scheme for Track Four (35 53 N)





# APPENDIX C

## EOF PROCESSING

The desired EOF's are those in the space domain, which for satellite data, is dimensioned much larger than the time dimension. It is possible to significantly expedite computations by computing eigenvalues, eigenvectors and principal components using the smaller covariance matrix of the time domain, and to then scale these results to obtain the eigenvectors and principal components in the space domain. The algebraic basis for this approach is reviewed in this appendix.

Consider the following convention for dimension notations

Space . . . .  $n = 1, \dots, N$

Time . . . .  $m = 1, \dots, M$

EOF (order) . . . .  $k = 1, \dots, K$

where  $K \leq \min(M, N)$ . As before the raw data matrix is given by

$$\underline{F}' = \begin{bmatrix} f'_{mn} \end{bmatrix} \quad (55)$$

of  $M$  rows by  $N$  columns. The sample mean in the space domain is given by



$$\bar{f} = \frac{1}{M} \left[ \sum_{m=1}^M f'_{mn} \right] \quad (56)$$

of dimension  $1 \times N$ . The centered data matrix in the space domain is given by

$$F = \left[ \begin{matrix} f'_{n1} & - \bar{f} \end{matrix} \right] \quad (57)$$

From Chapter IV the sample space covariance matrix (of size  $N \times N$ ) is

$$S = \frac{1}{M-1} F^T F \quad , \quad (58)$$

and the sample time covariance matrix (centered in space and of size  $M \times M$ ) is now defined as

$$T = \frac{1}{M-1} F F^T \quad . \quad (59)$$

If  $\lambda_k$  and  $e_k$  are an associated eigenvalue and eigenvector respectively of  $S$ , then

$$S e_k = \lambda_k e_k \neq 0 \quad , \quad (60)$$

since

$$\lambda_k \neq 0 \text{ and } e_k \neq 0 \quad . \quad (61)$$

Then

$$F e_k \neq 0 \quad , \quad (62)$$

and therefore



$$\frac{1}{M-1} \mathbf{F} \mathbf{F}^T \mathbf{F} \mathbf{e}_k = \lambda_k \mathbf{F} \mathbf{e}_k \quad (63)$$

(noting the commutative property of  $\lambda_k$  and  $\mathbf{F}$ ). Thus,  $\lambda_k$  is an eigenvalue of  $\mathbf{T}$  with associated eigenvector (in the time domain)

$$\mathbf{a}_k = \mathbf{F} \mathbf{e}_k, \quad (64)$$

where  $a_{mk}$  is the  $k$ 'th principal component (in the space domain) at time point  $m$ .

We now consider the eigenvalues  $\lambda_k$  and eigenvectors  $\mathbf{e}_k$  of  $\mathbf{T}$ , normalized such that

$$\sum_{m=1}^M \xi_{mi} \xi_{mj} = \delta_{ij}, \quad (65)$$

with time domain principal components

$$\mathbf{z}_k = \mathbf{F}^T \mathbf{e}_k; \quad k = 1, \dots, K, \quad (66)$$

where the 'significance order  $K$  is selected either to retain an arbitrary fraction of the total sample variance, or according to one of the more objective statistical selection rules discussed by Preisendorfer, et al. (1981).

The principal components in the time and space domain have the property that

$$\sum_{n=1}^N \zeta_{ni} \zeta_{nj} = \sum_{m=1}^M a_{mi} a_{mj} = (M-1) \lambda_i \delta_{ij}. \quad (67)$$



Recall that  $\underline{F}$  was centered on  $\bar{\underline{F}}$  in the space domain, and that both  $\underline{S}$  and  $\underline{F}$  were therefore normalized by the factor  $(1/M-1)$ .

By analogy to equation (63)

$$\frac{1}{M-1} \underline{F}^T \underline{F} \underline{F}^T \underline{\xi}_k = \lambda_k \underline{F}^T \underline{\xi}_k = \lambda_k \underline{\xi}_k, \quad (68)$$

where  $\underline{\xi}_k$  is now seen to be an eigenvector of  $\underline{S}$ , but of length

$$\left| \underline{\xi}_k \right| = \sqrt{(M-1)\lambda_k}, \quad (69)$$

rather than being an orthonormal eigenvector of length 1.

The two are thus related by

$$\underline{e}_k = \frac{\underline{\xi}_k}{\sqrt{(M-1)\lambda_k}} \quad (70)$$

(principal components in the time domain scale to orthonormal eigenvectors in the space domain),

and by similar arguments

$$\underline{a}_k = \left( \sqrt{(M-1)\lambda_k} \right) \underline{\xi}_k \quad (71)$$

(orthonormal eigenvectors in the time domain scale to principal components in the space domain).





## LIST OF REFERENCES

Aranuvachapun, S. and T. T. Thorton, 1983: Spatial and Temporal Transformation of Shallow Water Wave Energy. Submitted to Journal of Geophysical Research.

Aranuvachapun, S. and J. A. Johnson, 1979: Beach Profiles at Gorleston and Great Yarmouth. Coastal Engineering, 2, 201 - 213.

Austin, R. W., 1981: Remote Sensing of the Diffuse Attenuation Coefficient of Ocean Water, paper presented at The Symposium of the AGARD Electromagnetic Wave Propagation Panel on Special Topics in Optical Propagation, 29th, Monterey, California, 6 - 10 April.

Bernstein, R. L., L. Breaker, R. Whritner, 1977: California Current Eddy Formation: Ship, Air and Satellite Results. Science, 195, 353 - 359.

Brown, R. L., 1974: Geostrophic Circulation off the Coast of Central California. Master's Thesis, Naval Postgraduate School, Monterey, California.

Chelton, D. B. and R. E. Davis, 1982: Monthly Mean Sea Level Variability Along the West Coast of North America. Journal of Physical Oceanography, 12, 757 - 784.

Coddington, K., 1979: Measurement of the California Undercurrent. Master's Thesis, Naval Postgraduate School, Monterey, California.

Eckart, C. and G. Young, 1936: The Approximation of One Matrix By Another of Lower Rank. Psychometrika, 1, 211 - 221.

Eckart, C. and G. Young, 1939: A Principal Axis Transformation for Non-hermetian Matrices. Bull. Am. Math Soc., 45, 118 - 130.

Gordon, H. R., 1976: Radiative Transfer: A Technique for Simulating the Ocean in Satellite Remote Sensing Calculations. Applied Optics, 15(8), 1974 - 1979.

Gordon, H. R. and D. K. Clark, 1981: Clear Water Radiances for Atmospheric Correction of Coastal Zone Color Scanner Imagery. Applied Optics, 20(24), 4175 - 4180.

Gordon, H. R., D. K. Clark, J. L. Mueller and W. A. Hovis, 1980: Phytoplankton Pigments from the Nimbus-7 Coastal Zone Color Scanner: Comparisons with Surface Measurements. Science, 210, 63 - 66.



Gordon, H. R., D. K. Clark, J. W. Brown, O. B. Brown, R. H. Evans and W. W. Broenkow, 1983: Phytoplankton pigment Concentrations in the Middle Atlantic Bight: Comparison of Ship Determinations and CZCS Estimates. Applied Optics, 22, 20 - 36.

Gordon, H. R. and W. R. McCluney, 1975: Estimation of the Depth of Sunlight Penetration in the Sea for Remote Sensing. Applied Optics, 14(2), 413 - 416.

Hickey, B. M., 1979: The California Current System - Hypothesis and Facts. Prog. Oceanography, 8, 191 - 279.

Hovis, W. A., D. K. Clark, F. Anderson, R. W. Austin, W. H. Wilson, E. T. Baker, D. Ball, H. R. Gordon, J. L. Mueller, S. Z. El-Sayed, B. Sturm, R. C. Wrigley and C. S. Yentsch, 1980: Nimbus-7 Coastal Zone Color Scanner: System Description and Initial Imagery. Science, 210, 60 - 63.

Hurlburt, H. E., 1974: The Influence of Coastline Geometry and Bottom Topography on the Eastern Ocean Circulation. CUEA Technical Report, 21, 103 pp.

Ingraham, W. J., 1967: The Geostrophic Circulation and Distribution of Water Properties off the Coasts of Vancouver Island and Washington, Spring and Fall, 1963. Fisheries Bulletin, 66, 223 - 250.

Jerlov, N. G., 1976: Marine Optics. 2d. ed., v. 14, Elsevier Scientific Publishing Company.

Johnson, J. E., 1980: Subsurface Dynamical Properties of Variable Features Seen in Satellite IR Imagery Off Point Sur and Their Acoustic Significance. Master's Thesis, Naval Postgraduate School, Monterey, California.

Johnson, E. R., 1982: The Effects of Obstacle Shape and Viscosity in Deep Rotating Flow Over Finite Height Topography. Journal of Fluid Mechanics, 120, 359 - 383.

Kazumasa, K., 1981: Analysis of Edge Waves by Means of Empirical Eigenfunctions. Report of the Port and Harbour Research Institute, 20(3), 3-57.

Kutzbach, J., 1967: Empirical Eigenvectors of Sea Level Pressure, Surface Temperature, and Precipitation Complexes over North America. J. Appl. Meteor., 6, 791 - 802.

Lorenz, E. N., 1956: Empirical Orthogonal Functions and Statistical Weather Prediction. Scientific Report No. 1, Statistical Forecasting Project, Mass. Inst. of Tech., Cambridge, Mass., 47 pp.

Morel, A. and L. Prieur, 1977: Analysis of Variations in Ocean Color. Limnology and Oceanography, 22(4), 709 - 722.



Mueller, J. L., 1976: Ocean Color Spectra Measured Off the Oregon Coast: Characteristic Vectors. Applied Optics, 15, 394 - 402.

Mueller, J. L., J. R. Zaneveld, and R. W. Smith, 1982: R/V ACANIA ODEX CRUISE REPORT. Naval Postgraduate School, Monterey, California.

Munk, W. H., 1950: On the Wind-driven Ocean Circulation. J. Meteorol., 7(2), 79 - 93.

Nelson, C. S., 1977: Wind Stress and Wind Stress Curl Over the California Current. NOAA Technical Report NMFS SSRF-714, U. S. Department of Commerce, 89 pp.

Nestor, D. A., 1979: A Study of the Relationship Between Oceanic Chemical Mesoscale and Sea Surface Temperature as Detected by Satellite IR Imagery. Master's Thesis, Naval Postgraduate School, Monterey, California.

Pavlova, Y. V., 1966: Seasonal Variations of the California Current. Oceanology, 6, 806 - 814.

Pearson, K., 1901: On Lines and Planes of Closest Fit to Systems of Points in Space. Phil. Mag., 2, 559 - 571.

Priesendorfer, R. W., F. W. Zweirs, and T. P. Barnett, 1981: Foundations of Principal Component Selection Rules, S.I.O. Ref. Ser. 81-4, Scripps Institute of Oceanography, 190 pp.

Reid, J. L., Jr., 1960: Oceanography of the North Pacific Ocean During the Last Ten Years. Rancho Santa Fe Symposium on 1957-1958, Years of Change. CALCOFI Reports, 7, 77 - 90.

Reid, J. L., Jr., 1962: Measurements of the California Countercurrent at a Depth of 250 m. Journal of Marine Research, 20(2), 134 - 137.

Reid, J. L., Jr., 1963: Measurements of the California Countercurrent Off Baja California. Journal of Geophysical Research, 68(16), 4819 - 4822.

Reid, J. L., G. I. Roden, and J. G. Wyllie, 1958: Studies of the California Current System. CALCOFI Prog. Rept., 1 July 1956 - 1 January 1958, 27 - 56.

Reid, J. L. and R. A. Swartzlose, 1963: Direct Measurements of the Davidson Current Off Central California. Journal of Geophysical Research, 67(6), 2491 - 2497.

Reid, J. L., R. A. Swartzlose and D. M. Brown, 1963: Direct Measurements of a Small Surface Eddy Off Northern Baja California. Journal of Marine Research, 21(3), 205 - 218.





Rinne, J. and V. Karhala, 1979: Empirical Orthogonal Functions of 500 mb Heights in the Northern Hemisphere Determined From a Large Data Sample. Quart. J. R. Met. Soc., 105, 873 - 884.

Rinne, J. and S. Jarvenoja, 1979: Truncation of the EOF Series Representing 500 mb Heights. Quart. J. R. Met. Soc., 105, 885 - 897.

Smith, R. C. and K. S. Baker, 1978: The Bio-optical State of Ocean Waters and Remote Sensing. Limnol. Oceanogr., 23(2), 247 - 259.

Smith, R. C. and W. H. Wilson, 1981: Ship and Satellite Bio-optical Research in the California Bight. Oceanography from Space, J.F.R. Gower, editor, 13, 281 - 294.

Smith, R. L., 1968: Upwelling. Oceanic Marine Biology Annual Review 1968, 6, 11 - 46.

Sverdrup, H. U. and R. H. Fleming, 1941: The Waters Off the Coast of Southern California March to July, 1937. Bull. Scripps Inst. Oceanogr., 4(10), 261 - 378.

Steele, J. H., 1970: Marine Food Chains, University of California Press, 3 - 112.

Sverdrup, H. U., M. W. Johnson and R. H. Fleming, 1942: The Oceans, Their Physics, Chemistry, and General Biology. Prentice-Hall, Inc., New York. 1087 pp.

Tibby, R. B., 1941: The Water Masses Off the West Coast of North America. Journal of Marine Research, 27a, 99 - 118.

Traganza, E. D., D. A. Nestor and A. K. McDonald, 1979: Satellite Observation of a Nutrient Upwelling Off the Coast of California. J. of Geophys. Res., 85, 4101 - 4106.

Traganza, E. D., 1979: The Use of Temperature and Color in Satellite Detection of Ocean Fronts and Mesoscale Eddies for ASW Applications. Naval Postgraduate School Tech Report NPS-68-79-008, 58 pp.

Vincent, C. L. and D. T. Resio, 1977: An Eigenfunction Parameterization of a Time Sequence of Wave Spectra. Coastal Engineering, 1, 185 - 205.

Willmott, A. J., 1983: The Influence of a Coastal Headland on Oceanic Boundary Currents. Geophys. Astrophys. Fluid Dynamics, 23, 273 - 299.

Wooster, W. S. and J. H. Jones, 1970: California Undercurrent Off Northern Baja. Journal of Marine Research, 28, 235 - 250.





Wooster, W. S. and J. L. Reid, Jr. 1963: Eastern Boundary Currents. The Sea, M. N. Hill, editor, 6 (11), 253 - 260.

Yoshida, K. and H. L. Mao, 1957: A Theory of Upwelling of Large Horizontal Extent. Journal of Marine Research, 16, 123 - 132.



# INITIAL DISTRIBUTION LIST

	No. Copies
1. Defense Technical Information Center Cameron Station Alexandria, VA 22314	2
2. Library, Code 0142 Naval Postgraduate School Monterey, CA 93943	2
3. Professor Robert J. Renard, Code 63Rd Department of Meteorology Naval Postgraduate School Monterey, CA 93943	1
4. Professor Christopher N. K. Mooers, Code 68Mr Department of Oceanography Naval Postgraduate School Monterey, CA 93943	1
5. Adjunct Professor James L. Mueller, Code 68My Department of Oceanography Naval Postgraduate School Monterey, CA 93943	3
6. Assistant Professor Andrew J. Willmott, Code 68Wt Department of Oceanography Naval Postgraduate School Monterey, CA 93943	1
7. Lt. John T. McMurtrie Route 7 Box 385 Aiken, S.C. 29801	2
8. Director Naval Oceanography Division Naval Observatory 34th and Massachusetts Ave. NW Washington, D.C. 20390	1
9. Commander Naval Oceanography Command NSTL Station Bay St. Louis, MS 39522	1
10. Commanding Officer Naval Oceanographic Office NSTL Station Bay St. Louis, MS 39522	1













207513

Thesis

M2574     McMurtrie

c.1        Spatial structures of  
optical parameters in  
the California current,  
as measured with the  
Nimbus-7 Coastal Zone  
Color Scanner.

207513

Thesis

M2574     McMurtrie

c.1        Spatial structures of  
optical parameters in  
the California current,  
as measured with the  
Nimbus-7 Coastal Zone  
Color Scanner.





thesM2574

Spatial structures of optical parameters



3 2768 002 04404 2

DUDLEY KNOX LIBRARY